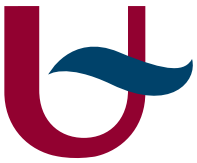

**UNIVERSITEIT ANTWERPEN**

**Faculteit Wetenschappen**

**Departement Fysica**

# A theoretical study of excitons and impurities in freestanding nanowires

---

# Een theoretische studie van excitonen en onzuiverheden in vrijstaande nanodraden

Proefschrift voorgelegd tot het behalen van de graad van doctor in de wetenschappen aan de Universiteit Antwerpen te verdedigen door

**An Slachmuylders**

| | |
|---|---|
| Promotor: | Prof. dr. F.M. Peeters |
| Co-promotoren: | Prof. dr. B. Partoens |
| | Prof. dr. W. Magnus |

Antwerpen 2008

# *Contents*

**Acknowledgments** **v**

**List of abbreviations** **vi**

**1 Introduction** **1**
1.1 Nanowire growth 4
1.1.1 Top-down technique 4
1.1.2 Bottom-up growth 5
1.2 Nanowire applications 11
1.2.1 Diodes 11
1.2.2 Lasers 12
1.2.3 Transistors 13
1.2.4 Sensors 14
1.3 Applications involving shallow donors 16
1.3.1 Transistor 16
1.3.2 Quantum computer 17
1.4 Basic theoretical concepts 18
1.4.1 Band structure of bulk semiconductors 18
1.4.2 The effective mass approximation 21
1.4.3 Validity of the approximations 22

1.4.4 From bulk to low-dimensional systems 22
1.4.5 Excitonic complexes: Excitons and trions 23
1.5 Numerical techniques 26
1.6 Organization of the thesis 28

**2 Excitons without dielectric mismatch 29**
2.1 Introduction 29
2.2 Single particle states 30
2.3 Hamiltonian 32
2.4 Effective potential 33
2.4.1 Approximate analytical expressions 33
2.5 Exciton energy 37
2.5.1 Numerical calculations 37
2.5.2 Comparison with analytical results 39
2.6 Magnetic field dependence 41
2.6.1 Single-particle properties 41
2.6.2 Effective exciton potential 42
2.6.3 Exciton energy 44
2.7 Conclusion 45

**3 Excitons with dielectric mismatch 47**
3.1 Introduction 47
3.2 Hamiltonian 48
3.3 Electrostatic potential with dielectric mismatch 49
3.4 Effective exciton potential 53
3.5 Exciton binding energy 59
3.6 Conclusion 64

**4 Trions with dielectric mismatch 67**
4.1 Introduction 67
4.2 Hamiltonian 68
4.3 Effective 2D trion potential 69
4.4 Trion binding energy and wave function 72
4.5 Conclusion 82

**5 Effect of a metallic gate on the energy levels of a shallow donor 85**
5.1 Introduction 85
5.2 Theory: potential energy and Hamiltonian 87

5.3 Donor energy levels 87
5.4 Influence of an electric field 89
5.5 Conclusion 91

**6 Summary 93**

**7 Samenvatting 97**

**Appendix A Numerical calculation of the effective potential 101**

**Appendix B Discretisation of the 1D Schrödinger equation on an inhomogeneous grid 105**

**References 109**

**List of publications 117**

**Curriculum Vitae 119**

# *Acknowledgments*

Bij het begin van mijn doctoraat leek deze dag nog eindeloos ver weg. Op dat moment was er ook nog wel een hele weg af te leggen, maar ik ben blij dat ik hem heb kunnen en mogen afleggen.

Nu ik vandaag aan het "eindpunt" ben aanbeland, wil ik dan ook mijn promotor, François Peeters, bedanken voor de jarenlange steun en het vertrouwen. Dankzij u heb ik deze weg kunnen afleggen en ik heb er echt heel veel van bijgeleerd. Verder wil ik ook mijn twee copromotoren Bart en Wim bedanken, voor het beantwoorden van mijn duizenden (of waren het er miljoenen?) vragen. Altijd kon ik bij hen terecht voor echt alle mogelijke dingen – zowel voor fysica-gerelateerde vragen alsook voor bouw-gerelateerde vragen... nietwaar, Bart ;-)

To all members, previous members and visitors of the CMT group: thanks for creating a nice atmosphere here! Special thanks to my office mates Michaël and Bin, and also my previous office mate Yosyp, for keeping up with me and always listening to what I have to say.

Verder moet ik ook mijn familie, collega's en vrienden bedanken voor alle steun en de leuke momenten: Katrijn, Erik, Jacques, Damiaan, Tobias,... enz. Bedankt voor de hulp met de TEX-tekeningetjes, de interessante lunches met imitaties van allerlei beesten, het lezen van horoscopen, het oppeppen (specialiteit van Katrijn!), het discussiëren over dromen (ik ben echt al veel geruster nu Jacques heeft berekend dat het heelal niet zal Bose-Einstein condenseren en wetende dat Katrijn en Erik altijd daar voor mij zullen zijn als ik uit de lift kom :-P). Ik ga jullie echt missen!

Tot slot, is ook de steun en het vertrouwen van mijn lieve echtgenoot Tim onmisbaar geweest. Ik weet niet wat ik had moeten beginnen zonder jou.

*This work was supported by the Flemish Science Foundation (FWO-Vl), the Belgian Science Policy (IAP), the EU network of Excellence: Sandie, BOF-TOP (University of Antwerp) and the UA-IMEC, vzw collaborative project.*

# *List of abbreviations*

*(in alphabetic order)*

| **Abbreviation or symbol** | |
|---|---|
| 1D (2D, 3D) | one-(two-, three-) dimensional |
| AFM | atomic force microscopy |
| CMOS | complementary metaloxidesemiconductor |
| CNT | carbon nanotube |
| CVD | chemical vapor deposition |
| DOS | density of states |
| EBL | electron beam lithography |
| EL | electroluminescence |
| EUV | extreme ultra violet |
| FEM | finite element method |
| FVM | finite volume method |
| FE-SEM | field emission scanning electron microscopy |
| IR | infrared |
| MBE | molecular beam epitaxy |

| Abbreviation or symbol | |
|---|---|
| ML | monolayer |
| MOSFET | metal-oxide-semiconductor field effect transistor |
| MOVPE | metal-organic vapor phase epitaxy |
| NW | nanowire |
| PDE | partial differential equation |
| PL | photoluminescence |
| SEM | scanning electron microscopy |
| SLS | solid-liquid-solid |
| UV | ultraviolet |
| VLS | vapor-liquid-solid |

# 1

# Introduction

It would be hard to imagine what today's world would look like without the rapid development in microelectronics technology. Downscaling of circuits, sensors and other devices has opened up a whole new world of possibilities. It also led us to the field of nanotechnology, an exciting and rapidly expanding research area that crosses the borders between the physical, life and engineering sciences. It is worth pointing out that the word "nanotechnology" has become very popular nowadays and is used to describe research and development at dimensions of roughly 1 to 100 nm. "*ὄ νανος*" means dwarf in Greek and "*nano*" is nowadays used as a prefix in metric unit systems to describe a billionth of a unit, for instance nanometer - one billionth of a meter or 0.000000001 m ($10^{-9}$m). Modern nanotechnology research has three corner stones: *fabrication* of nanostructures, *measurement and characterization*, and *theoretical calculations and simulations*. In this thesis, I would like to focus on the *theoretical* part of several topics in nanotechnology and contribute to the knowledge and modeling of them.

In the first part of my thesis, I will discuss optical properties of nanowires (NWs). NWs are the main subject of this thesis, therefore a large part of this introduction will also be devoted to them. The main goal in the first three chapters about NWs is a theoretical study of the excitonic properties in semiconductor wires. Excitons form the basis of optical properties of devices, producing broad or sharp absorption and photoluminescence (PL) lines. The confinement of the electron and the hole and the material surrounding the NW is responsible for the properties of the exciton. Confinement of the particles can be controlled through the size of the NW, whereas the material surrounding the NW can cause significant changes in the PL peak positions. Therefore,

theoretical investigations of excitons in NWs are required to provide valuable information about NW characteristics, such as the PL spectrum. Excitons also reflect the intrinsic nature of low-dimensional systems and therefore one-dimensional[1] (1D) NWs are an ideal platform to probe properties which may be inaccessible or hard to achieve in larger devices, due to the reduced device size.

While low-dimensional materials, such as nanotubes, NWs, nanoparticles etc., have properties that make them attractive as potential solutions to future technology needs, significant progress in research is still required for them before they can be used on a large scale [1]. These wires are expected to play an important role as interconnects as well as active components in future applications such as transistors [2, 3, 4, 5], diodes [6, 7], memory elements [8], lasers [9, 10, 11], chemical and biological sensors [12, 13], decoders [14], etc. Together with carbon nanotubes (CNTs), NWs were proposed to sustain the historical scaling trend beyond CMOS (Complementary Metal-Oxide-Semiconductor). To date, great efforts and progress have been made in the field of CNTs, although CNT based applications are still hindered by difficulties to produce uniform, semiconducting nanotubes. The nature of the CNT depends on the chirality of the rolled-up graphene sheet and is - up to now - not yet fully controllable. On the other hand, semiconductor NWs have several interesting advantages. First, NW devices can be assembled in a rational and predictable manner because the size, interfacial properties, and electronic properties of the NWs can be precisely controlled during NW growth. Moreover, reliable methods exist for their parallel assembly [15]. Secondly, it is possible to combine distinct NW building blocks in ways not possible in conventional electronics to produce semiconductor NW devices that achieve new functionalities and therefore could lead to unexpected device concepts. Finally, the structure of NWs can be designed both axially and radially in a well controlled way for integrating materials of different composition and possible crystal structure into a single component with numerous possibilities. The growing popularity of NWs as a future building block in devices is remarkable and can be quantified in terms of the rapidly increasing number of publications per year since the early 1990s (Fig. 1.1)[2].

In the second part of this thesis I will briefly discuss the importance of impurities in wires and planar nanostructures. Nowadays, the realization of device components containing impurities placed with atomic precision has been achieved [16]. It was demonstrated that these single dopants strongly affect the behaviour of low-dimensional systems. For instance, in transport experiments, the acceptor impurity enhances tunneling in a planar MOSFET (Metal-Oxide-Semiconductor Field Effect Transistor) via its resonant levels

[1] In the context of nanowires, "one-dimensional" is used when the wires have a radius $R$ of the order of nm and a length $L$ in the order of $\mu$m, thus $R \ll L$.

[2] Obtained from www.scopus.com by performing a search on publications containing "nanowire(s)" or "quantum wire(s)" in the abstract, title or keywords.

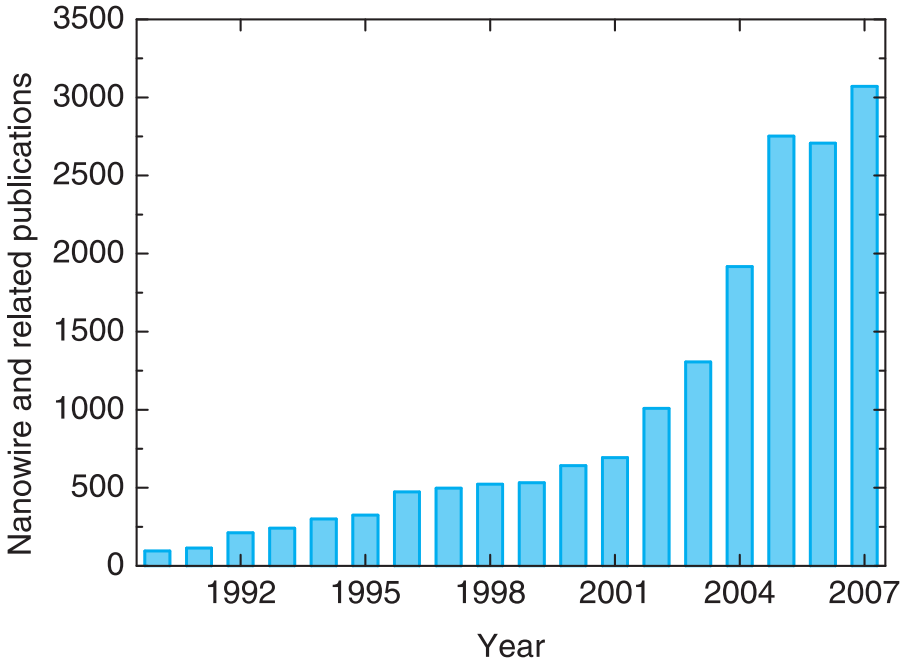


*Fig. 1.1* Plot showing the number of published papers related to nanowires each year since the early 1990s.

[17, 18]. Sellier *et al.* [19] have studied the effect of impurities on the electrical transport in a semiconductor NW and it was claimed that tunneling through donors is responsible for certain features in the conductance of a gated NW. Furthermore, the use of simple donors in Si has been proposed recently in the light of realizing a solid state quantum computer [20, 21]. In this thesis, I will have a closer look at the low energy spectrum of a single dopant placed near a metallic gate, because of their significant effect on electrical and optical properties. Thus, it is crucial to have a good understanding of the underlying mechanisms of donor impurities for both transport and qubit applications.

In this introductory chapter, I present the general background of this work. To get a better understanding of NWs, I will review some of the most important and promising techniques used to build and engineer a NW. Then, I will discuss some applications of NWs, including those related to the implantation of donor impurities. Some fundamental concepts such as band structure and the effective mass approximation, which is adopted throughout this thesis, will be introduced, together with the notion of excitons, trions and biexcitons. The techniques used to solve the Hamiltonian of the system, i.e. the finite difference technique and the finite element technique, will be briefly discussed. Finally, I will give an overview of the thesis.

## 1.1 NANOWIRE GROWTH

It is virtually impossible to review all techniques to grow nanowires. Therefore the two main-stream approaches are discussed in the next sections, with special focus on the one leading to the type of nanowires that I consider in this thesis. In general, these two different approaches for creating nanoscale objects are top-down and bottom-up. The difference between both approaches is quite straight-forward: the top-down approach is a physical approach in which a sample can be downsized using e.g. lithographical techniques, mechanical printing techniques, etc. The bottom-up approach, being rather chemistry oriented, attempts to build the nanostructures from scratch in a controllable environment that allows a well-defined growth of the nanowire.

A good understanding of the growth mechanism is crucial for generating one-dimensional nanostructures of the desired material, size, and morphology. This knowledge enables us to assess which of the experimental parameters controls important parameters of the nanowire, as well as the ease of tailoring the synthesis to form more complex heterostructures.

### 1.1.1 Top-down technique

Several techniques are nowadays available to create a surface pattern of less than 100 nm. One of them, optical lithography, is a relatively mature field because of the wide-spread use in microelectronic chip manufacturing [22]. Photolithography transfers the various circuit design patterns onto a silicon wafer by projecting a uniform beam of laser light through a shadow mask and then focusing it onto a photosensitive "photoresist" material that coats the silicon wafer. Subsequent development, etching, and material deposition steps form the circuit features. Short-wavelength sources, such as extreme ultraviolet (EUV) and X-rays, have been exploited to allow lithographic printing techniques to reach dimensions from 100 to 10 nm. Unfortunately, most of the optical and other lithography techniques encounter several problems, such as high costs, slow production or the inability of sufficient downscaling.

Printing techniques in which mechanical deformation of the patterning media is obtained have been extended to surprisingly small sizes of about 20 to 40 nm. The details of these techniques vary, but they are all based on making a master "stamp" by a high-resolution technique such as electron beam lithography (EBL) and then applying this stamp to a surface to create the pattern. It is seen as a potentially simple and inexpensive technique, however, the current reliance on other lithography techniques to generate the template imposes an important barrier. For the sake of the industry, many efforts have been made to improve all kinds of lithographic techniques, however it is becoming increasingly challenging to postpone the end of lithography [1].

Very recently [23], a new method based on low energetic wide ion beam etching has been proposed to reduce the dimensions of various types of micro-

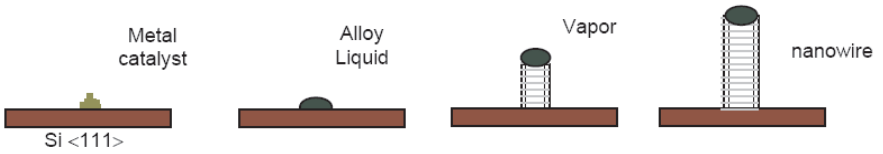


*Fig. 1.2* Schematic of VLS growth of semiconductor nanowires. After deposition of the metallic catalyst on the substrate, a liquid alloy droplet is formed above the eutectic temperature when the vaporized semiconductor material is added. Nanowire growth begins after the liquid becomes supersaturated in the semiconductor material and continues as long as the alloy nanocluster remains in a liquid state and the semiconductor vapor reactant is available (from Ref. [49]).

objects and nano-objects in a predictable and well-controlled way. The authors claim they provide a method which is complementary to existing nanofabrication techniques with the possibility of providing cheap and reliable post-processing enabling sub-10 nm feature formation.

To conclude, it is a challenge for all top-down techniques that, while they work well at the microscale, it becomes increasingly difficult to apply them at nanoscale dimensions. A second disadvantage is that they involve planar techniques, which means that structures are created by the addition and subtraction of patterned layers (deposition and etching), so arbitrary three-dimensional objects are difficult to construct.

### 1.1.2 Bottom-up growth

To synthesize such 1D nanostructures, great efforts were made to improve the development through the vapor-liquid-solid mechanism (VLS). Other bottom-up approaches, such as template-based, solution-based and in-situ growth approaches have also been developed. However, the VLS process seems to be the most successful for generating high quality nanowires with single crystalline structures and in relatively large quantities. Many reviews on NW growth have been written, for some recent and extended reviews on most bottom up approaches, see e.g. Refs. [24, 25, 26].

*1.1.2.1 The VLS growth method* This technique was first discovered in 1964 by Wagner and Ellis at Bell labs [27] to produce micrometer-sized whiskers and recently re-examined by Lieber, Yang, and many other research groups to generate nanowires and nanorods from a rich variety of inorganic materials, such as fundamental semiconductors [28, 29, 30, 31], III-V compounds [32, 33, 34, 35, 36, 37, 38, 39], II-VI compounds [40, 41, 42, 43] and oxides [44, 45, 46]. Generally one starts the synthesis of a nanowire by employing

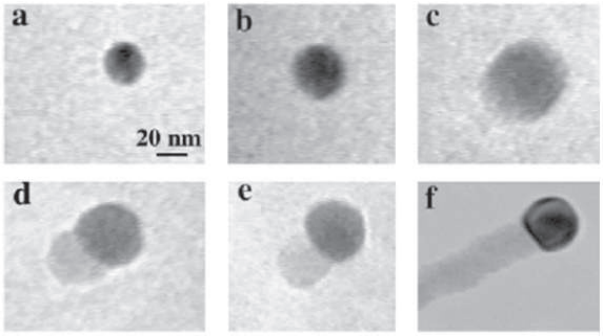


*Fig. 1.3* Birth of a Ge nanowire on a Au nanocluster, as observed using in situ TEM. (a) Au nanocluster in solid state at 500°C; (b) alloying initiates at 800°C, at this stage Au exists mostly in solid state; (c) liquid Au/Ge alloy; (d) the nucleation of Ge nanocrystal on the alloy surface; (e) Ge nanocrystal elongates with further Ge condensation and eventually forms a wire (f) (from Ref. [50]).

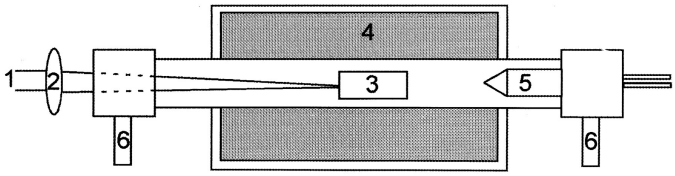


*Fig. 1.4* Schematic view of the nanowire growth apparatus. The output from a pulsed laser (1) is focused (2) onto a target (3) located within a quartz tube; the reaction temperature is controlled by a tube furnace (4). A cold finger (5) is used to collect the product as it is carried in the gas flow that is introduced (6, left) through a flow controller and exits (6, right) into a pumping system (from Ref. [28]).

metal nanoclusters as a catalyst. In the presence of a vapor-phase source[3] of the semiconductor material, the metal nanoclusters are heated above the eutectic temperature that depends on the envisaged metal-semiconductor system. This will result in a semiconductor-metal alloy liquid droplet. When a sufficient concentration of the semiconductor vapor is present, the liquid droplet will become supersaturated and crystalline material precipitates underneath the metal particle. The solid-liquid interface provides the growth interface, which acts as a sink causing the continued incorporation into the lattice and, thereby, the growth of the nanowire with the alloy droplet on

[3]To bring the material into the gaseous phase, many techniques for thin-film growth were already known and have been used to produce wires (e.g. laser ablation [28], chemical vapor deposition (CVD) [47], molecular beam epitaxy (MBE) [48], etc. A flow of precursor gas such as Argon is used to transport the vapor to the substrate.

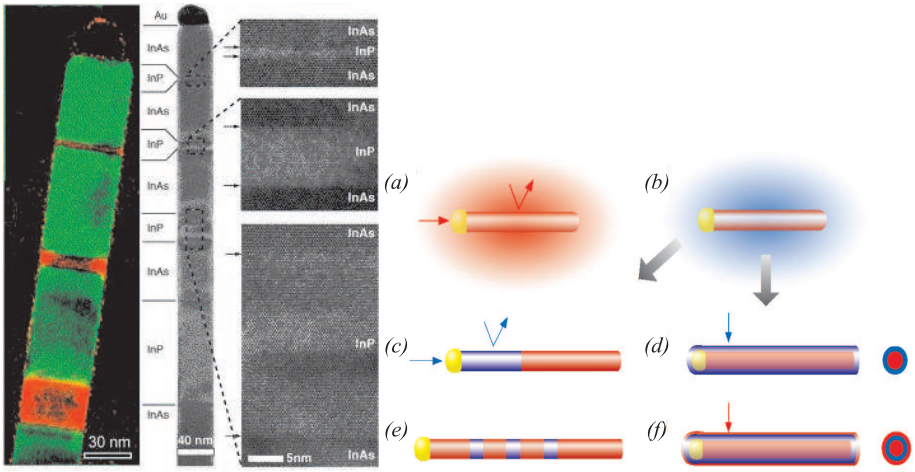


*Fig. 1.5* Left: Color-coded representation of the origin of diffraction spots from the two lattices of InAs (green) and InP (red). Right: high-resolution electron microscope image of the same structure from which can be seen that the multiple layer structure of alternating segments are perfect from a crystalline point of view, free of strain within less than 10 nm from the interface, and have an interface abruptness on the atomic level (from Ref. [51]).

*Fig. 1.6* Nanowire heterostructure synthesis. (a) Preferential reactant incorporation at the catalyst (growth end) leads to one-dimensional axial growth. (b) A change in the reactant leads to either (c) axial heterostructure growth or (d) radial heterostructure growth depending on whether the reactant is preferentially incorporated (c) at the catalyst or (d) uniformly on the wire surface. Alternating reactants will produce (e) axial superlattices or (f) core-multishell structures (from Ref. [52]).

the top (see Fig. 1.2 for a schematic representation of the nanowire growth). Transmission electron microscope (TEM) images also support the idea of the mechanism explained here, as can be seen in Fig. 1.3. A schematic picture of the growth machine is shown in Fig. 1.4. The laser is used to ablate targets containing the element wanted in the nanowire and the metal catalyst component. Many parameters can be varied during the growth process, which can result in nanowires with different growth direction, size, material composition, etc. For instance, adding different targets to the growth machine in Fig. 1.4 enables one to switch between different materials. The ability to produce heterostructures is seen as one of the key advantages of the VLS growth. Both axial heterostructures, in which sections of different materials with the same diameter are grown along the wire axis (Fig. 1.5 and Fig. 1.6(e)), having interfaces that are abrupt on an atomic scale and free of defects, as well as radial heterostructures, in which core-shell (Fig. 1.6(d)) and core-multishell (Fig. 1.6(f)) forms along the radial direction have been realized on VLS grown nanowires.

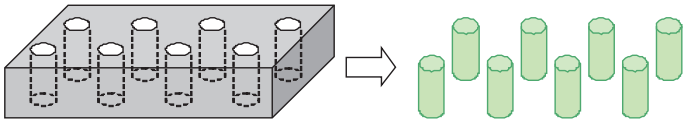

*Fig. 1.7* Schematic drawing illustrating the formation of nanowires by filling the pores within a porous membrane with the desired material.

The ability to use several materials in a nanowire also gave rise to a slightly different way of nanowire VLS growth, namely the self-catalytic growth. In this case, one of the nanowire materials serves as a catalyst. Stach *et al.* [53] demonstrated all the steps of the VLS growth method in the self-catalytic growth process. By heating a GaN thin-film in a vacuum of $10^{-7}$ torr, decomposition of the GaN film occurred and lead to the formation of isolated liquid Ga nanoparticles. The resultant vapor species, composed of atomic nitrogen and diatomic or polymeric GaN then redissolved into the Ga droplets and initiates VLS growth after supersaturation of the metal and establishing a liquid Ga/solid GaN interface. A great advantage of this technique is that the use of foreign material is no longer necessary, reducing the risk of contamination of the nanowire.

Furthermore, it is known that the size of the alloy liquid droplet is predominantly controlling the diameter of the wire. Most semiconductor nanowires assembled through the VLS method are grown along the $\langle 111 \rangle$ direction [42]. However, also other growth parameters such as temperature can have an effect on the nanowire growth direction: Cai *et al.* [54] showed that at 390°C most ZnSe wires of about 10 nm grow along the $\langle 111 \rangle$ direction. At 530°C wires in the diameter range of 10-20 nm grow along the $\langle 110 \rangle$ or $\langle 112 \rangle$ direction, whereas wires with diameters smaller than 10 nm always grow along the $\langle 110 \rangle$ direction. In general, the crystallographic orientation of the nanowire growth is chosen to minimize the total free energy, since the process is thermodynamically driven.

*1.1.2.2 Template-mediated growth* Another popular growth method of wires uses templates, which was first demonstrated by Martin *et al.* [55]. The nanowire material can be crystallized into the pores of an alumina or polymer film, whose pores usually are cylindrical. The only requirement to obtain NW growth seems to be that the wire material can be loaded into the pores using vapor-phase sputtering, liquid-phase injection or solution-phase chemical or electrochemical deposition. One end of the template is plated with a metal and can be used as an electrode. Wires with diameters and lengths determined by the size of the pores are the result. After NW growth, the template itself is removed through a corrosive etch enabling one to recover the wires (Fig. 1.7). These template-mediated grown wires usually form polycrystalline materials, however under certain growth conditions it is possible to achieve crystalline wires.

*1.1.2.3 Solution based growth* Semiconductor wires have also been assembled in a solution [56]. One of these types of growth method, the solution-liquid-solid or SLS, resembles the VLS growth method, although some fundamental differences are present. The main difference between VLS and SLS is that the catalysts particles have melting points below $\propto 400°C$. It was found that the extremely small size of the metal catalysts guarantees the activation of NW growth even at low temperatures. Also, the wires can be crystallized in a solution without the use of templates or substrates. Therefore, solution-phase synthesis is not limited by the density of pores in a template or by the close packing of nanoparticles on a substrate. Yields can therefore be higher and reactions can be scaled up. The SLS process can be described as follows [57]: a solution phase molecular precursor thermolyzes to give elements of the desired semiconductor. These particles then solubilize within the catalyst particles until supersaturation. The surface of the nanoparticles serves as a heterogeneous nucleation site for the semiconductor where nucleation crystal growth leads to a NW. Organic surfactants in solution passivate the surface of the NW, preventing and suppressing any transverse growth [25].

*1.1.2.4 Strain induced growth* An alternative bottom-up growth method is based on the anisotropic stress caused by growth under certain conditions. Spontaneous wire formation was demonstrated by Fuster *et al.* [58]. In their experiments, InAs was grown on an InP substrate. Due to a 3.2% lattice mismatch, the accumulated stress will increase linearly as InAs is deposited on the InP substrate. At a certain InAs coverage, the 2D layer is not energetically favourable anymore and relaxation starts by the formation of self-assembled nanostructures. This can be seen on $1 \times 1\ \mu m^2$ AFM (atomic force microscopy) images shown in Fig. 1.8. The InP surface before InAs deposition is shown in Fig. 1.8(a): we can see the steps in the surface, due to the unintentional miscut angle of the InP $\langle 001 \rangle$ wafer. When the As flux reaches the surface (Fig. 1.8(b)), the InAs surface produced by As/P exchange exhibits a more regular step distribution. At 2.3 ML of InAs in Fig. 1.8(c), 1 ML high islands elongated along the $\langle 1\bar{1}0 \rangle$ direction are formed starting at the step edges. Relaxation of the built up stress will occur around 2.5 ML (Fig. 1.8(d)), when wire formation clearly starts: an asymmetric isolated 3D structure arises. When further increasing the flux InAs, more wires start to form along the $\langle 1\bar{1}0 \rangle$ direction (Figs. 1.8(e)-(f)). The final result is an array of wires with an average length/width ratio of around 8.

*1.1.2.5 Difference between strain induced growth and VLS growth* The wires that I discussed in the previous paragraph, i.e. wires obtained through strain-induced growth, are spontaneously formed wires and are capped by InP, resulting in wires of InAs surrounded by InP. These wires are therefore fundamentally different from the wires we discussed earlier in the VLS growth method. In these cases, the dielectric constant of the wire material is of the order of 10, whereas the surrounding material usually has a dielectric constant

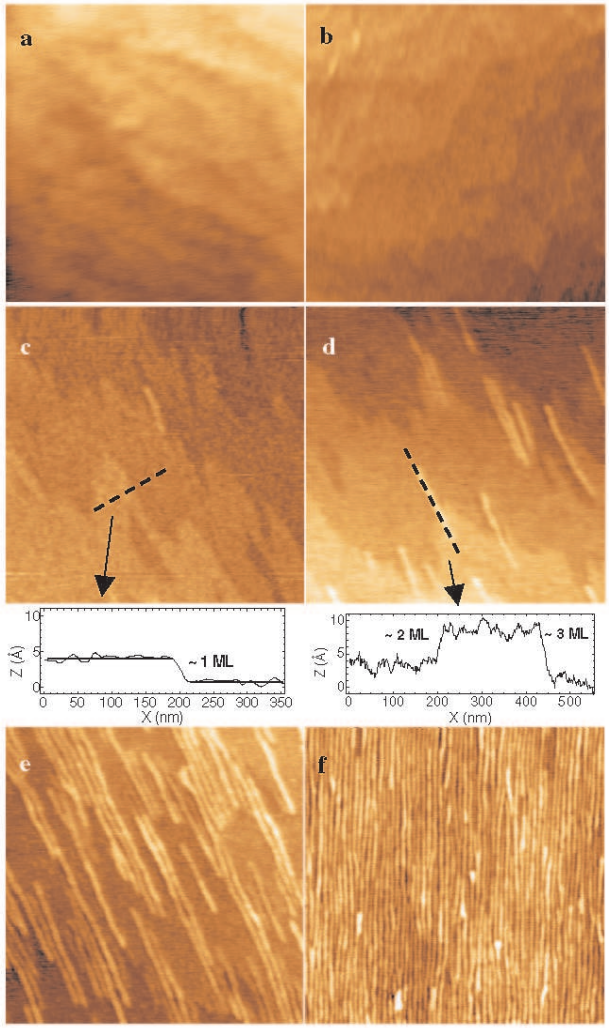


*Fig. 1.8* $1 \times 1\mu m^2$ AFM images ((a)-(f)) 0, 1, 2.3, 2.5, 2.7 and 3.5 ML of InAs grown on InP$\langle 001 \rangle$, respectively. Profiles along the direction of the dashed lines drawn on (c) and (d) are also shown. The elongated islands (c) and the quantum wires ((d)-(f)) are always aligned along the $\langle 1\bar{1}0 \rangle$ direction.

$\propto 1$. Here, the dielectric constant of InAs is 12.4, whereas for InP we find 14.6. The ratio between both constants, i.e. the dielectric mismatch, is close to 1 and therefore has negligible effects on the wires excitonic properties. In this thesis however, I will pay especially attention to wires with a non-negligible mismatch effect.

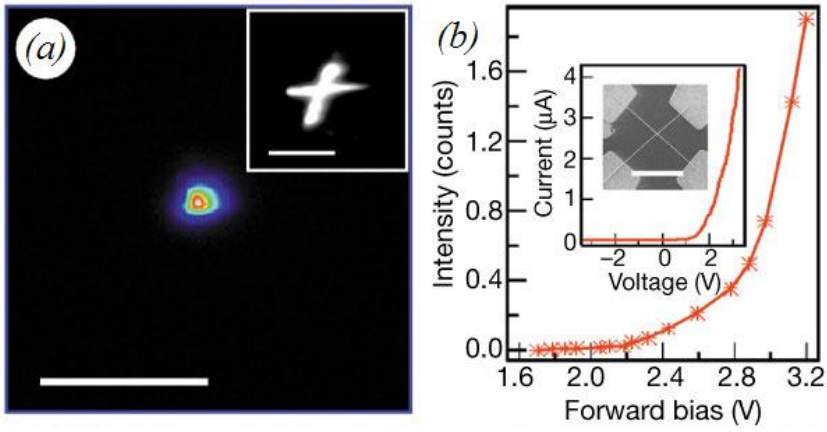


*Fig. 1.9* (a) Electroluminescence (EL) image of the light emitted from a forward-biased nanowire p-n junction at 2.5 V. Inset: photoluminescence (PL) image of the junction. Scale bars are 5 $\mu$m. (b) EL intensity versus voltage. Inset: I-V characteristics. Inset in this inset: FE-SEM image of the junction itself. Scale bars are 5 $\mu$m. The n-type and p-type nanowires forming this junction have diameters of 65 and 68 nm, respectively (from Ref. [7]).

## 1.2 NANOWIRE APPLICATIONS

Numerous applications have been realized over the last decade. NWs have proven to possess some superior qualities over thin films or the particle counterparts, thanks to their high surface to volume ratio. This advantage makes them excellent candidates for opto-electronic [6, 7, 9, 10, 11] and sensing [12, 13] applications. Their shape also suggests they are exceptional candidates for transistors [2, 3, 4, 5] and they have also been used as memory elements [8]. In this section I will give examples of the applications that have been realized to show the NW potential.

### 1.2.1 Diodes

An example of a nanowire diode has been realized several years ago by Duan *et al.* [7]. They formed junctions by crossing n-type and p-type InP wires that were prepared by VLS growth. Because these NWs can be easily produced in bulk quantities, they are a readily available material for assembling devices and device arrays. The photoluminescence (PL) and electroluminescence (EL) was studied from crossed p-n junctions. Fig. 1.9 (a) (inset) shows two crossed wire-like structures, and comparison of the EL (main figure) and PL (inset) images, shows that the position of the EL maximum corresponds to the crossing point in the PL image, demonstrating that the light originates

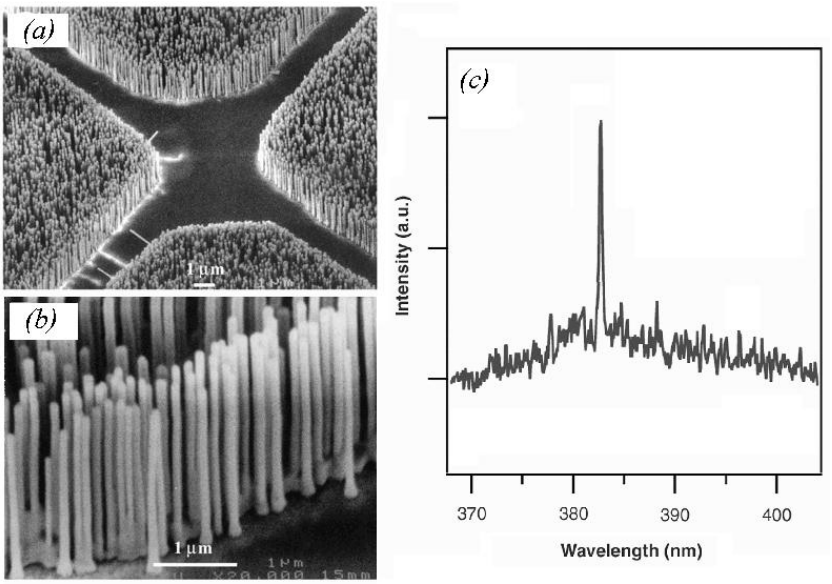


*Fig. 1.10* (a) SEM image of a ZnO nanowire 'nanoforest' grown on a sapphire substrate. (b) Zoom of (a). (c) Emission spectrum from nanowire arrays above the lasing threshold. The pump power for this spectrum is 150 kW/cm$^2$ (adapted from Ref. [9]).

from the nanowire p-n junction. The EL maximum is found at 820 nm for the set of wires in Fig. 1.9. The EL versus voltage (1.9 (b)) shows that significant light can be detected already at low voltages. The $I - V$ characteristic (1.9 (b) (inset)) shows clear rectification with a sharp current onset at $\sim$ 1.5 V. When thinner wires were used (39 and 49 nm), a larger blueshift was obtained and the EL peak emission occured at 680 nm. The results suggest that this blueshift may be due to quantum confinement.

### 1.2.2 Lasers

Short-wavelength blue-light lasers an UV lasers play important roles in laser printing and information storage. We all know that CD read-heads require short-wavelength operating lasers. Because the density of storage in an optical memory system is inversely proportional to the square of the wavelength of the operating laser, the shorter the wavelength of the operating laser, the higher the informational storage on the CD. NWs have been demonstrated to be excellent laser cavities for producing laser beams with wavelengths ranging from ultraviolet (UV) to infrared (IR). Huang *et al.* [9] showed that lasing activity at room temperature is possible with ZnO nanowires. ZnO is a compound semiconductor which has several properties that are a perfect match

with the requirements for room temperature UV lasers. Firstly, the material has a wide bandgap of 3.37 eV and secondly, the exciton binding energy is about 60 meV, which is significantly higher than the thermal energy at room temperature ($\sim$ 26 meV). Furthermore, the material is synthesized into a nanostructure in which quantum size effects yield a substantial density of states at the band edges and enhances radiative combination due to carrier confinement. The ZnO wires in their experiments were grown vertically on a substrate with the VLS growth method, using a Au catalyst. The diameters of these wires range from 20 nm to 150 nm, whereas more than 95 % of them have diameters of 70 to 100 nm. The wires have an areal density of $1.1 \times 10^{10}$ $cm^{-2}$ (Fig. 1.10 (a)-(b)) and produce strong emission (Fig. 1.10 (c)). The observation of lasing action in these nanowire arrays without any fabricated mirrors is a strong evidence for the assumption that the single crystalline faceted nanowires serve as natural resonance cavities. The wires are in contact with materials of low dielectric constants, producing natural cavities or waveguides with a simple chemical approach instead of cleavage and etching.

Also other materials, for instance $In_2O_3$, has been used to produce UV emitting lasers [11]. These wires were obtained by a template-mediated growth, resulting in wires with an average diameter of 80 nm. It is known that bulk $In_2O_3$ can not emit light at room temperature, but in the form of nanowires, strong and sharp PL emission centered at 398 nm was obtained.

### 1.2.3 Transistors

In the previous section I discussed several growth methods and also the versatility of the VLS growth method. This method allows for core-shell growth of wires, a great advantage for device development. A device grown in this way also has some important advantages over its planar counterparts, such as a capacitance enhancement. Lauhon *et al.* [3] used a core-multishell wire, as shown in Fig. 1.11. The building blocks used to fabricate the coaxial FET consists of a p-type Si core, surrounded by i-Ge (intrinsic Ge), which is the active region of the FET. Source and drain were made by material deposition onto the i-Ge part of the wire. A shell of $SiO_x$ prevents current leakage into the last shell: a shell of p-type Si which is surrounded by the gate electrode. Transport measurements on these devices show very good performance characteristics and can be understood as follows: the all-round gate is capable of fully 'squeezing' the conduction channels in the wire, until no current can pass anymore. On the other hand, gate can 'open up' the nanowire channels, depending on its potential. These results are without any doubt of significant importance, because they represent a lower limit to what may be achieved. Further optimization of the device could lead to even more improvements, e.g. Ref. [59] suggests that the application of a high-k dielectric layer to the nanowire provides opportunities towards the realization of nanoscale electronic devices with ultrahigh performance.

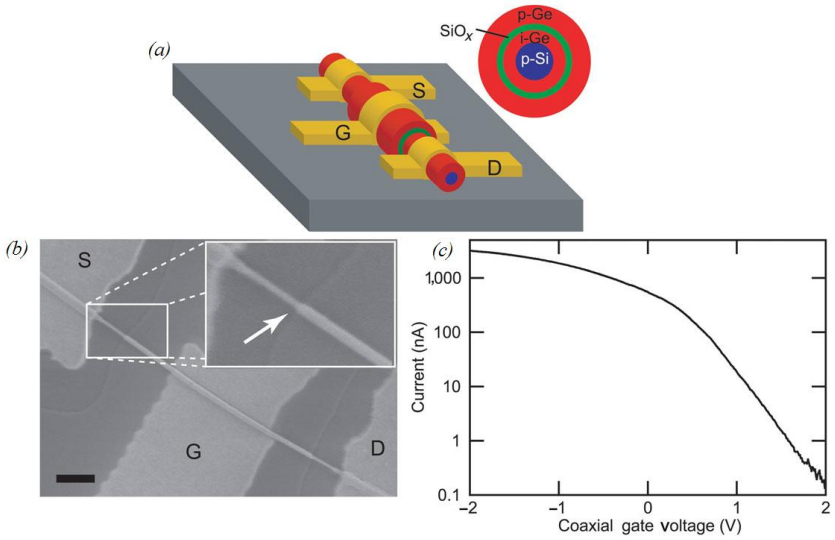


*Fig. 1.11* (a) Device schematic showing transistor structure. The inset shows the cross-section of the nanowire, starting with a p-doped Si core (blue, 10 nm) with subsequent layers of i-Ge (red, 10 nm), $SiO_x$ (green, 4 nm), and p-Ge (5 nm). The source (S) and drain (D) electrodes are contacted to the inner i-Ge core, while the gate electrode (G) is in contact with the outer p-Ge shell and electrically isolated from the core by the $SiO_x$ layer. (b) Scanning electron micrograph (SEM) of a coaxial transistor. Source and drain electrodes were deposited after etching the Ge and $SiO_x$ layers to expose the core layers. The etching of these outer layers is shown clearly in the inset and is indicated by the arrow. Scale bar is 500 nm. (c) Gate response of the coaxial transistor at $V_{SD} = 1$ V. Charge transfer from the p-Si core to the i-Ge shell produces a highly conductive and gateable channel (from Ref. [3]).

### 1.2.4 Sensors

As we discussed in the previous paragraph, nanowires can also be assembled as field-effect transistors (FETs), which exhibit a conductivity change in response to variations in the electric field or potential at the surface of the device. The dependence of the conductance on gate voltage and corresponding charge at the gate electrode/dielectric interface makes FETs natural candidates for electrically based sensing, since the binding of a charged or polar biological or chemical species to the gate dielectric is analogous to applying a voltage using a gate electrode. The one-dimensional morphology of wires is a great advantage over planar FET sensors in order to overcome the sensitivity limitations. This increased sensitivity may even lead us to the point that single-molecule detection is possible in the future [60]. Cui *et al.* [12] assembled boron-doped Si nanowires into a nanosensor that can detect changes in

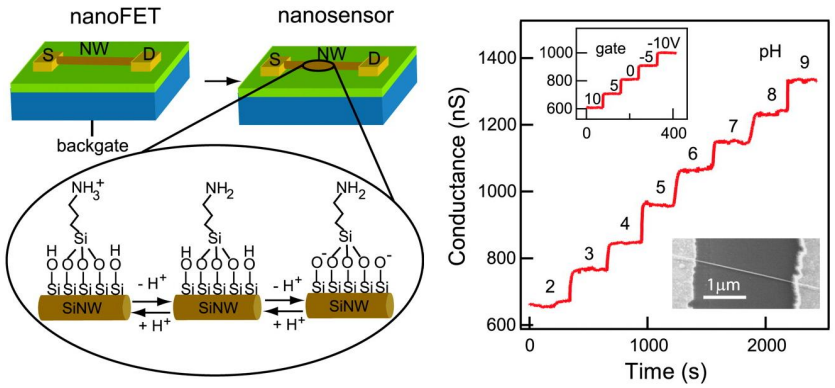


*Fig. 1.12* Left: Schematic illustration of the conversion of a NW FET into NW nanosensors for pH sensing. The NW is contacted with two electrodes, a source (S) and drain (D), for measuring conductance. Zoom of the APTES-modified SiNW surface is shown, illustrating changes in the surface charge state with pH. Right: Real-time detection of the conductance for an APTES-modified SiNW for pHs from 2 to 9; the pH values are indicated on the conductance plot. Top inset: Plot of the time-dependent conductance of a SiNW FET as a function of the back-gate voltage. Bottom inset: Field-emission scanning electron microscopy image of a typical SiNW device (from Ref. [12]).

the pH of a solution. This was obtained by modifying the silicon oxide surface with 3-aminopropyltriethoxysilane (APTES) to provide a surface that can undergo protonation and deprotonation, where changes in the surface charge can chemically gate the SiNW. The single-crystal p-type SiNWs used in these studies were prepared by a nanocluster-mediated VLS growth method. Linear current (I) versus voltage (V) behavior was observed for all of the devices studied, which shows that the SiNW-metal contacts are ohmic, and applied gate voltages produced reproducible changes in the I-V.

Their device is based on a covalent link of APTES to the SiNW oxide surface, resulting in a surface terminating in both -$NH_2$ and -SiOH groups (Fig. 1.12 (left)), which have different dissociation constants. At low pH, the -$NH_2$ group is protonated to -$NH_3^+$ and acts as a positive gate, which depletes hole carriers in the p-type SiNW and decreases the conductance. At high pH, -SiOH is deprotonated to $SiO^-$, which correspondingly causes an increase in conductance. Measurements of conductance as a function of time and solution pH (Fig. 1.12 (right)) demonstrate that the NW conductance increases stepwise with discrete changes in pH from 2 to 9 and that the conductance is constant for a given pH; the changes in conductance are also reversible for increasing and/or decreasing pH. The concept of using NW FETs modified with receptors or ligands for specific detection can be extended in many di-

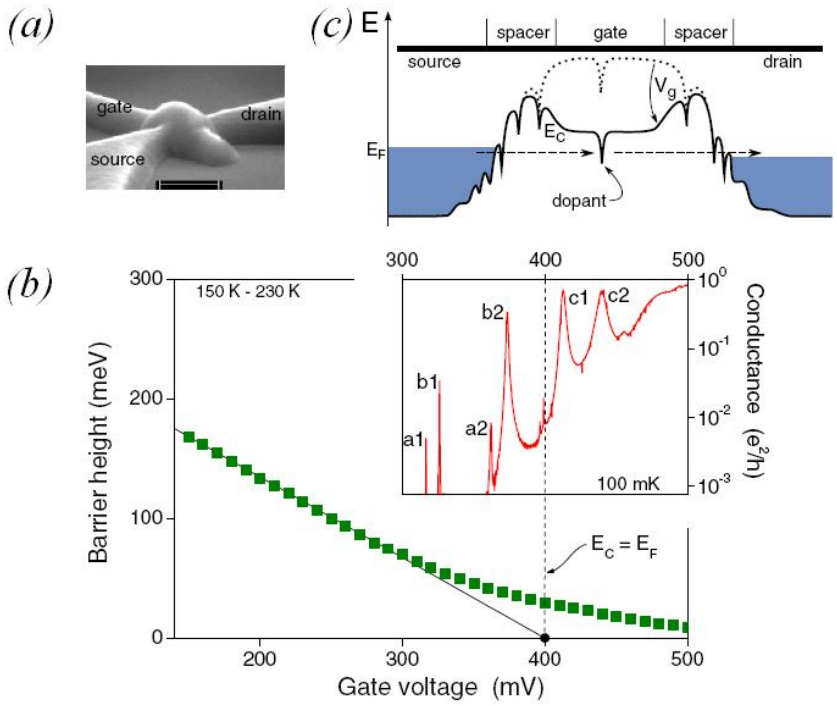


*Fig. 1.13* (a) SEM image of the device. The scale bar is 200 nm. Note how the wire is fully covered by the gate material. (b) Barrier height measurments performed at high temperatures (squares). The conduction band edge $E_C$ reaches the Fermi level $E_F$ at 400 mV. Inset: differential conductance measured at low temperature. Peaks a1 to b2 show resonances below threshold, while c1 and c2 are resonances found above threshold. (c) Conduction band profile showing the attractive donor site in the wire. For an applied gate voltage $V_g$, resonant tunneling through the discrete levels of the dopant can occur (from Ref. [19]).

rections. For instance, this procedure has also been used for the detection of proteins, such as streptavidin, and $Ca^{2+}$ ions.

## 1.3 APPLICATIONS INVOLVING SHALLOW DONORS

### 1.3.1 Transistor

In this section I will explain how a dopant in a device can be used as a functional part of it, instead of merely providing charges [19]. A 60 nm tall p-type Si wire is placed on a substrate and is provided with a single n-type dopant. Source and drain are made at the ends of the wire and the gate fully covers the

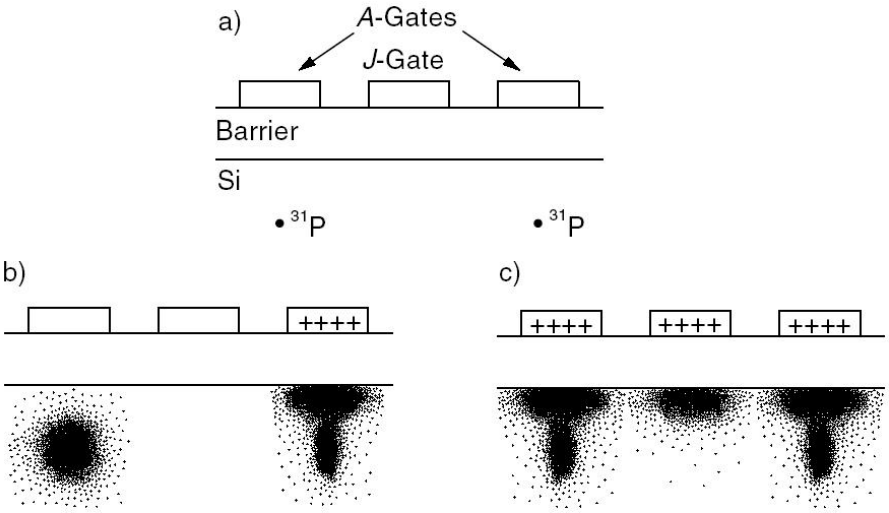


*Fig. 1.14* (a) Schematical picture of the qubit for realizing one and two qubit logic operations: $A$-gates are placed on top of the donors and $J$-gates are located between the donors. (b) A single qubit logic operation is obtained by applying an $A$-gate bias which brings a selected spin into resonance with an external magnetic field. (c) Exchange between two qubits (two qubit operations) can be realized by lowering the potential barrier between the donor sites with the $J$-gate and turning on exchange coupling between the donors. Nuclear spin exchange between donor nuclei will occur thanks to the electrons (from Ref. [21]).

wire along the three other sides of it (see Fig. 1.13(a)). When the temperature is sufficiently low, conductance peaks were found even below the threshold conductance. This is shown in Fig. 1.13(b): the conduction band edge $E_C$ reaches the Fermi level $E_F$ at 400 mV of applied gate voltage. Below this voltage, one would expect no conductance, however, Fig. 1.13(b) (inset) shows several conductance peaks (peaks a1 to b2) which correspond to resonant tunneling through the donor state, as is drawn schematically in Fig. 1.13(c). Above the threshold gate voltage, resonant peaks are still found in the conductance plot. This is possible because of tunneling through a potential well caused by the dopant in the wire. Single dopants in gated nanostructures create thus attracting Coulomb potentials which induces resonances in the subthreshold conductance due to tunneling through their discrete energy levels.

### 1.3.2 Quantum computer

The zeros and ones in classical computers systems can be replaced by the quantum states of a two-level system (qubits). A very promising candidate

for realizing this idea in a quantum computer is a P donor located in a Si-based structure.

In the device that was proposed by Kane [20, 21], the qubits are the donor nuclear spins, and the hyperfine interaction between these and the donor electron spins is used to perform single-qubit operations. The strength of the hyperfine interaction is manipulated by a metallic gate, the so-called $A$-gate (Fig. 1.14), which moves the electron between the donor and the interface. Exchange between neighboring donors, tuned by surface "exchange" gates ($J$-gates), would control two-qubit operations. The ability to move or "shuttle" electrons between a donor and the Si surface using external electric field is an essential element of Si quantum computer architectures because the measurement of the electron spin states can only occur at surfaces whereas the qubit entanglement takes place at the donor sites.

## 1.4 BASIC THEORETICAL CONCEPTS

This section recapitulates a few basis notions of solid state physics that are relevant to the study of semiconducting nanowires.

### 1.4.1 Band structure of bulk semiconductors

The electrons of a single free-standing atom occupy atomic orbitals, which form a discrete set of energy levels. If several atoms are brought together into a molecule, their atomic orbitals split up. This produces a number of molecular orbitals proportional to the number of atoms. When a large number of atoms (of order $10^{20}$ or more) are brought together to form a solid, the number of orbitals becomes exceedingly large, and the difference in energy between them becomes very small, so the levels broaden to form bands of energy rather than the discrete energy levels of the atoms in isolation. However, some intervals of energy contain no orbitals – no matter how many atoms are brought together – forming band gaps. Thus, in solid state physics, the electronic band structure (or simply band structure) of a solid describes ranges of energy that an electron is "forbidden" or "allowed" to have. At temperature $T = 0$, the electrons in a semiconductor fill the electronic bands starting from the lowest one all the way up to the highest energy bands below the bandgap, which form the *valence* bands. Energy levels with an energy above the bandgap are empty and are called the *conduction* bands [61].

The band structure of a material determines several characteristics, in particular its electronic and optical properties. Therefore, it is highly desirable from a theoretical point of view to know this band structure. The band structure can be obtained by solving the Schrödinger equation appropriate for the solid which is of course an enormously complicated problem. Therefore, some approximations are necessary enabling one to solve it. In general, there are

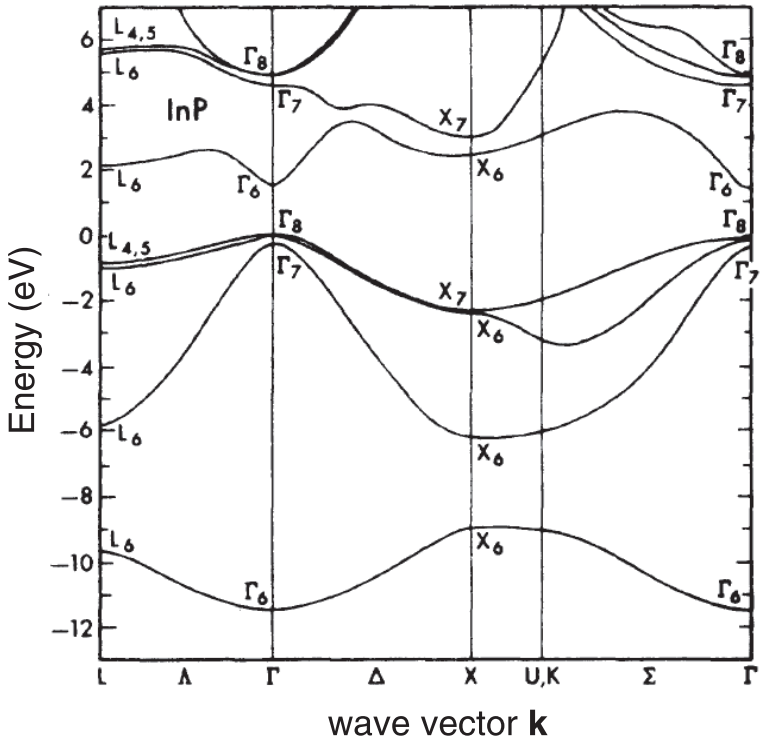


*Fig. 1.15* InP band structure calculated using the pseudopotential method (from Ref. [64]).

two main categories of bandstructure calculation for semiconductors. Firstly, methods which describe the entire valence band and conduction bands, such as e.g. the tight binding method, orthogonalized plane wave methods and pseudopotential methods, and secondly, methods which describe near band-edge bandstructures such as the $\mathbf{k}\cdot\mathbf{p}$ method. An overview of these methods can be found in many textbooks (see for instance Refs. [62] and [63]). The problem of band structure becomes greatly simplified if we are dealing with crystalline materials, which is the case for the NWs. A crystal is a periodic array of atoms which can be described through a Bravais lattice with a basis. The periodical position of the atoms is due to the nature of the bonding. In e.g. a III-V binary compound such as InP, there are 8 outer electrons per unit cell which contribute to the chemical bonds. The other electrons of each kind of atom are "locked" in closed shell configurations and their wave functions are strongly bound around the In or P nuclei. If we neglect the impurities in the crystal (ideal crystal) and we consider the cores of the atoms fixed at their lattice sites, those shared electrons feel a periodic potential generated from the ionic cores in the underlying lattice. The wave function of a single

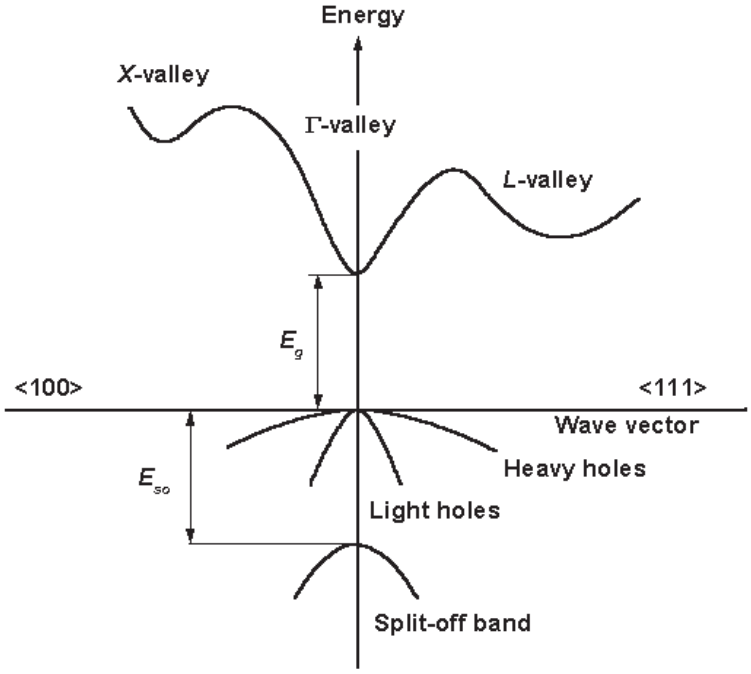


*Fig. 1.16* Energy and wave vector region of interest for typical optical and electrical transport purposes. For InP, the band gap energy $E_g = 1.34$ eV, whereas $E_{\mathrm{SO}} = 0.11$ eV at 300K (from Ref. [65]).

outer-shell electron satisfies the Schrödinger equation

$$\Big[ -\frac{\hbar^2}{2m_0}\nabla^2 + V(\mathbf{r})\Big]\psi(\mathbf{r}) = E(\mathbf{k})\psi(\mathbf{r}), \tag{1.1}$$

where $m_0$ is the free-electron mass. Because the Hamiltonian is invariant under the next translation of the lattice vector the general solution of Eq. (1.1) can be written as

$$\psi_{n\mathbf{k}}(\mathbf{r}) = e^{i\mathbf{k}\cdot\mathbf{r}} u_{n\mathbf{k}}(\mathbf{r}), \tag{1.2}$$

where $u_{n\mathbf{k}}(\mathbf{r})$ has the same periodicity as the lattice. The energy eigenvalue $E$ can be written as $E = E_n(\mathbf{k})$, where $n$ is the band index and $\mathbf{k}$ denotes the wavevector of the electron. The wavefunction $\psi_{n\mathbf{k}}(\mathbf{r})$ is known as the Bloch function. This is the Bloch theorem basically underlying earlier mentioned methods to calculate the band structure for bulk solids. Fig. 1.15 shows an example of the InP band structure which has been calculated using the pseudopotential method. In Fig. 1.16 we see the region of the bandstructure which is important for most physical phenomena in NW related applications.

Depending on the problem one is dealing with, the number of bands taken into account can vary from two (effective mass approximation) up to four, six (Luttinger-Kohn, see Ref. [66]), eight[4] (Kane, see Ref. [67]) and even fifteen for Ge/Si [68], each with increasing accuracy and complexity. Also strain was added to the 8x8 multiband Hamiltonian by Pikus and Bir [69].

In this thesis, we will assume the split-off energy to be large enough, enabling one to neglect this band. Furthermore, we assume that mixing between heavy holes and light holes is negligible and that the wire involves mainly one single type of holes (heavy holes). Therefore, we use the single-band approximation for both holes and electrons. Since we focus on free-standing nanowires, mainly grown by the VLS growth method, there are two major consequences for the model used to describe the system, i.e. a) no strain has to be taken into account, and b) the dielectric mismatch has a non-negligible effect on the electronic properties of the nanowire. This dielectric mismatch is caused by the difference in dielectric constant between the nanowire material (typically of the order of 10) and the surrounding material, often vacuum (dielectric constant is 1).

### 1.4.2 The effective mass approximation

An electron moving in a crystal feels a perfectly periodic background potential, thus the electron propagates without scattering. Indeed, the Bloch theorem states that the electron wavefunction $\propto \exp(i\mathbf{k}\cdot\mathbf{r})$. The effect of the crystal can easily be taken into account, by replacing the free electron mass in the Schrödinger equation by an effective mass. We can define the effective mass starting from the Taylor expansion of the energy of an electron with momentum $\mathbf{k}$ in the vicinity of the minimum of the conduction band at $\mathbf{k} = \mathbf{k_0}$,

$$E_n(\mathbf{k}) = E_n(\mathbf{k_0}) + \frac{1}{2}\sum_{i,j=x,y,z} \left.\frac{\partial^2 E_n(\mathbf{k})}{\partial k_i \partial k_j}\right|_{\mathbf{k}=\mathbf{k_0}} (k_i - k_{i0})(k_j - k_{j0}) + \dots \quad (1.3)$$

where the second derivative of the energy is a positive definite tensor that does not depend on $\mathbf{k}$. This tensor can be used to define a "new" mass $m_e$ of the electron called the *effective mass*, such as

$$\left.\frac{\partial^2 E_n(\mathbf{k})}{\partial k_i \partial k_j}\right|_{\mathbf{k}=\mathbf{k_0}} = \left.\frac{\hbar^2}{2m_e(\mathbf{k})_{\mathbf{ij}}}\right|_{\mathbf{k}=\mathbf{k_0}}. \quad (1.4)$$

It is clear that the effective mass is inversely proportional to the curvature of the band in the point. Note that once the $E$ versus $\mathbf{k}$ relation is established, we can, for all practical purposes, forget about the background potential and treat

[4]Due to spin, each band is twofold degenerate.

the electrons as if they are free and obey the effective Schrödinger equation of motion.

### 1.4.3 Validity of the approximations

The approximations that are made in this thesis are only valid if the system satisfies certain conditions. Firstly, the single-band approximation is no longer valid in cases of strong confinement. Band mixing between the different hole bands occurs and neglecting this effect will no longer be acceptable. Therefore, it is important to realize that all calculations done in this work are valid when the radius of the wire is at least several nm. Secondly, the Coulomb interaction potential can not be treated anymore in a perturbative way, if the wire radius is too large. It should be noted that the kinetic energy is proportional to $1/R^2$, where $R$ is the wire radius, whereas the Coulomb potential energy goes as $1/R$. This means that for confined systems ($R$ small) the Coulomb potential energy is only a perturbation to the single particle kinetic energy. In case $R$ increases too much, the Coulomb and kinetic energy will become equally important. A typical semiconductor such as InP has a minimum kinetic energy of $\propto$ 49 meV for $R = 5$ nm, whereas its Coulomb energy is only $\propto$ 6 meV. Thus, on the one hand the wire radius is not allowed to be too small, but on the other hand, the wire radius should not be too large. Roughly speaking, the "window" of validity is between several nanometers up to several tens of nanometers, depending on the wire material. Wires of that size are easily grown, thus our "window" matches a broad range of experimentally realizable wires. Furthermore, it should be noted that our approach is optimal for direct bandgap materials. For materials with an indirect bandgap, such as Si, one should be more careful. However, the indirect bandgap can be taken care of by using an effective mass, which will depend on the wire's growth direction, that specifically accounts for this different bandstructure.

### 1.4.4 From bulk to low-dimensional systems

When confining particles to a region with a characteristic size of the order of the de Broglie wavelength, quantum mechanical laws come into action. They cause changes in most electronic properties and a bunch of so-called size effects occur. The most fundamental characteristic of an electron system - its energy spectrum - is changing due to additional confinement: the spectrum becomes discrete along the confining coordinate direction. As a consequence, carriers have a non-vanishing minimum kinetic energy, the quantum confinement energy. This feature is of great importance for applications in the laser/detector area. Achieving the desired bandgap enables one to essentially determine the energy of the light emitted and absorbed. Also, the number of available states or the density of states (DOS) changes when confining carriers in one, two or three dimensions. The DOS (Fig. 1.17) for small structures shows that the

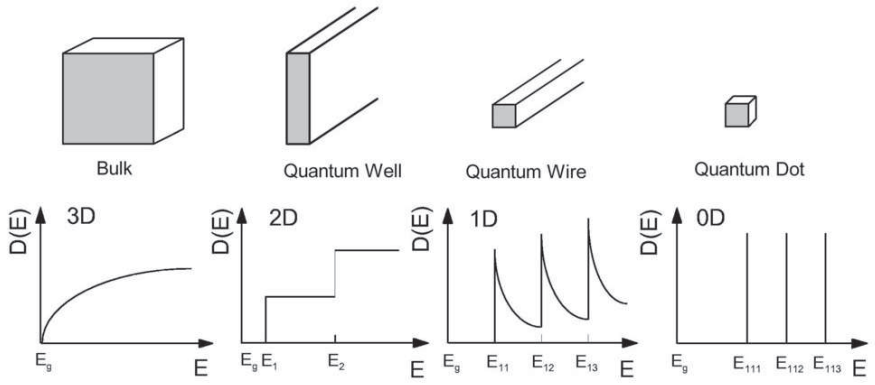


*Fig. 1.17* Density of states (DOS) for bulk, quantum wells, quantum wires and quantum dots (from Ref. [70]).

distribution of electrons changes as dimensionality is reduced. For quantum wells (2D system), a steplike behavior is found, whereas for sufficiently thin wires (1D system), the DOS for certain energies actually becomes higher than the DOS for bulk semiconductors. For quantum dots (0D system), the electrons become quantized to certain energies, which is why quantum dots are also called "artificial atoms". For nanowires, the concentration of electrons and holes populating the conduction band and valence band is largest near the band edges, which makes such quantum structures more attractive for a laser device. The discretisation of the energy levels also means that optical transitions will be sharper (i.e. sharper lines in the output frequency will be produced). As a result, these quantum size effects significantly reduce the threshold current density and its temperature dependence, and shorten the emission wavelength.

### 1.4.5 Excitonic complexes: Excitons and trions

In Sect. 1.4.1 I discussed the band structure of semiconductors. Until now, the assumption was made that the valence bands are filled and the conduction bands are empty. It is, however, possible to excite electrons from the valence band to the conduction band, using a laser of the appropriate wavelength. Due to the Coulomb interaction, this conduction electron is now attracted to the hole left in the valence band. This new state of a bound electron-hole pair is called an *exciton*. The electronic band structure is now modified into a slightly different one, where not only valence band and conduction band exists now, but also exciton energy levels in the bandgap area (see Fig. 1.18. The existence of excitons was also confirmed experimentally (see Fig. 1.19): absorption peaks below the bandgap, corresponding to excitonic energy levels,

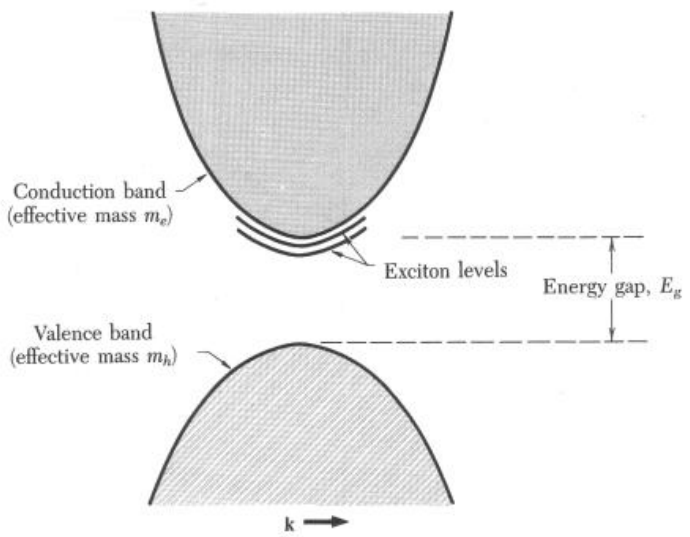


*Fig. 1.18* Schematic representation of the band structure, showing the dispersion for conduction bands, valence bands and the exciton energy levels. Since the Coulomb interaction is attractive, these levels are found in the band gap (from Ref. [61]).

appeared in the absorption spectrum as temperature becomes sufficiently low. Excitons are electrically neutral, do not transport charge and can move freely through the crystal as quasi-particles with mass $M = m_e + m_h$, where $m_e$ and $m_h$ are the effective electron and hole masses, respectively. The characteristic energy spectrum of the exciton is easily obtained by making the comparison with the hydrogen atom: in bulk, the exciton ($X$) binding energy becomes

$$E_X = -\frac{\mu e^4}{2\epsilon^2 \hbar^2}, \tag{1.5}$$

where $e$ is the free electron charge, $\epsilon$ is the dielectric constant and $\mu = m_e m_h/(m_e + m_h)$, the mass of the exciton's relative motion. For a typical semiconductor such as GaAs, one can obtain an exciton binding energy of 4.2 meV. As opposed to bulk, nanostructures have additional size-dependent components in the expression for the energy due to the electron and hole confinement,

$$\begin{array}{lcll} E_{\rm tot} & = & E_g + E_X & \text{(bulk)} \\ E_{\rm tot} & = & E_g + E_e + E_h + E_X & \text{(nanostructure).} \end{array}$$

The exciton binding energy also depends on the dimensions of such structures because both the electron and hole bound by the Coulomb interaction in addition are also confined by the conduction and valence band offset. Fur-

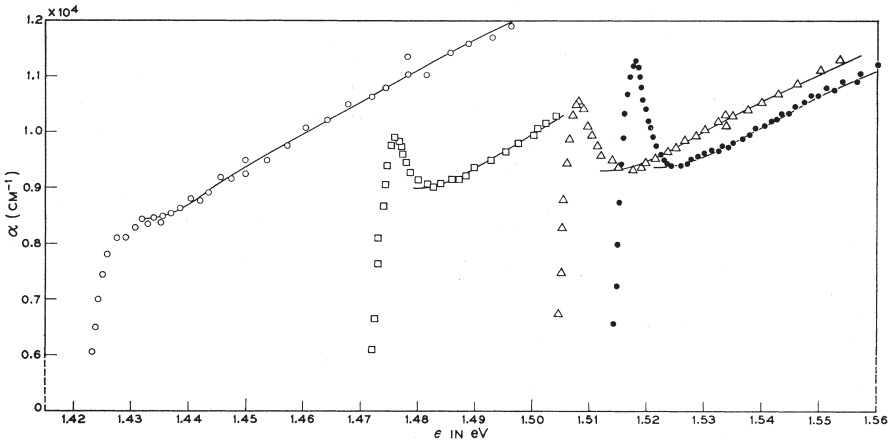


*Fig. 1.19* Experimental result for the exciton absorption in GaAs near its bandgap for different temperatures, as indicated by different symbols: ○ 294K, □ 186K, △ 90K, • 21K (from Ref. [71]).

thermore, it should be stressed that the decreased structure dimensionality increases the exciton binding energy. Thus, excitons are more stable in semiconductor nanostructures than in bulk. Therefore, exciton recombination is an important feature of low temperature PL in quantum structures. Knowing the exciton binding energy and the particles confinement energies, one can calculate the total exciton energy, which is equal to the PL energy.

Already in 1958, Lampert [72] showed that an electron (hole) bound to an exciton is stable and forms a so-called *charged exciton* or *trion*. When an electron is bound to the exciton, a negatively charged exciton or $X^-$ is obtained, whereas a hole bound to the exciton results in a positively charged exciton or $X^+$. Their bulk binding energy was calculated by Stébé *et al.* [73] and was found to be approximately 0.1 meV. The low binding energy found theoretically was consistent with the inability of the experimentalists to detect charged excitons in bulk semiconductors. With the advent of nanotechnology, the low trion binding energy was enhanced and it has become possible to fabricate semiconductor devices at a nanoscale, clearing the path for trion detection in quantum wells [74], wires [75] and dots [76]. Trions are not only interesting from a fundamental point of view. Knowledge of the associated PL energies is needed for a better understanding of the spectrum of a nanostructure, leading to successful application of quantum structures to quantum information technologies.

To conclude this section, it is instructive to point out that when studying excitons and trions in freestanding NWs, we will introduce the model of an infinitely long cylinder (see Fig. 1.20): along the z-axis, the charged particles in the wire are not confined, whereas a strong confinement is present along

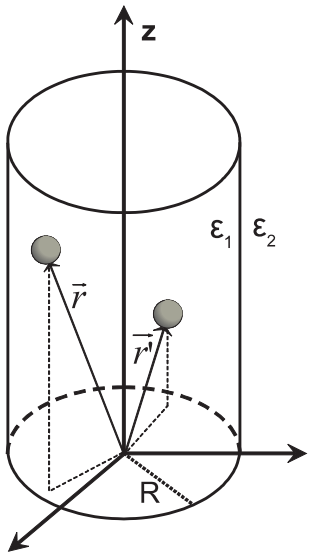


*Fig. 1.20* Model of a nanowire containing charged particles. In freestanding nanowires, the ratio between both dielectric constants ($\epsilon_1/\epsilon_1$) is typically of the order of 10.

the other two axes. The charged particles in the wire will interact with each other via the usual Coulomb forces, but because of the difference in dielectric constants in- ($\epsilon_1$) and outside ($\epsilon_2$) the wire, this Coulomb interaction will be distorted.

## 1.5 NUMERICAL TECHNIQUES

Once the Hamiltonian of a system is known, its eigenvalues and eigenvectors are in principle also known: the corresponding Schrödinger equations throughout this thesis are nothing more than time-independent partial differential equations (PDEs). However, obtaining a solution for them is never an easy task. In most cases - as is also the case in this thesis - analytical solutions are not possible and we are bound to turn to numerical techniques in order to solve the problem.

For numerically solving the partial differential equation for the exciton, we used the finite difference method. In this method, a finite difference scheme has to be constructed, which is obtained by approximating the derivatives by finite differences. This method was used for the solution of the exciton problem. For excitons, as will be explained explicitly in Chapter 2, a 1D PDE has to be solved. This can be done in the following way: let us consider a grid with $N$ points for the $x$-coordinate, so that $x_i = x_0 + (i-1)h$, where $h$

is the grid stepsize and $i = 1, 2, 3 \ldots N$. When replacing the derivatives with their finite difference counterparts as follows

$$\left.\frac{\partial^2 f}{\partial x^2}\right|_{x_i} = \frac{f_{i+1} - 2f_i + f_{i-1}}{h^2} \tag{1.6}$$

where $f_{i\pm1} = f(x_{i\pm1})$ and $f_i = f(x_i)$, one obtains a set of linear equations which needs to be solved. These linear equations can be written as a sparse matrix from which eigenvalues and eigenvectors are calculated.

T obtaine the solutions of the trion and shallow donor system, COMSOL *Multiphysics* [77] was used. This software package acts as a black box for the user, who implements the PDE, creates a mesh suitable for the problem, and finally the problem is solved. The underlying algorithm of COMSOL is based on the finite element method (FEM). The FEM originates from the principle of the action integral. In fact, basically all the differential equations of interest in physics can be derived by the calculus of variations from a corresponding action integral. There are several ways to arrive at the equation that needs to be solved, but in quantum mechanics, this can be found by minimizing this action integral which can be written as [78]

$$A = \int \mathrm{d}^3\mathbf{r} \left[ \frac{\hbar^2}{2m} \nabla\psi^*(\mathbf{r}) \cdot \nabla\psi(\mathbf{r}) + \psi^*(\mathbf{r})(V(\mathbf{r}) - E)\psi(\mathbf{r}) \right]. \tag{1.7}$$

By dividing an interval into $N$ smaller regions, or *elements*, the action integral can be written as a sum of $N$ terms. The solution, say $\psi$, can then be expressed as a linear combination of interpolating polynomials multiplied by a set of unknown coefficients. Minimization of this integral leads to a matrix eigenvalue problem which by solving gives the ground and excited states.

It is clear that, as the grid stepsize or element size approaches zero, the approximation becomes more and more accurate. It should be noted however, that taking the stepsize (element size) extremely small leads to larger matrices that have to be diagonalized. Therefore it is convenient to take a non-uniform grid, which allows to place many gridpoints (elements) in the region of interest (close to where the wave function undergoes most of the changes) and few gridpoints (elements) near the interval's boundaries, without increasing the size of the matrix too much. This concept of a non-uniform grid has been used throughout the whole thesis, and becomes particularly useful in higher dimensional systems (such as the trion), whose matrices would quickly result in extremely large ones if the grid is not constructed in an intelligent way. Also in the case of donors, where we took an extremely fine grid in the region of the donor site – which was required to model the $1/r$ potential – and a coarser grid elsewhere, the non-uniform grid turns out to be extremely handy and necessary to obtain correct energy levels.

## 1.6 ORGANIZATION OF THE THESIS

This thesis is organized as follows: In chapter two, I start by studying the bare exciton in a semiconductor nanowire without dielectric mismatch. I give explicit analytical expressions for the effective excitonic Coulomb potential which I use in further chapters. Furthermore, the effective mass approximation will be adopted to obtain the binding energy of the exciton numerically for arbitrary wire thicknesses. Also the energy of excited exciton states can be found and analytical expressions will be fitted to the numerical results. Finally, the influence of a magnetic field will be studied in detail.

The third chapter takes the dielectric mismatch into account, which results in an extra contribution to the previously calculated exciton potential. The extra contribution to the exciton potential will be studied in detail for a wide range of dielectric constants, enabling a general use of the obtained results. This contribution will also be fitted to an analytical expression to facilitate and speed up the process of binding energy calculation. The binding energy will be studied as function of the mismatch and the wire radius, which can reveal the strong effect of mismatch effects.

The fourth chapter is devoted to the study of trions. Since I investigated all possible interaction between particles in the previous chapters, it is straightforward to obtain the effective trion potential, which allows an immediate calculation of the trion binding energy. Contourplots as function of the wire's dielectric constant and the electron-hole mass ratio can be made for the exciton binding energy, a convenient tool which immediately allows a quick estimate of the trion binding energy for a very large set of materials. Furthermore, I also study the trion wave functions and discus both correlation functions and conditional probabilities of the trions. These results show the correlated arrangement of the particles in the wire. To conclude, I will calculate the binding energy as a function of the wire radius and study its $R$-dependence.

Finally, the effect of an impurity near a metallic gate is treated in chapter five. I calculate the energy levels of the impurity as a function of the donor position and compare them with the bulk values to demonstrate the effect of the metallic interface on the energy levels that may also carry source-to-drain tunneling currents in nanoscale transistors. In view of potential quantum computing applications, I also study the effect of an electric field moving the electron away from the donor site to the interface. An acceptable degree of lateral localization of the electron at the interface is necessary, therefore I will investigate what electric fields are allowed enabling one to switch between the donor site and the metallic interface. Or in other words: it is crucial that the energy spectrum is not dominated by the electric field strength but by the characteristic of the sample, such as the donor position.

# 2

# Excitons without dielectric mismatch

## 2.1 INTRODUCTION

In the previous chapter we showed how semiconductor nanowires with a small diameter can nowadays be grown to form free-standing nanowires [28]. From a theoretical point of view such semiconductor nanowire structures enable us to understand the role of dimensionality on physical properties. Furthermore, they provide a great potential for the applications mentioned in the previous chapter, for instance transistors [2, 3, 4, 5], diodes [6, 7], memory elements [8], lasers [9, 10, 11], chemical and biological sensors [12, 13], etc.

These nanowires have a large aspect ratio and can be considered one-dimensional structures. They have a length and a diameter roughly in the micrometer resp. nanometer range. Electrons and holes are strongly confined in two directions and there is no confinement in the direction of the axis of the wire. In this chapter we will investigate the exciton binding energy and its lowest excited states. Excitons determine the basis of optical properties reflecting the intrinsic nature of low-dimensional systems. As a first step we investigate the potential and energy of the electron-hole pair. Because our aim is to present numerically 'exact' results we will limit ourselves for the moment, to the *model* system in which the difference in dielectric constant of the nanowire material and its surrounding, i.e. the *dielectric mismatch*, is neglected. Only in this special case we are able to present analytical results.

In previous work [79], a similar model system was studied, but only the ground exciton state was obtained and no systematic study was presented of the dependence on wire radius, mass of the carriers, magnetic field and of the

excited states. Also impurity states – both with and without a magnetic field parallel to the wire axis – were considered in previous papers [80, 81], with the charged impurity fixed to the cylinder axis and with averaging performed only over the electronic motion. The effective potential for the ground state configuration was obtained before [82] – the calculations involved the numerical evaluation of multi-dimensional integrals – and agrees with our results. One of the aims of the present work is to give explicit analytical expressions for the effective Coulomb potential that are fitted to the numerical results and are more tractable for future calculations of e.g. the energy levels of exciton complexes. Furthermore, the binding energy of the exciton is calculated numerically for a broad range of wire thicknesses, while the results of Ref. [79] were limited to thin wires. Also the energy of excited exciton states are given and analytical expressions are fitted to the numerical results. Finally, the addition of a magnetic field is another extension which hasn't been studied in detail before. The effective potential was calculated before for embedded rectangular wires [83] for magnetic fields perpendicular and parallel to the wire axis. The focus of Ref. [83] is not on the effective potential, but on the calculation of the exciton energy and a comparison with experiment. In Ref. [84] analytical expressions for parabolic confined wires were obtained, which have been fitted accurately to our results in the high magnetic field limit. Note that our calculations are very general, since they apply to arbitrary materials provided they can be described within the framework of the effective mass theory.

This chapter is organized as follows. In Sect. 2.2 we consider the single particle states of the electron and the hole. In Sect. 2.3 we define the exciton Hamiltonian to calculate the effective potential of the exciton in Sect. 2.4, using the adiabatic approximation. The numerical results for the effective potential as function of the interparticle distance are fitted to simple analytical expressions. The exciton energy is calculated numerically and semi-analytically in Sect. 2.5. The influence of a magnetic field will be investigated in Sect. 2.6 and our conclusions are presented in Sect. 2.7.

## 2.2 SINGLE PARTICLE STATES

For completeness we first consider the eigenfunctions and corresponding eigenvalues of a single particle in a circular [85] potential well with radius $R$. Adopting the effective mass approximation we write the Schrödinger equation as follows:

$$-\frac{\hbar^2}{2m}\nabla^2\psi(\mathbf{r}) + V(\mathbf{r})\psi(\mathbf{r}) = E\psi(\mathbf{r}), \tag{2.1}$$

where we approximate the confinement potential of the wire by a hard wall potential

$$V(\mathbf{r}) = \begin{cases} 0 & \text{if } \rho \leq R \\ \infty & \text{if } \rho > R \end{cases}, \tag{2.2}$$

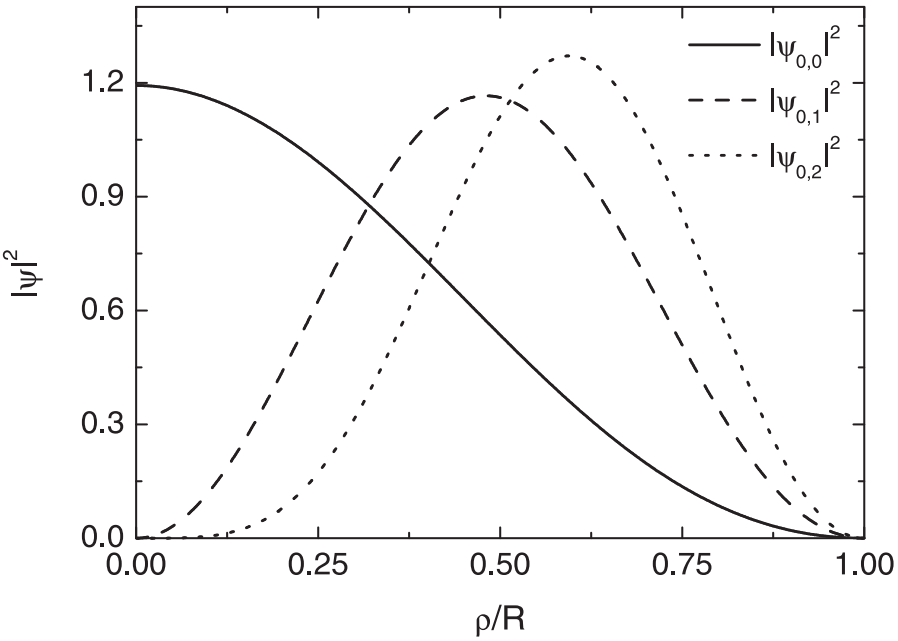


*Fig. 2.1* Density for the electron and hole in the nanowire for the lowest three single-particle states.

where $\rho = \sqrt{x^2 + y^2}$. For the free-standing wire the potential height is given by the work function which is typically a few eV and therefore very large compared to typical confinement energies. The wire is oriented along the $z-$axis. Since the motion in the $z-$direction (free particle in that direction) is decoupled from the motion in the $(x, y)-$plane and because of circular symmetry, we have $\psi(\rho, \theta, z) = F(\rho)e^{-il\theta}e^{ik_z z}$, where $\theta$ is the polar angle. The Schrödinger equation is then reduced to the one dimensional (1D) equation

$$\rho^2 \frac{\mathrm{d}^2 F(\rho)}{\mathrm{d}\rho^2} + \rho \frac{\mathrm{d}F(\rho)}{\mathrm{d}\rho} + ((k^2 - k_z^2)\rho^2 - l^2)F(\rho) = 0, \tag{2.3}$$

with $k^2 = 2mE/\hbar^2$. The solutions to this equation are the well known Bessel functions and taking hard wall boundary conditions into account, one gets for the single particle wave functions

$$\psi_{n,l,k_z}(\rho, \theta, z) \quad = \quad C_{n,l} e^{-il\theta} J_l \left( \frac{\beta_{n,l}}{R} \rho \right) e^{ik_z z}, \tag{2.4}$$

and the corresponding eigenenergies

$$E_{n,l,k_z} \quad = \quad \frac{\hbar^2 \beta_{n,l}^2}{2mR^2} + \frac{\hbar^2 k_z^2}{2m}, \tag{2.5}$$

where $C_{n,l}$ is the normalisation constant and $\beta_{n,l}$ is the $n^{th}$ order zero of the Bessel function $J_l(x)$. The zeros of the Bessel functions are known and can be found in the literature [86]: $\beta_{0,0} = 2.4048, \beta_{0,1} = 3.8317, \beta_{0,2} = 5.1356, \beta_{1,0} = 5.5201, \beta_{1,2} = 8.4172, \beta_{2,2} = 11.6198, \ldots$. Notice that the first excited state is $|0, 1, k_z\rangle$ and the second one $|0, 2, k_z\rangle$. The lowest three radial densities $|\psi_{n,l}|^2$ are plotted in Fig. 2.1.

## 2.3 HAMILTONIAN

The appropriate Hamiltonian for an exciton in the effective mass approximation is given by

$$\begin{aligned} H &= -\frac{\hbar^2}{2m_e}\nabla_e^2 + V_e(x_e, y_e) - \frac{\hbar^2}{2m_h}\nabla_h^2 + V_h(x_h, y_h) \\ &\quad + V_C\left(\mathbf{r}_e - \mathbf{r}_h\right), \end{aligned} \tag{2.6}$$

where $m_e$ ($m_h$) is the effective mass of the electron (hole), $V_e$ ($V_h$) is the confinement potential of the electron (hole) and

$$V_C\left(\mathbf{r_e} - \mathbf{r_h}\right) = -\frac{1}{4\pi\epsilon}\frac{e^2}{\sqrt{(x_e - x_h)^2 + (y_e - y_h)^2 + (z_e - z_h)^2}}, \tag{2.7}$$

is the Coulomb interaction potential between the electron and the hole. In this case, it is convenient to separate the motion of the two particles into that of the center of mass of the system and the relative motion, thereby introducing the quantities: $Z = (m_e z_e + m_h z_h)/(m_e + m_h), z = z_e - z_h, M = m_e + m_h, \mu = (m_e m_h)/(m_e + m_h)$. Now the Hamiltonian can be rewritten as

$$\begin{aligned} H = &-\frac{\hbar^2}{2m_e}\left(\frac{\partial^2}{\partial x^2} + \frac{\partial^2}{\partial y^2}\right) - \frac{\hbar^2}{2m_h}\left(\frac{\partial^2}{\partial x^2} + \frac{\partial^2}{\partial y^2}\right) \\ &+ V_e(x_e, y_e) + V_h(x_h, y_h) \\ &- \frac{\hbar^2}{2M}\frac{\partial^2}{\partial Z^2} - \frac{\hbar^2}{2\mu}\frac{\partial^2}{\partial z^2} - \frac{1}{4\pi\epsilon}\frac{e^2}{\sqrt{(x_e - x_h)^2 + (y_e - y_h)^2 + z^2}}. \end{aligned} \tag{2.8}$$

In the case of strong lateral confinement, the exciton motion along the wire is decoupled form the lateral motion of the particles and we may factorize the wave function as follows

$$\Psi(x_e, y_e, x_h, y_h, z, Z) = e^{iKZ}\phi(z)\psi(x_e, y_e)\psi(x_h, y_h). \tag{2.9}$$

Because the Coulomb energy in the considered case is much weaker than the single particle confinement energy, we adopt the adiabatic approximation, thereby taking $\psi(x, y)$ as the above obtained single particle states. Multiplying Eq. (2.8) with $\psi^*(x_e, y_e)\psi^*(x_h, y_h)$ from the left and with $\psi(x_e, y_e)\psi(x_h, y_h)$ from the right, integrating over the lateral coordinates we reduce the original

6D Schrödinger equation for the exciton problem to a 1D effective Schrödinger equation for the relative exciton coordinate

$$\left(E_e + E_h + \frac{\hbar^2 K^2}{2M} - \frac{\hbar^2}{2\mu}\frac{\partial^2}{\partial z^2} + V_{\text{eff}}(z)\right)\phi(z) = E_{\text{tot}}\phi(z), \tag{2.10}$$

where $E_e$ ($E_h$) are the single-electron (hole) energies, and the effective exciton potential, $V_{\text{eff}}$, is given by

$$V_{\text{eff}}^{n,l}(z) = -\frac{e^2}{4\pi\epsilon}\int \mathrm{d}x_e \mathrm{d}x_h \mathrm{d}y_e \mathrm{d}y_h \frac{|\psi_{n,l,k_z}(x_e,y_e)|^2\,|\psi_{n,l,k_z}(x_h,y_h)|^2}{\sqrt{(x_e-x_h)^2+(y_e-y_h)^2+z^2}}. \tag{2.11}$$

Introducing dimensionless variables (i.e. length expressed in units of $R$) and $\alpha = a_B^*/2R$ with $a_B^* = 4\pi\epsilon\hbar^2/\mu e^2$ the effective Bohr radius, we finally get

$$\left(-\alpha\frac{\partial^2}{\partial z^2} + \tilde{V}_{\text{eff}}(z)\right)\phi(z) = \tilde{E}_C\phi(z), \tag{2.12}$$

where $z$ is from now on given in units of $R$, $\tilde{V} = V/E_0$, $\tilde{E_C} = E_C/E_0$, $E_0 = e^2/4\pi\epsilon R$ and $E_C = E_{\text{tot}} - E_e - E_h - \hbar^2K^2/2M$.

## 2.4 EFFECTIVE POTENTIAL

To study the bound states of the exciton, we first have to evaluate the exciton potential of Eq. (2.11), taking into account the $1/r$ singularity for $r \to 0$, where $r$ represents the distance between electron and hole.

The method we used to get rid of this problem, the logarithmically weighted method, is explained in Appendix A. The result of the calculations can be found in Fig. 2.2, where we show the effective Coulomb potential when the electron and the hole are in the ground state, i.e. $\psi \to \psi_{0,0}$, ($V^{0,0}$) and in both the first and second excited state, i.e. $\psi \to \psi_{0,1}$ ($V^{0,1}$) and $\psi \to \psi_{0,2}$ ($V^{0,2}$) respectively (the corresponding single particle densities are shown in Fig. 2.1). Notice how all effective potentials in Fig. 2.2 show the $-1/z$ behaviour for $z \to \infty$ and that the effective potential is finite for $z = 0$.

### 2.4.1 Approximate analytical expressions

Since the calculation of the effective Coulomb potential requires a considerable amount of computing time, it is highly desirable to have an analytical expression for it. Let us first consider the small $z$ behaviour of the effective potential:

$$\tilde{V}_{\text{eff}}(z) = a + bz + cz^2, \tag{2.13}$$

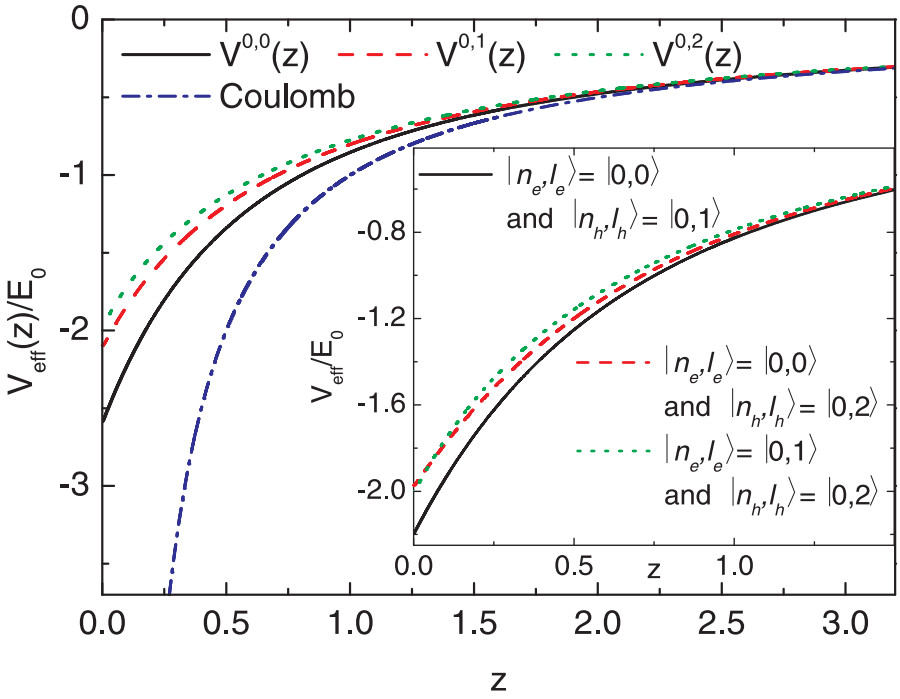


*Fig. 2.2* Effective exciton interaction potential as a function of the electron-hole separation $z$ for three different states of the electron and hole (Full curve: $n_e = l_e = 0$ and $n_h = l_h = 0$ for the hole; dashed curve: $l_e = l_h = 1$ and $n_e = n_h = 0$; dotted curve: $l_e = l_h = 2$ and $n_e = n_h = 0$). The regular Coulomb potential, $1/z$, is also plotted (dashed-dotted) for comparison. Inset: The effective potential for different sets of quantum numbers for the electron and hole.

where $\tilde{V}_{\rm eff}(z) = V_{\rm eff}(z)/E_0$ and $z$ is in units of $R$. The coefficients are given by

$$a = \tilde{V}_{\rm eff}(z=0) = -2.5961, \tag{2.14}$$

$$b = \left.\frac{{\rm d}\tilde{V}_{\rm eff}(z)}{{\rm d}z}\right|_{z=0} = 4.1967, \tag{2.15}$$

$$c = \left.\frac{1}{2}\,\frac{{\rm d}^2\tilde{V}_{\rm eff}(z)}{{\rm d}z^2}\right|_{z=0} = -5.6140, \tag{2.16}$$

for the single particle ground state. In a similar way, we get $a = -2.1126$ ($a = -1.9774$), $b = 3.1031$ ($b = 3.0608$) and $c = -4.5503$ ($c = -5.4277$) for the first (second) excited state. This polynomial expression, Eq. (2.13), agrees within 1% with the numerical result for $z/R < 0.14$.

Next we look for an analytical expression that covers the whole range of $z$-values. Therefore, we have approximated the full effective potential by Padé approximants, the first order one being

$$\tilde{V}_{\text{eff}}(z) = \frac{P_0(z)}{P_1(z)} = \frac{v}{w + |z|}, \tag{2.17}$$

where $P_i(z)$ is a polynomial of $i-$th order. This formula corresponds to Eq. (2.8a) of Ref. [79]. If we take into account that $\tilde{V}_{\text{eff}}(0) = v/w$ and remember that for $z \to \infty$ the effective potential behaves as a normal Coulomb potential $(-1/z)$, we can conclude that $v = -1$ and calculate that $w = 0.3852$ (ground state), $w = 0.4734$ (first excited state) and $w = 0.5057$ (second excited state).

This Padé approximation and the numerical result are compared in Fig. 2.3(a) for the ground state and Fig. 2.3(b) for the first and second excited state. To improve this result we consider the next Padé approximation:

$$\tilde{V}_{\text{eff}}(z) = \frac{P_1(z)}{P_2(z)} = \frac{\gamma\,|z| + \delta}{z^2 + \eta\,|z| + \beta}. \tag{2.18}$$

The condition $\tilde{V}_{\text{eff}}(z) \overset{z\to\infty}{\longrightarrow} -1/z$ implies that $\gamma = -1$ and $\delta/\beta = \tilde{V}_{\text{eff}}(z = 0)$, which leaves us with two fitting parameters. After fitting the data to the expression in Eq. (2.18), we find $\eta = 1.1288 \pm 0.0029, \beta = 0.4705 \pm 0.0015, \delta = -1.2215 \pm 0.0039$ for the electron and hole in the ground state, $\eta = 1.728 \pm 0.017, \beta = 0.899 \pm 0.011, \delta = 1.900 \pm 0.023$ for the electron and hole in the first excited state and $\eta = 2.749 \pm 0.061, \beta = 1.559 \pm 0.039, \delta = -1.9774\beta = 3.083 \pm 0.077$ for the electron and hole in the second excited state. The second order Padé approximation is also shown in Fig. 2.3 and we obtain an excellent fit (i.e. within 1.5%) for all states. If the confinement potential for the electron and hole is a parabolic potential, i.e. $V(x, y) = m\omega_0^2(x^2 + y^2)$ instead of a circular hard wall confinement, it is possible to perform all integrals in Eq. (2.11) analytically. The analytical result for the effective potential was obtained in Ref. [84] and reads

$$\tilde{V}_{\text{eff}}(z) = -\left(\frac{\pi}{2}\right)^{1/2} \frac{1}{l_0/R} \left[1 - \text{erf}\left(\frac{|z|}{\sqrt{2}l_0/R}\right)\right] e^{z^2/2(l_0/R)^2} \tag{2.19}$$

with the oscillator length $l_0 = (\hbar/m\omega_0)^{1/2}$. It is remarkable that this potential approaches our effective exciton potential very closely if we define $l_0$ to be

$$l_0/R = -\frac{1}{\tilde{V}_{\text{eff}}(0)} \left(\frac{\pi}{2}\right)^{1/2}. \tag{2.20}$$

i.e. the expression for the oscillator length extracted from Eq. (2.19) by putting $z = 0$. It is possible now to calculate numerically $l_0/R$ for the different effective potentials: $l_0/R = 0.4828$ (ground state), $l_0/R = 0.5933$ (first excited state)

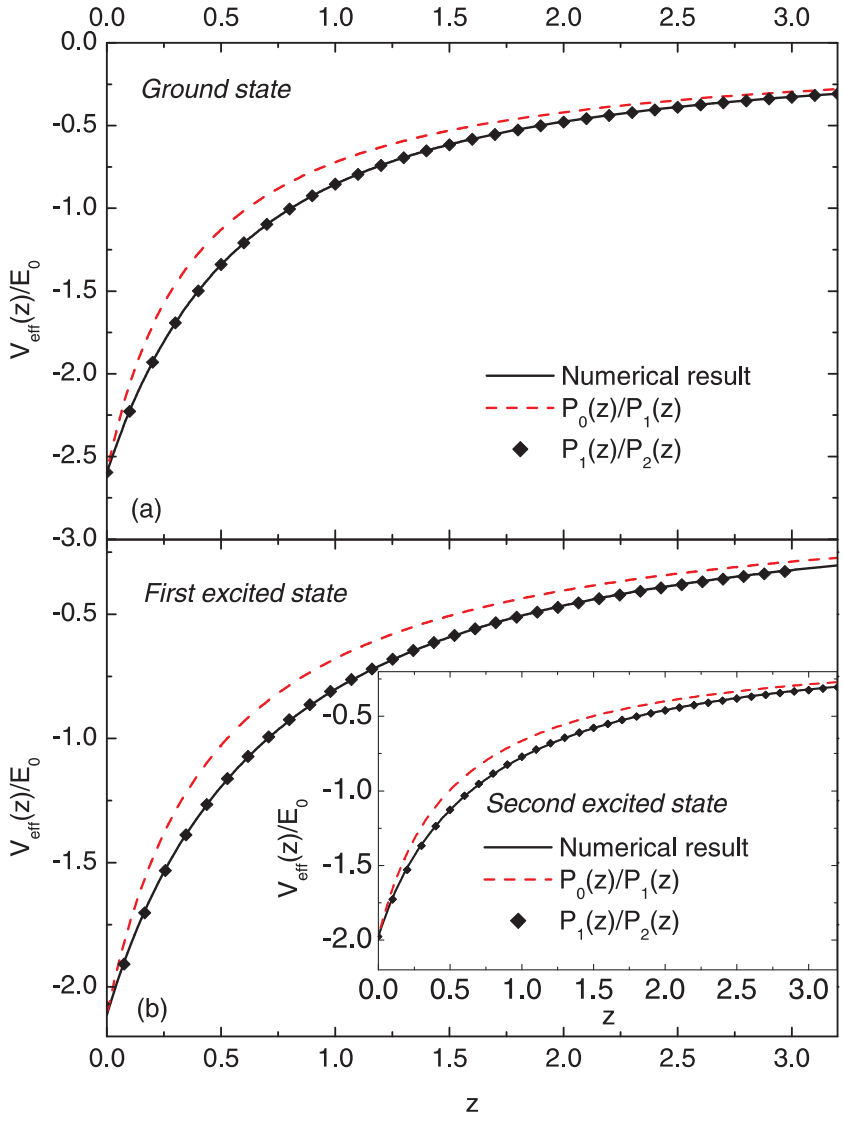


*Fig. 2.3* Plot of the numerical data and the two Padé approximations, $P_0(z)/P_1(z)$ and $P_1(z)/P_2(z)$, for (a) the ground state and (b) the first and second (inset) excited state.

and $l_0/R = 0.6338$ (second excited state). Using these results in Eq. (2.19), we get an expression for the effective exciton potential as function of the interparticle distance. The analytical approximation (2.19) and the numerical data can be seen in Fig. 2.4 and show a good agreement for ground state and

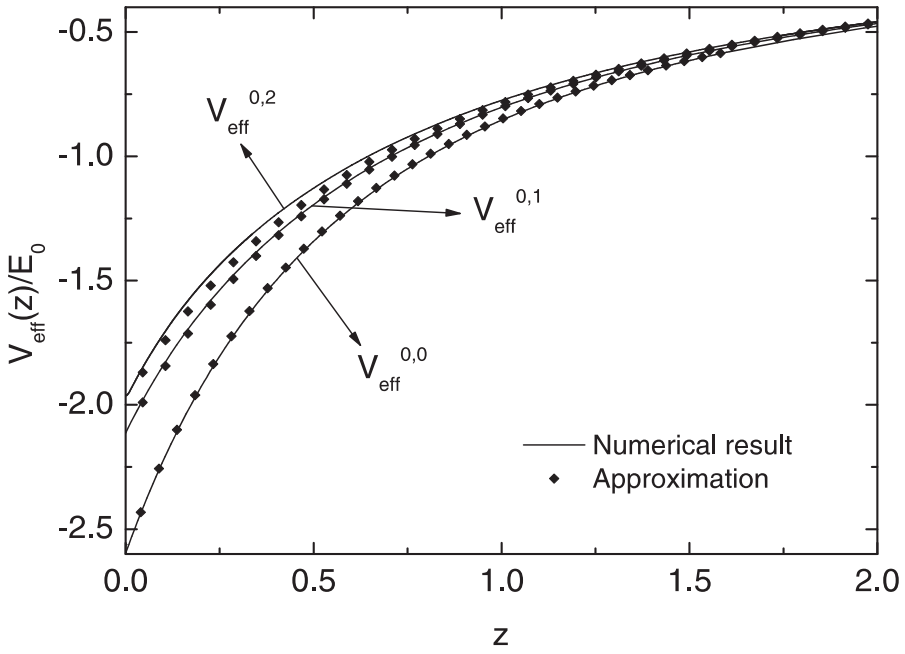


*Fig. 2.4* Comparison between the numerical evaluation of the effective electron-hole potential and the approximate one using the wave function of a harmonic oscillator for three different sets of quantum numbers of electron and hole.

first excited state (fit within 0.7% of the data), while for the second excited state the approximated result is still reasonable (fits within 3.2% of the data).

## 2.5 EXCITON ENERGY

### 2.5.1 Numerical calculations

When a single exciton is created, its energy is generally given by $E = E_g + E_e + E_h + E_C$, where $E_g$ denotes the energy band gap, $E_{e(h)}$ is the single electron (hole) energy and $E_C$ is the (negative) energy of the Coulomb interaction between electron and hole. For a given material, we only have to calculate $E_C$, all other contributions to the exciton energy being known. Therefore, the 1D Schrödinger equation [Eq. (2.12)] was solved on a non-uniform grid using the finite difference technique (see Appendix B for the finite difference scheme). Fig. 2.5 shows the energy of the Coulomb interaction of the three lowest exciton energy levels as a function of the dimensionless parameter $\alpha = a_B^*/2R$ for two cases of the effective potential.

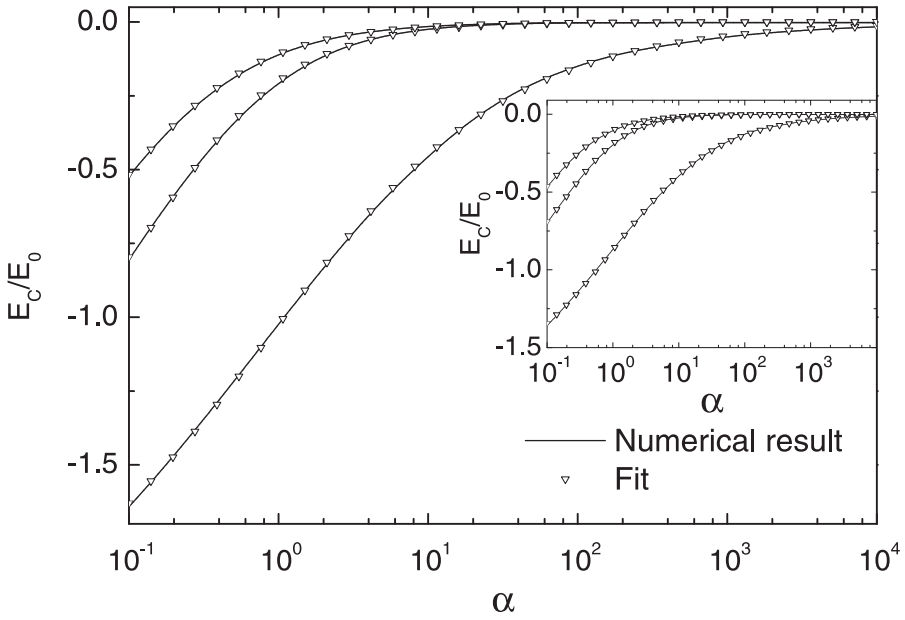


*Fig. 2.5* Binding energy as a function of the parameter $\alpha = a_B^*/2R$. The solid curves are calculated by using the effective potential $V^{0,0}$ (electron and hole in the ground state). The symbols represent the fit which is given by Eq. (2.21). Inset: The same, but now for the effective potential $V^{0,1}$ (electron and hole in the first excited state).

The binding energy $E_C$ can also be fitted to an analytical expression now. Values of $\alpha < 0.1$ are not realistic, since this would correspond to a large radius and a strong confinement approach would no longer be valid. Therefore, the following fit is suggested for $\alpha$ values exceeding 0.1,

$$\tilde{E}_C = \frac{\xi}{1 + b\alpha^\tau}. \tag{2.21}$$

For the ground state configuration of the electron and hole, we find that $\xi = -2.145 \pm 0.020$, $b = 1.093 \pm 0.022$, $\tau = 0.5385 \pm 0.0040$, and for the first (second) excited states of the exciton binding energy we find $\xi = -1.287 \pm 0.031$, $b = 5.42 \pm 0.16$ and $\tau = 0.945 \pm 0.013$ ($\xi = -1.211 \pm 0.016$, $b = 10.23 \pm 0.14$ and $\tau = 0.8830 \pm 0.0034$) (see Fig. 2.5 for the fits). Similarly, for the configuration where electron and hole are in the first excited state, we find that $\xi = -1.714 \pm 0.015$, $b = 0.967 \pm 0.020$ and $\tau = 0.5449 \pm 0.0042$ (ground state), $\xi = -1.0525 \pm 0.028$, $b = 4.56 \pm 0.16$, $\tau = 0.940 \pm 0.016$ (first excited state) and $\xi = -0.965 \pm 0.016$, $b = 8.47 \pm 0.15$, $\tau = 0.8944 \pm 0.0051$ (second excited state).

From Eq. (2.12) it is clear that for small $\alpha-$values, there is a relatively smaller contribution of the kinetic energy term $\partial^2\psi/\partial z^2$. As $\alpha$ increases, the energy of the particle will also increase, because of an increase in the

contribution from the kinetic energy term. For large values of $\alpha$ the energy levels accumulate around the $\tilde{E}_C = 0$ level. In fact, because of the $1/z$ behaviour of the exciton potential for large $z$, the integral $\int V(z)^{1/2}\mathrm{d}z$ diverges and according to Ref. [87] there will be an infinite number of bound states.

### 2.5.2 Comparison with analytical results

In this section we present an analytical solution of the 1D Schrödinger equation Eq. (2.12). Similar calculations were done earlier by Loudon [88], who solved the problem of the 1D hydrogen atom (i.e. the ideal limit of the 1D electron-hole system: infinitesimal wire cross-section and hard wall confinement) analytically. To avoid the divergence of the original potential at $z = 0$ Loudon used different models, e.g. hard wall conditions at $z = 0$, i.e. $\phi(z = 0) = 0$. The 1D Schrödinger equation, Eq. (2.12), has in general to be solved numerically. We used the finite difference technique. In the special case in which the effective potential is approximated by the first Padé approximant, Eq. (2.17), it is possible to obtain an analytical expression for the wave function. After introducing the new variable $y = 2\sqrt{-\tilde{E}_C/\alpha}(z+w)$, we can rewrite Eq. (2.12) as the Whittaker equation:

$$\frac{\partial^2\phi(y)}{\partial y^2} + \left(-\frac{1}{4} + \frac{1}{2y\alpha\sqrt{-\tilde{E}_C/\alpha}}\right)\frac{\partial\phi(y)}{\partial y} = 0. \tag{2.22}$$

The wave functions are then given in terms of the Whittaker function

$$\phi(y) = Aye^{-y/2}U(1-\kappa;2;y), \tag{2.23}$$

where $A$ is a normalisation constant and $\kappa = -v/2\alpha\sqrt{-\tilde{E}_C/\alpha}$. The energy is then obtained by solving the following equations:

$$\begin{aligned} \left.\frac{d\phi(y)}{dy}\right|_{y=2w\sqrt{-\tilde{E}_C/\alpha}} &= 0 \qquad \text{(even states)}, \\ \phi(y = 2w\sqrt{-\tilde{E}_C/\alpha}) &= 0 \qquad \text{(odd states)}. \end{aligned} \tag{2.24}$$

We now obtain the energy of the Coulomb interaction semi-analytically (by solving the transcendental equation) and we compare it in Fig. 2.6 with the numerically calculated energy. Notice that for large $\alpha$ both energies are close to each other. But for small $\alpha$-values (which corresponds to large $R$) there is a underestimation of the exciton energy up to 15 %. This is not surprising, since the first Padé approximation leads to a rather poor fit to the effective potential (see Fig. 2.3(a)). Nevertheless analytical calculations are useful because they allow for an estimation of the energy without having to

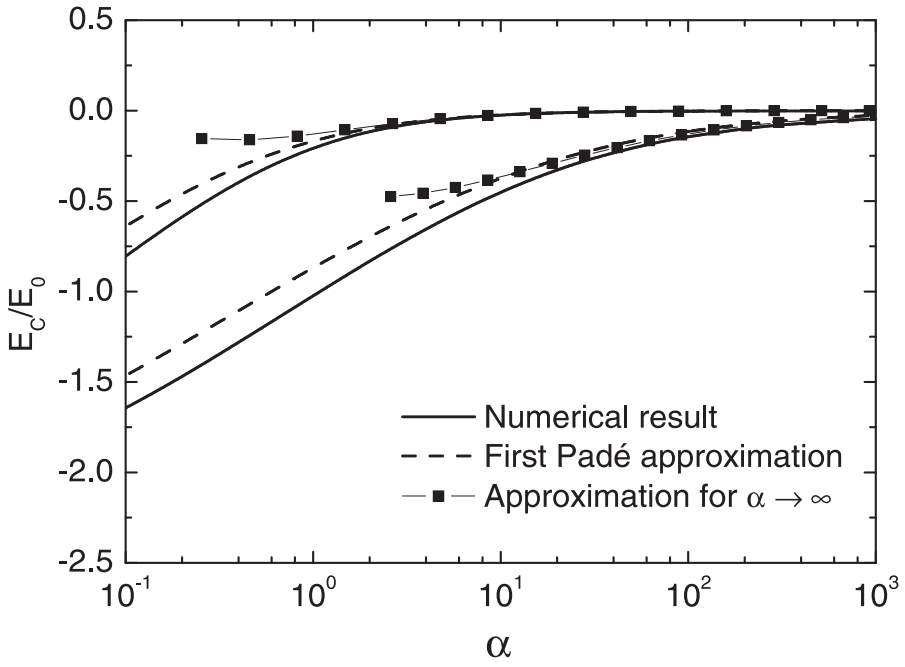


*Fig. 2.6* Ground state (lower curves) and first excited state (upper curves) energy of the exciton when 1) using the first Padé approximation for the electron-hole interaction potential and 2) the numerical result for the electron and hole in the ground state. The curve with symbols is the asymptotic behaviour, i.e. Eq. (2.25).

solve the differential equation (2.12) numerically. Furthermore it has to be noticed that, in the case of large $\alpha$ (which corresponds to small radii $R$), a simple analytical expression [79] for $\tilde{E}_C$ can be found:

$$\tilde{E}_C = -1/4\alpha\nu^2 \tag{2.25}$$

where

$$\nu = \nu_m \begin{cases} \nu_m = m + \frac{w}{\alpha} & \text{(odd states)} \\ \nu_m = m - \frac{1}{\ln(w/m\alpha)} & \text{(even states)} \end{cases} \tag{2.26}$$

for $m = 1, 2, 3, \ldots$ determine the bound states of the exciton. This asymptotic result is shown in Fig. 2.6 by the square symbols and is clearly valid only for large $\alpha$. Note that in the limit of a Coulomb interaction potential the excited states are twofold degenerate. The lowest bound state satisfies the special relation

$$\ln\left(\frac{w}{\nu_0\alpha}\right) + \frac{1}{2\nu_0} = 0. \tag{2.27}$$

This approximation is also shown in Fig. 2.6 (square symbols).

## 2.6 MAGNETIC FIELD DEPENDENCE

### 2.6.1 Single-particle properties

When a magnetic field, directed along the wire, is applied, the single-particle Hamiltonian for an electron ($q = -|e|$) or hole ($q = |e|$) can be written as

$$H = \frac{1}{2m}\left(-i\hbar\frac{\partial}{\partial \mathbf{r}} - q\mathbf{A}\right)^2 + V(\mathbf{r}), \tag{2.28}$$

where $m = m_e = m_h$ is the effective mass and $V(\mathbf{r})$ is again the confinement potential of the wire. Due to the symmetry of the problem we may benefit from the symmetric gauge $\mathbf{A} = \frac{1}{2}B\rho\mathbf{e}_\theta$ for the vector potential. For the same reason, the wave function $\psi(\rho,\theta)$ is separable, and can be written as $\psi(\rho,\theta) = R(\rho)e^{-il\theta}$, where the $z$-dependence has been omitted for the sake of simplicity. The Schrödinger equation now reads

$$\begin{aligned}&\left(\frac{\partial^2}{\partial\rho^2} + \frac{1}{\rho}\frac{\partial}{\partial\rho} - \frac{l^2}{\rho^2}\right)R + \\ &\left(-\frac{m\omega_c}{\hbar}\mathrm{sgn}(q)l - \left(\frac{m\omega_c}{2\hbar}\right)^2\rho^2 + \frac{2mE}{\hbar^2}\right)R = 0,\end{aligned} \tag{2.29}$$

where $\omega_c = |e|B/m$ is the cyclotron frequency. Introducing the following parameters, $k^{*^2} = -\mathrm{sgn}(q)lm\omega_c/\hbar + 2mE/\hbar^2$ and $1/l_B^2 = m\omega_c/2\hbar$, and by putting $R(\rho) = \rho^{|l|}\exp(-\rho^2/2l_B^2)f(\rho)$, one gets

$$t\frac{\mathrm{d}^2 f}{\mathrm{d}t^2} + ((|l|+1) - t)\frac{\mathrm{d}f}{\mathrm{d}t} - \left(\frac{1}{2}(|l|+1) - \frac{l_B^2 k^{*^2}}{4}\right)f = 0, \tag{2.30}$$

where the new variable $t$ is given by $t = \rho^2/l_B^2$. The solution is the confluent hypergeometric function [89].

$$\psi_{n,l}(\rho,\theta) \;=\; C_{n,l}e^{-il\theta}\rho^{|l|}e^{-\frac{\rho^2}{2l_B^2}}\;{}_1F_1\left(-a_{n,l};|l|+1;\frac{\rho^2}{l_B^2}\right), \tag{2.31}$$

where $C_{n,l}$ is a normalisation constant and

$$-a_{n,l} = \frac{1}{2}(|l|+1) - \frac{l_B^2 k^{*^2}}{4}, \tag{2.32}$$

is a constant which is obtained by imposing the hard wall boundary conditions, $\psi_{n,l}(R,\theta) = 0$. The single particle spectrum then becomes

$$E_{n,l} = \hbar\omega_c\left(a_{nl} + \frac{1+|l|+\mathrm{sgn}(q)l}{2}\right). \tag{2.33}$$

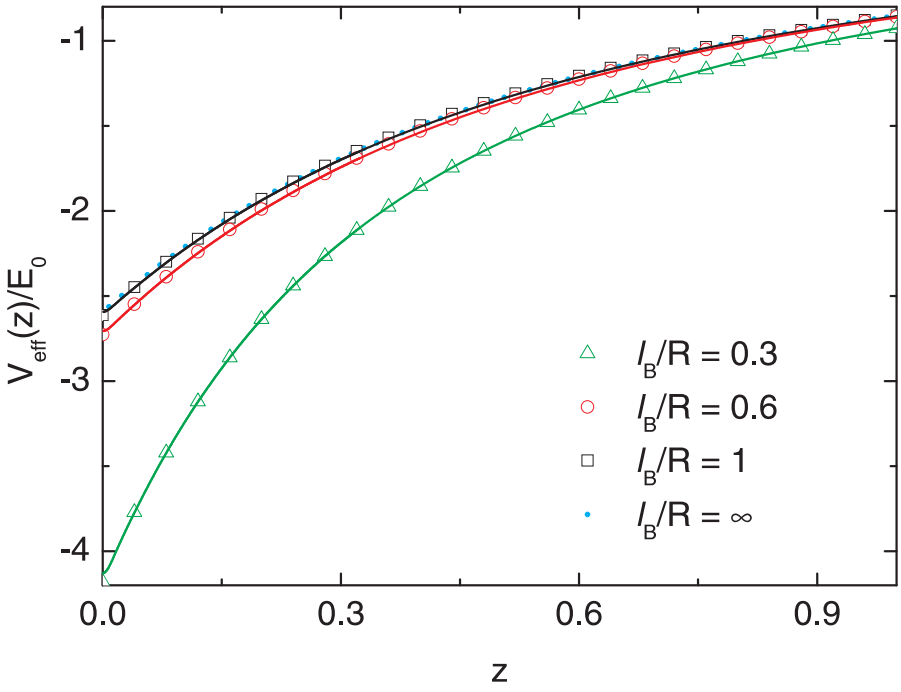


*Fig. 2.7* Effective exciton potential for different values of the magnetic field (full lines) in which the electron and hole are in the ground state. The approximation (open symbols) of Eq. (2.19) can be used again to fit the calculated effective potential. For comparison, the effective potential for the system without magnetic field was also drawn ($l_B/R = \infty$, dotted line). Note that for this figure, the electron and hole were in the ground state.

### 2.6.2 Effective exciton potential

The total Hamiltonian is now given by

$$\begin{aligned} H_{tot} &= -\frac{1}{2m_e}\left(\mathbf{p}_{x_e,y_e} + |e|\,\mathbf{A}\right)^2 - \frac{1}{2m_h}\left(\mathbf{p}_{x_h,y_h} - |e|\,\mathbf{A}\right)^2 \\ &\quad + V_e(x_e,y_e) + V_h(x_h,y_h) - \frac{\hbar^2}{2m_e}\frac{\partial^2}{\partial z_e^2} - \frac{\hbar^2}{2m_h}\frac{\partial^2}{\partial z_h^2} \\ &\quad - \frac{1}{4\pi\epsilon}\frac{e^2}{\sqrt{(x_e-x_h)^2+(y_e-y_h)^2+z^2}} \end{aligned} \tag{2.34}$$

Again, we can reduce this equation to a 1D effective Schrödinger equation similarly as for the $B = 0$ case by: i) separating the motion of the two particles into the center of mass relative coordinates, ii) by using the adiabatic approximation for the exciton wave function, and iii) by introducing the same dimensionless quantities as in Sect. 2.3. This leads us to the equivalent of

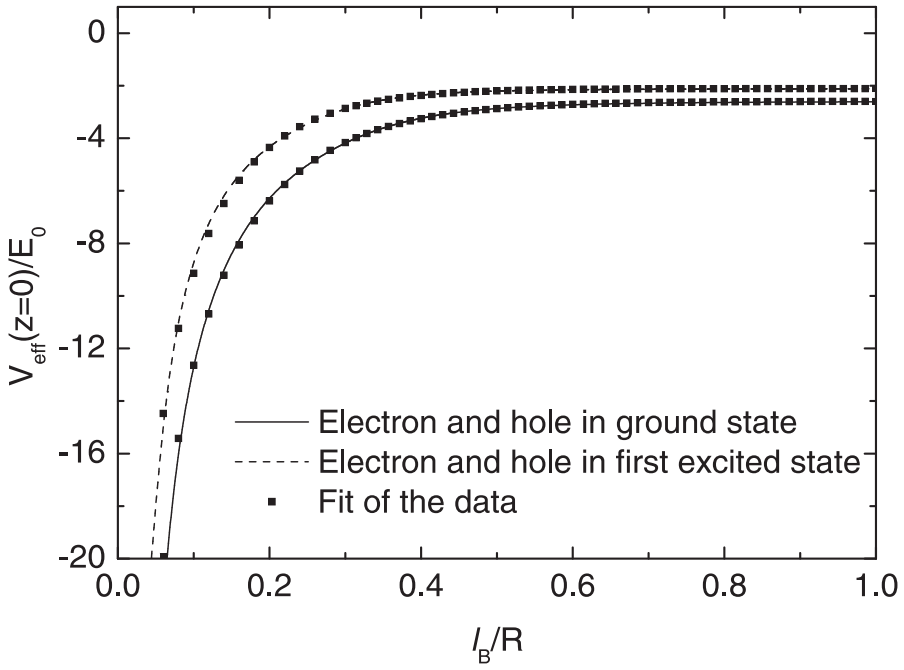


*Fig. 2.8* Effective exciton potential at $z = 0$ as function of the magnetic length $l_B$ (the magnetic field). The fit is to Eq. (2.37) and Eq. (2.39)

Eq. (2.12), where the single particle energies are now given by Eq. (2.33) and the averaging of the effective potential has to be performed with the Kummer functions (Eq. (2.31)) (instead of Bessel functions). Note that the confluent hypergeometric function ${}_1F_1$ is equivalent to the Kummer function $M$:

$$ {}_1F_1(a; b; z) = M(a, b, z). \tag{2.35}$$

Fig. 2.7 shows the effective potential for different values of the magnetic field (which corresponds to different values of the magnetic length $l_B = \sqrt{2\hbar/m\omega_c}$). These potentials can be approximated again by the expression in Eq. (2.19) (see fit in Fig. 2.7). Therefore it is of higher relevance to determine the relation between $l_B$ and $\tilde{V}_{\text{eff}}(z = 0)$, since the value of $\tilde{V}(z = 0)$ will enable us to calculate $l_0/R$ (Eq. (2.20)) and therefore to reconstruct the effective potential for the whole range of $z-$values for an arbitrary magnetic field. Fig. 2.8 shows this curve for both electron and hole in the ground state and in the first excited state. This figure can be understood as follows. The larger the value of $l_B$, the smaller the magnetic field becomes and therefore the curve converges to the previously calculated value of $\tilde{V}_{\text{eff},l_B\to\infty}(z = 0)$ for $B = 0$. For small values of $l_B$, Eq. (2.19) matches the calculated curve, because for high magnetic fields, the confinement becomes effectively parabolic. Replacing the oscillator length

$l_0$ by $l_B$, the result for large magnetic fields is recovered:

$$\tilde{V}^{0,0}_{\text{eff},l_B\to 0}(z=0) = -\sqrt{\frac{\pi}{2}}\frac{1}{l_B/R}. \tag{2.36}$$

Putting together these results into a single formula, we obtain a fit for the effective potential as function of the magnetic field:

$$\tilde{V}^{0,0}_{\text{eff}}(z=0) = \tilde{V}^{0,0}_{\text{eff},l_B\to\infty}(z=0) - \sqrt{\frac{\pi}{2}}\frac{1}{\tilde{l}/R}e^{-pl_B}, \tag{2.37}$$

where $1/\tilde{l}^2 = 1/l_0^2 + 1/l_B^2$. Two parameters have been determined by fitting the data and are $l_0/R = 0.0624 \pm 0.0021$ and $pR = 8.570 \pm 0.090$ for the electron and the hole in the ground state configuration. Note that we have used the expression for parabolic confinement (Eq. (2.19)) where the effect of the magnetic field is included by replacing $l_0$ with $\tilde{l}$.

By making a similar calculation to the one in Ref. [84], but for the electron and hole in the first excited state, we find that

$$\tilde{V}^{0,1}_{\text{eff},l_B\to 0}(z=0) = -\frac{11}{16}\sqrt{\frac{\pi}{2}}\frac{1}{l_B/R} \tag{2.38}$$

Therefore we fitted the data for $|n_e, l_e\rangle = |n_h, l_h\rangle = |n, l\rangle = |0, 1\rangle$ to a slightly different function,

$$\tilde{V}^{0,1}_{\text{eff}}(z=0) = \tilde{V}^{0,1}_{\text{eff},l_B\to\infty}(z=0) - \frac{11}{16}\sqrt{\frac{\pi}{2}}\frac{1}{\tilde{l}/R}e^{-pl_B}, \tag{2.39}$$

where $l_0/R = 0.0462 \pm 0.0026$ and $pR = 10.73 \pm 0.17$. The numerical results together with the results of the fit are shown in Fig. 2.8 and agree very well.

### 2.6.3 Exciton energy

Previously, we calculated the exciton energy as a function of the dimensionless parameter $\alpha = a_B^*/2R$, which is determined by the wire radius and the material parameters. In this case, also the magnetic length affects the energy. Considering the previous results of the system without magnetic field and knowing that the shape of the potential does not fundamentally change by applying a magnetic field (the effective potential well only gets deeper), we know that also the energy as a function of $\alpha$ will not give a fundamentally different result as before. Therefore we calculated the binding energy as function of the magnetic field (or the magnetic length $l_B$) for a few fixed values of $\alpha$ ($\alpha = 10$, $\alpha = 1$ and $\alpha = 0.1$) and the result of these calculations can be seen in Fig. 2.9. The main figure shows only the ground state binding energy, while the inset shows also the energy of the first and second excited state. The inset further reveals that the magnetic field influences the ground state

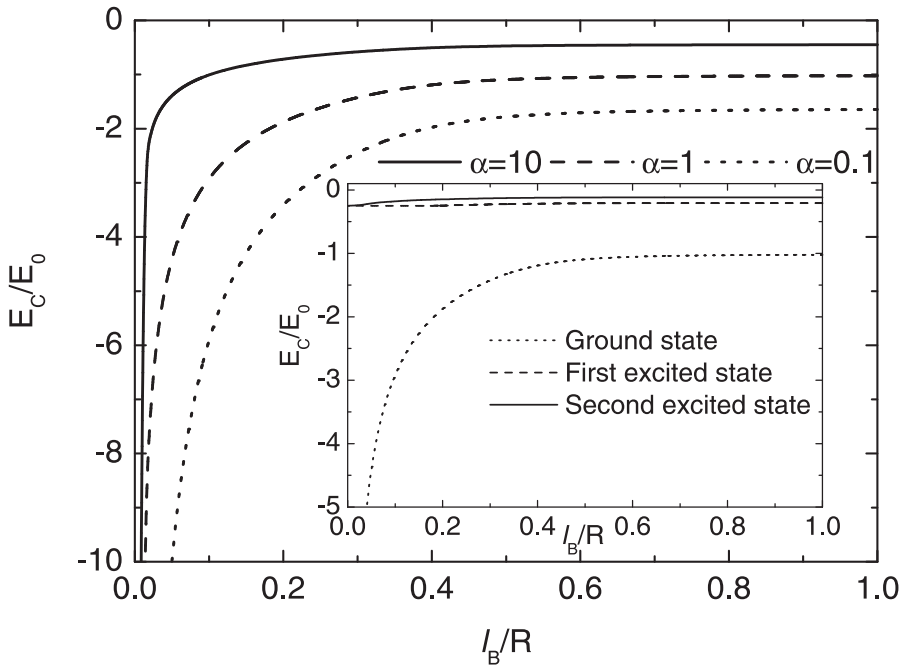


*Fig. 2.9* Ground state exciton binding energy for the electron and hole in the ground state as function of the magnetic length $l_B = \sqrt{2\hbar/eB}$ for different values of $\alpha$. Inset: the same but now for the ground state, first and second excited state with $\alpha = 1$.

more than the first and second excited states, which are almost constant. For high magnetic fields, corresponding with $l_B/R \to 0$, we find that the effective potential of Eq. (2.19) becomes a $1/z$-potential [86]. This means that we can use Eqs. (2.25)-(2.27) again to determine the asymptotic dependence of $\tilde{E}_C$ as function of $l_B$. We find that the ground state energy $\tilde{E}_C \to \infty$ for $l_B \to 0$ for all values of $\alpha$, whereas for $\alpha = 1$ (inset of Fig. 2.9) the first and second excited state become, in the limit $B \to \infty$, degenerate with energy $-1/4$.

## 2.7 CONCLUSION

In summary, we have calculated the effective interaction potential and the binding energy for an exciton in a nanowire without dielectric mismatch effects. The effective interaction potential was calculated for different states of the electron and hole and we were able to obtain 'exact' numerical results. In order to reduce the amount of computational time for future calculations, these results were used to propose various analytical approximate expressions. We fitted the results to three different functions. A first Padé approximation

gives the correct qualitative behaviour, but the fit was not optimal. Nevertheless this expression was useful to perform further analytical calculations to estimate the binding energy of the exciton, especially for small values of the wire radius $R$. A second Padé approximation as well as the result from the parabolic confinement resulted in very good fits. Furthermore, the exciton binding energy was calculated both semi-analytically and numerically and analytical approximations were given. We also investigated the influence of a magnetic field and determined an analytical expression for the effective potential for arbitrary magnetic field values. Finally we calculated the binding energy as a function of the magnetic field, where we found that the ground state binding energy is most affected by a variation of the magnetic field.

### Publications

The results in this chapter were published as:

- A.F. Slachmuylders, B. Partoens, W. Magnus, and F.M. Peeters, *Exciton states in cylindrical nanowires*, J. Phys.: Condens. Matter **18**, 3951 (2006).

# 3

# Excitons with dielectric mismatch

## 3.1 INTRODUCTION

In this chapter we will extend the work of the previous chapter and include the effect of the medium surrounding the wire which complicates the effective exciton potential while the correction to the Coulomb binding energy appears to be significant. Furthermore, we will limit ourselves from this moment on to the case where both electron and hole are found in the ground state configuration (i.e. $n = l = 0$). Due to the extra variable, the dielectric mismatch, it would be extremely time-consuming to perform similar calculations for other configurations. Therefore we proceed with both electron and hole in the ground state, the most obvious choice to obtain significant results.

Although excitons in nanowires with dielectric mismatch have been intensively studied previously [82, 90, 91, 92, 93], again much less effort has been dedicated to the construction of tractable analytical representations for the exciton potential accounting for the dielectric mismatch between the nanowire and its environment (vacuum, oxide, water, ...). Several fits have been suggested previously, but the accuracy is often to low to compute the exciton binding energy. In the present chapter, we will present more accurate expressions which are also tractable for future work.

In Ref. [90], a 6-band model was used to calculate the electron and hole wave functions. These wave functions were then used to average the six-dimensional (6D) interaction potential in order to obtain the effective exciton potential. An approximate expression for the effective potential of CdSe nanorods was used which allowed those authors to find analytical expressions for the energy

and wave functions of 1D excitons. However, the approximation for the effective potential is rather poor and the fitted parameters cannot be used to study other materials. A similar conclusion may be drawn for the expression suggested by Xia *et al.* [92]. Muljarov *et al.* [91] did not give an analytical expression and they used the numerically calculated effective potential to obtain the exciton binding energy which was then compared with experiment.

So we can conclude that time-consuming calculations have to be done over and over again for other materials. Therefore, we have performed calculations of the exciton potential and tested a Padé approximant for a significant range of dielectric permittivities covering a wide variety of materials. The parameters of this Padé approximation are then fitted as a function of the material parameters. We also constructed a set of fits that enables a quick and accurate reconstruction of the exciton potential. This allows us to study the exciton binding energy as a function of the dielectric mismatch, a result not presented in previous works.

This chapter is organized as follows. In Sect. 3.2, the analytical formalism we used is explained. In Sect. 3.3 the electrostatic potential with a dielectric mismatch is obtained. Sect. 3.4 presents the effective exciton interaction potential together with the Padé approximation used to fit this potential and Sect. 3.5 shows the results for the exciton binding energy. Our conclusions are given is Sec. 3.6.

## 3.2 HAMILTONIAN

The exciton Hamiltonian is given by the same expression as in Eq. 2.6, i.e.

$$\begin{aligned} H &= -\frac{\hbar^2}{2m_e}\vec{\nabla}_e^2 + V_e(x_e, y_e) - \frac{\hbar^2}{2m_h}\vec{\nabla}_h^2 + V_h(x_h, y_h) \\ &\quad + W\left(\vec{r}_e - \vec{r}_h\right), \end{aligned} \tag{3.1}$$

where $m_e$ ($m_h$) is the effective mass of the electron (hole), $V_e$ ($V_h$) is the confinement potential of the electron (hole) and $W\left(\vec{r}_e - \vec{r}_h\right)$ is the electrostatic potential due to the interaction between the electron and the hole. We used a different symbol for the electrostatic interaction compared to the symbol in Eq. 2.6, $V_C$, because due to the dielectric mismatch effects both expressions appear to be different.

Analogously to the previous chapter, we separate the motion of both particles into the motion of the center of mass and relative motion. We also adopt the adiabatic approximation again and average over the lateral coordinates, transforming the $6D$ Schrödinger equation into the following effective $1D$ equation:

$$\left(E_e + E_h + \frac{\hbar^2 K^2}{2M} - \frac{\hbar^2}{2\mu}\frac{\partial^2}{\partial z^2} + U_{\text{tot}}(z)\right)\phi(z) = E_{\text{tot}}\phi(z), \tag{3.2}$$

where $E_e$ ($E_h$) are the single-electron (hole) energies, and

$$U_{\rm tot}(z) = \iiiint {\rm d}x_e {\rm d}y_e {\rm d}x_h {\rm d}y_h W\left(\vec{r}_e - \vec{r}_h\right) \psi_e(x_e, y_e)\psi_h(x_h, y_h) \tag{3.3}$$

is the total exciton potential due to the Coulomb interaction, which will be discussed in the next section.

Introducing again the wire radius $R$ as the unit of length and denoting the permittivities of the wire and its surrounding medium by $\epsilon_1$ and $\epsilon_2$ respectively, we may rewrite the effective Schrödinger equation in terms of dimensionless quantities

$$\left(-\alpha \frac{\partial^2}{\partial z^2} + \tilde{U}_{\rm tot}(z)\right) \phi(z) = \tilde{E}_C \phi(z), \tag{3.4}$$

where in SI-units $\alpha = a_{\rm B}^*/2R$ with $a_{\rm B}^* = 4\pi\epsilon_1\hbar^2/\mu e^2$ the effective Bohr-radius of the exciton in the wire, $\tilde{U}_{\rm tot} = U_{\rm tot}/E_0$, $\tilde{E}_C = E_C/E_0$, $E_0 = e^2/4\pi\epsilon_1 R$, $E_C = E_{\rm tot} - E_e - E_h - \hbar^2 K^2/2M$ and $z$ is in units of $R$. Solving Eq. (3.4) yields the exciton energies. But in this procedure it is essential to have an accurate determination of the total 1D exciton potential $U_{\rm tot}(z)$ which will be presented in this chapter.

## 3.3 ELECTROSTATIC POTENTIAL WITH DIELECTRIC MISMATCH

The electron and hole interact via Coulomb forces, but due to the difference in dielectric permittivity inside ($\epsilon_1$) and outside ($\epsilon_2$) the wire, the Coulomb interaction will be distorted. We follow the approach of Ref. [82], and calculate first the potential $V_{\rm in/out}(\vec{r}, \vec{r}')$ at a point $\vec{r}$ due to a charge $e$ at $\vec{r}'$ *inside* a cylindrical wire. This is achieved by solving the appropriate Poisson equation

$$\begin{array}{lll} \epsilon_1 \nabla^2 V_{\rm in/out}(\vec{r}, \vec{r}') = -e\delta(\vec{r} - \vec{r}') & \text{for} & |\rho| \le R, \\ \epsilon_2 \nabla^2 V_{\rm in/out}(\vec{r}, \vec{r}') = 0 & \text{for} & |\rho| > R. \end{array} \tag{3.5}$$

where we introduced cylindrical coordinates $(\rho, \theta, z)$. Because Ref. [82] contains several typographical errors, we will repeat the calculation and give the major results. The potential at $\vec{r}$ for a charge located at $\vec{r}'$ is then given by

$$\begin{aligned} V_{\rm in}(\vec{r}, \vec{r}') = \frac{e}{4\pi\epsilon_1} \Bigg[ & \frac{1}{|\vec{r} - \vec{r}'|} + \frac{2}{\pi}\left(\frac{\epsilon_1}{\epsilon_2} - 1\right) \sum_{m=-\infty}^{+\infty} e^{im(\theta - \theta')} \\ & \times \int_0^\infty {\rm d}k \cos(k(z - z')) \mathbb{C}_m\left(kR, \frac{\epsilon_1}{\epsilon_2}\right) I_m(k\rho) I_m(k\rho') \Bigg] \end{aligned} \tag{3.6}$$

when the charge resides inside the wire, where

$$\mathbb{C}_m\left(kR, \frac{\epsilon_1}{\epsilon_2}\right) = \frac{K_m(kR) K_m'(kR)}{I_m(kR) K_m'(kR) - \frac{\epsilon_1}{\epsilon_2} I_m'(kR) K_m(kR)}. \tag{3.7}$$

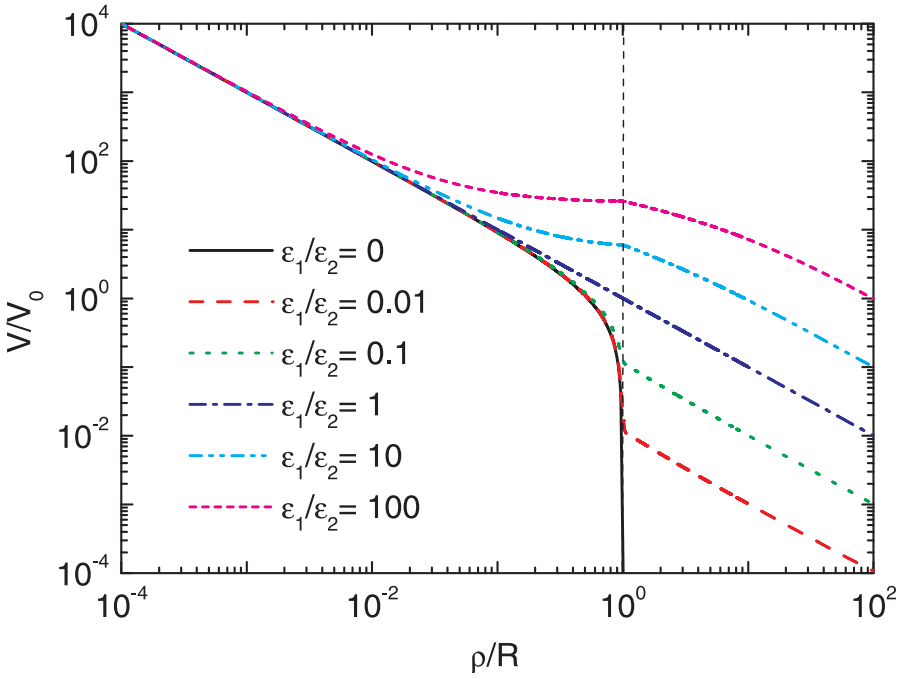


*Fig. 3.1* Potential $V$ at $\vec{r} = (\rho, 0, 0)$ due to a charge in $\vec{r}' = (0, 0, 0)$. $R$ is the wire radius and $V_0 = e/4\pi\epsilon_1 R$.

and $I_m(x)$, $K_m(x)$ are modified Bessel functions of the first and second kind. For the potential in a point outside the wire we have

$$V_{\rm out}(\vec{r}, \vec{r}') = \frac{2e}{4\pi^2\epsilon_1} \sum_{m=-\infty}^{+\infty} e^{im(\theta-\theta')} \int_0^\infty {\rm d}k \cos(k(z-z')) \left[ \frac{\left(\frac{\epsilon_1}{\epsilon_2} - 1\right) I_m(kR) K'_m(kR)}{\left(I_m(kR)K'_m(kR) - \frac{\epsilon_1}{\epsilon_2} I'_m(kR) K_m(kR)\right)} + 1 \right] I_m(k\rho') K_m(k\rho) \qquad (3.8)$$

In a similar way, we can calculate the potential $\bar{V}$ at a point $\vec{r}$ in case the charge at $\vec{r}'$ is located *outside* the wire. Therefore, we need to solve a slightly different Poisson equation from the one given by Eq. (3.5). Inside the wire we have

$$\bar{V}_{\rm in}(\vec{r}, \vec{r}') = \frac{2e}{4\pi^2\epsilon_2} \sum_{m=-\infty}^{+\infty} e^{im(\theta-\theta')} \int_0^\infty {\rm d}k \cos(k(z-z')) \left[ \frac{\left(\frac{\epsilon_1}{\epsilon_2} - 1\right) I'_m(kR) K_m(kR)}{\left(I_m(kR)K'_m(kR) - \frac{\epsilon_1}{\epsilon_2} I'_m(kR) K_m(kR)\right)} + 1 \right] K_m(k\rho') I_m(k\rho), \qquad (3.9)$$

and outside the wire

$$\bar{V}_{\text{out}}(\vec{r},\vec{r}') = \frac{e}{4\pi\epsilon_2}\left[\frac{1}{|\vec{r}-\vec{r}'|} + \frac{2}{\pi}\left(\frac{\epsilon_1}{\epsilon_2}-1\right)\sum_{m=-\infty}^{+\infty} e^{im(\theta-\theta')}\right.$$
$$\left.\int_0^\infty \mathrm{d}k\cos(k(z-z'))\mathbb{D}_m\left(kR,\frac{\epsilon_1}{\epsilon_2}\right)K_m(k\rho)K_m(k\rho')\right] \tag{3.10}$$

with

$$\mathbb{D}_m\left(kR,\frac{\epsilon_1}{\epsilon_2}\right) = \frac{I_m(kR)I'_m(kR)}{I_m(kR)K'_m(kR) - \frac{\epsilon_1}{\epsilon_2}I'_m(kR)K_m(kR)}. \tag{3.11}$$

As an illustration, the above potential is plotted in Fig. 3.1 as function of the radial distance to a charge placed in the center of the wire. It clearly shows how the Coulomb interaction is distorted due to the difference in permittivity in- and outside the wire: for $\epsilon_1/\epsilon_2 < 1$ the dielectric outside the wire screens more strongly the charge resulting in a strong reduction of the Coulomb potential. The limit $\epsilon_1/\epsilon_2 = 0$ corresponds to a wire surrounded by a metal (i.e. $\epsilon_2 = \infty$). The opposite case of $\epsilon_1/\epsilon_2 \to \infty$ corresponds to the case where the charges are strongly screened by the medium inside the wire. The presence of the medium outside the wire with a smaller permittivity leads to an enhancement of the Coulomb potential inside the wire.

Fig. 3.2 shows the dependence on the position of the charge for a fixed value of $\epsilon_1/\epsilon_2 = 10$, which is typical for III-V semiconductor nanowires in vacuum. Notice i) the $1/|\rho-\rho'|$ divergence, ii) for $\rho \gg \rho'$ the potential is independent on the position of the charge, while iii) for $\rho < \rho'$ this is not the case.

The next step is the calculation of the electrostatic energy $W(\vec{r}_e,\vec{r}_h)$ of the electron-hole pair inside the wire which is given by (with $e$ the charge of an electron)

$$\begin{aligned} W(\vec{r}_e,\vec{r}_h) &= \frac{1}{2}\int \mathrm{d}\vec{r}\,[e\delta(\vec{r}-\vec{r}_e) - e\delta(\vec{r}-\vec{r}_h)] \\ &\quad \times [V_{\text{in}}(\vec{r},\vec{r}_e) - V_{\text{in}}(\vec{r},\vec{r}_h)] \\ &= W_{\text{dir}} + W_{\text{ind}} + W_{\text{ind,S}} \end{aligned} \tag{3.12}$$

where

$$W_{\text{dir}}(\vec{r}_e,\vec{r}_h) = -\frac{e^2}{4\pi\epsilon_1}\frac{1}{|\vec{r}_e-\vec{r}_h|} \tag{3.13}$$

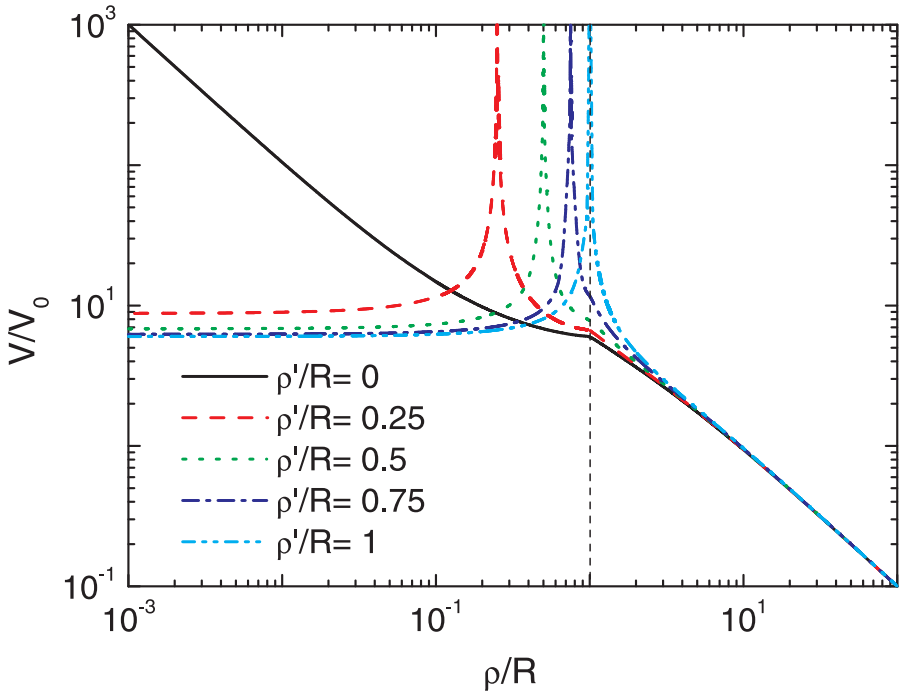


*Fig. 3.2* Potential $V$ at $\vec{r} = (\rho, 0, 0)$ due to a charge in $\vec{r}' = (\rho', 0, 0)$. $R$ is the wire radius and $V_0 = e/4\pi\epsilon_1 R$. $\epsilon_1/\epsilon_2$ has been set to 10.

is the direct Coulomb interaction in the absence of a dielectric mismatch and

$$W_{\mathrm{ind,S}}\left(\vec{r}_e, \vec{r}_h\right) = \frac{e^2}{4\pi^2\epsilon_1}\left(\frac{\epsilon_1}{\epsilon_2} - 1\right)\sum_{m=-\infty}^{+\infty}\int_0^\infty \mathrm{d}k\mathbb{C}_m\left(kR, \frac{\epsilon_1}{\epsilon_2}\right) \times \left[I_m^2(k\rho_e) + I_m^2(k\rho_h)\right] \tag{3.14}$$

$$W_{\mathrm{ind}}\left(\vec{r}_e, \vec{r}_h\right) = -2\frac{e^2}{4\pi^2\epsilon_1}\left(\frac{\epsilon_1}{\epsilon_2} - 1\right)\sum_{m=-\infty}^{+\infty}\int_0^\infty \mathrm{d}k\mathbb{C}_m\left(kR, \frac{\epsilon_1}{\epsilon_2}\right) [\cos(k(z_e - z_h))\cos(m(\theta_e - \theta_h))I_m(k\rho_e)I_m(k\rho_h)] \tag{3.15}$$

is the modification of this interaction due to the image charges induced by the difference in permittivity between the wire and its surrounding environment.

More precisely, the different contributions to the electrostatic energy $W$ are (also see Fig. 3.3):

- a direct contribution of the regular Coulomb potential $W_{\mathrm{dir}}$ (Eq. (3.13));
- a self-energy contribution from the interaction between an induced image charge and the original charge (that produces the image). This is

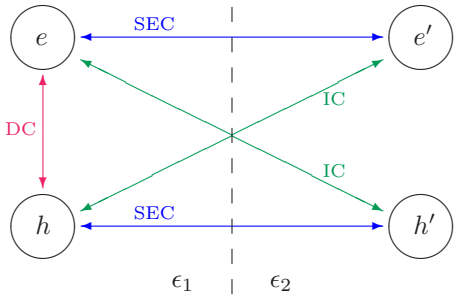


*Fig. 3.3* Schematical drawing of electron ($e$) and hole ($h$) near an interface with the indication of the different interactions between $e$ and $h$ and their images $e'$ and $h'$.

given by Eq. (3.14). This contribution $W_{\mathrm{ind,S}}$ as a function of the radial position of the particle is shown in Fig. 3.4. The divergence of $W_{\mathrm{ind,S}}$ at $\rho = R$ can be understood as follows: the contribution from $m = 0$ to the induced self-energy for the electron and for $\rho < R$ is proportional to

$$\mathbb{C}_0\left(kR, \frac{\epsilon_1}{\epsilon_2}\right) I_0^2(k\rho_e) \tag{3.16}$$

For $k \to \infty$ we know that $I_0(kR) \sim e^{kR}/\sqrt{2\pi kR}$ and $K_0(kR) \sim \sqrt{\pi/2kR}e^{-kR}$. Therefore, $\mathbb{C}_0 I_0^2(k\rho_e) \sim e^{2k(\rho_e - R)}/k\rho_e$, which leads to a finite integral as long as $\rho_e < R$. For $\rho_e = R$, the integrand is proportional to $1/k$ which implies that the integral diverges causing the total energy to be infinity;

- an induced contribution $W_{\mathrm{ind}}$ emerging from the interaction between a charge in the wire and the induced image charge (Eq. (3.15)).

## 3.4 EFFECTIVE EXCITON POTENTIAL

Adopting the adiabatic approximation and averaging over the ground state wave functions of the electron and hole, we obtain $U_{\mathrm{dir}}(z)$, $E_{\mathrm{self}}$ and $U_{\mathrm{ind}}(z)$. $U_{\mathrm{dir}}$ and $U_{\mathrm{ind}}$ depend on the dimensionless interparticle distance $z$ (in units of $R$) and adding them gives

$$U(z) = -\frac{e^2}{4\pi\epsilon_1 R}\frac{1}{\pi^2 J_1^4(\beta_{0,0})}\left(U_{\mathrm{ind}}(z) + U_{\mathrm{dir}}(z)\right), \tag{3.17}$$

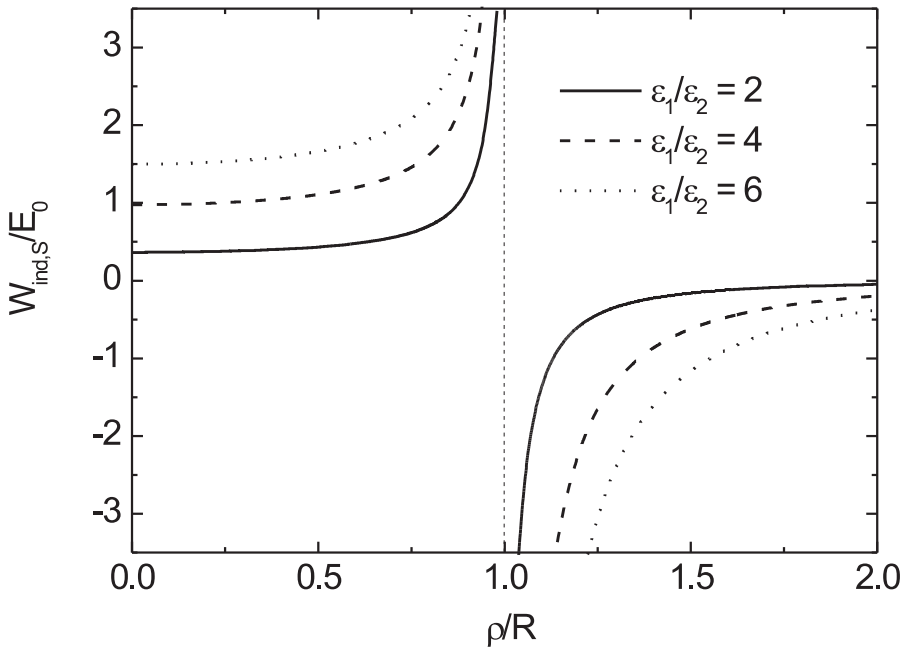


*Fig. 3.4* Self-energy $W_{\rm ind,S}$ contribution from the interaction between the induced image charge and the original charge (electron or hole) for different values of the ratio $\epsilon_1/\epsilon_2$. $W_{\rm ind,S}$ is given by Eq. (3.14). $R$ is the wire radius and $E_0 = e^2/4\pi\epsilon_1 R$.

where $\beta_{0,0} = 2.4048$ is the first zero of the Bessel function $J_0(x)$ and

$$
\begin{aligned}
U_{\rm ind}(z) &= 8\pi\left(\frac{\epsilon_1}{\epsilon_2}-1\right)\int_0^1 {\rm d}\rho_e\rho_e\int_0^1 {\rm d}\rho_h\rho_h J_0^2(\beta_{0,0}\rho_e) \\
&\quad\times J_0^2(\beta_{0,0}\rho_h)\int_0^\infty {\rm d}k\mathbb{C}_0\left(k,\frac{\epsilon_1}{\epsilon_2}\right) I_0(k\rho_e)I_0(k\rho_h)\cos(kz) \\
U_{\rm dir}(z) &= \int_0^1 {\rm d}\rho_e\int_0^1 {\rm d}\rho_h\int_0^{2\pi}{\rm d}\theta_e\int_0^{2\pi}{\rm d}\theta_h \\
&\times\frac{\rho_e\rho_h J_0^2(\beta_{0,0}\rho_e)J_0^2(\beta_{0,0}\rho_h)}{z^2+(\rho_e\cos\theta_e-\rho_h\cos\theta_h)^2+(\rho_e\sin\theta_e-\rho_h\sin\theta_h)^2}
\end{aligned}
\tag{3.18}
$$

with $\rho_e$, $\rho_h$, $\theta_e$ and $\theta_h$ dimensionless polar coordinates. The self-energy for the electron or hole does not depend on the interparticle distance and can be

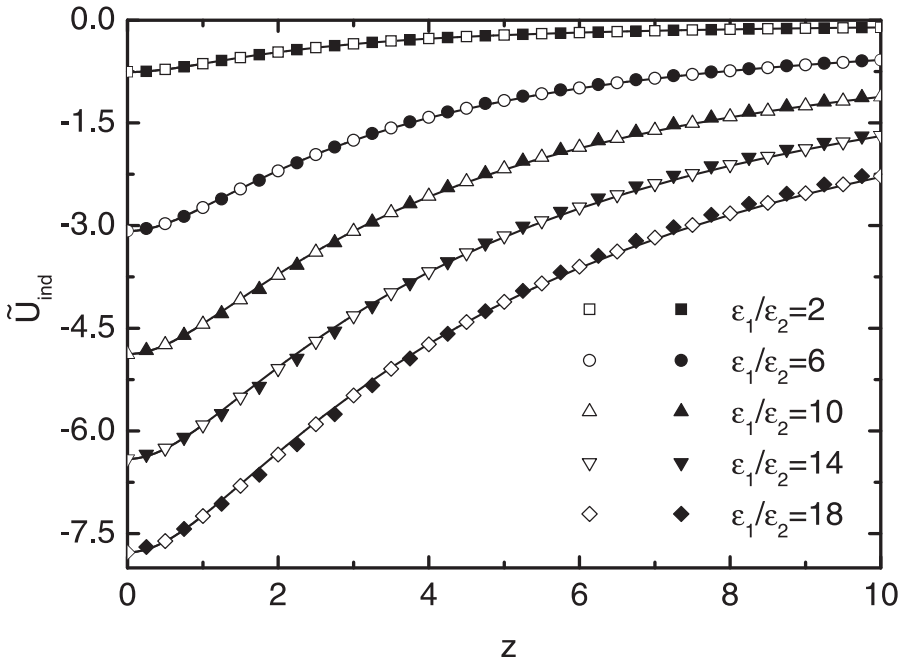


*Fig. 3.5* Induced potential for different ratios of the permittivities. The numerical results (full curves) together with the fits of Eq. (3.21) (open symbols) and Eq. (3.22) (unfilled symbols) are shown.

written as

$$E_{\rm self} = \frac{1}{2}\frac{e^2}{4\pi\epsilon_1 R}\frac{4}{\pi J_1^2(\beta_{0,0})}\left(\frac{\epsilon_1}{\epsilon_2}-1\right)\sum_{m=-\infty}^{+\infty}\int_0^\infty {\rm d}k \times\mathbb{C}_m\left(k,\frac{\epsilon_1}{\epsilon_2}\right)\int_0^1 {\rm d}\rho\rho I_m^2(k\rho)\left|J_0(\beta_{0,0}\rho)\right|^2 \tag{3.19}$$

with $U_{\rm tot}(z) = U(z) + 2E_{\rm self}$.

Since the numerical calculation of the effective potential is a CPU-intensive and time-consuming process, it is highly desirable to construct analytical expressions for it. In the previous chapter, we extensively studied the direct Coulomb interaction, $U_{\rm dir}$, and showed that it can be accurately fitted to the following simple Padé approximant which we used for further calculations:

$$\tilde{U}_{\rm dir} = \frac{\gamma\left|z\right|+\delta}{z^2+\eta\left|z\right|+\beta}, \tag{3.20}$$

with $\gamma = -1, \delta = -1.22, \eta = 1.13$ and $\beta = 0.47$ for the electron and hole in the ground state. Here, we focus on the calculation of the induced potential

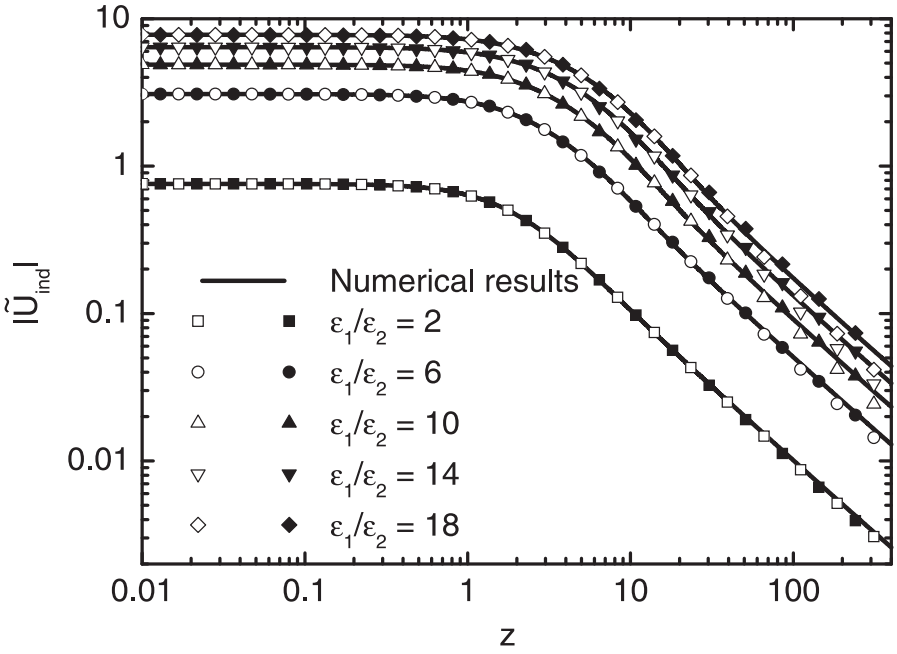


*Fig. 3.6* The same as Fig. 3.5 but now shown on a log-log scale.

$U_{\rm ind}$, which depends on the dielectric mismatch. The numerical results of these calculations can be seen in Fig. 3.5, together with the following two Padé approximants:

$$\tilde{U}_{\rm ind,1} = \frac{p\,|z| + q}{z^2 + r\,|z| + s} \tag{3.21}$$

and

$$\tilde{U}_{\rm ind,2} = \frac{az^2 + b\,|z| + c}{|z|^3 + dz^2 + e\,|z| + f}. \tag{3.22}$$

We found almost no difference between both Padé approximations for $\epsilon_1/\epsilon_2 = 2$ (the $\chi$-square for $\tilde{U}_{\rm ind,1}$ is $1.5 \cdot 10^{-7}$ and for $\tilde{U}_{\rm ind,2}$ is $1.2 \cdot 10^{-7}$, indicating that both fits are very good). As $\epsilon_1/\epsilon_2$ increases, the difference between $\tilde{U}_{\rm ind,1}$ and $\tilde{U}_{\rm ind,2}$ becomes noticeable. However, for $\epsilon_1/\epsilon_2 = 10$ and 18 the $\chi$-square results for $\tilde{U}_{\rm ind,1}$ is $2.6 \cdot 10^{-4}$ resp. $1.4 \cdot 10^{-3}$ while for $\tilde{U}_{\rm ind,2}$ we have $3.8 \cdot 10^{-5}$ resp. $1.3 \cdot 10^{-4}$, which indicates that the introduction of more fit parameters only slightly improves the result. When we go to a log-log plot of both Padé approximants together with the numerical results (Fig. 3.6) in order to show more clearly the small and large $z$ behavior, we can even conclude that the Padé approximant $P_2/P_3$ for large interparticle distances is less accurate than the $P_1/P_2$ approximant, where $P_n$ is a polynomial in $z$ of order $n$. A lower $\chi$-square was obtained for the $P_2/P_3$ approximant however, due to the excellent

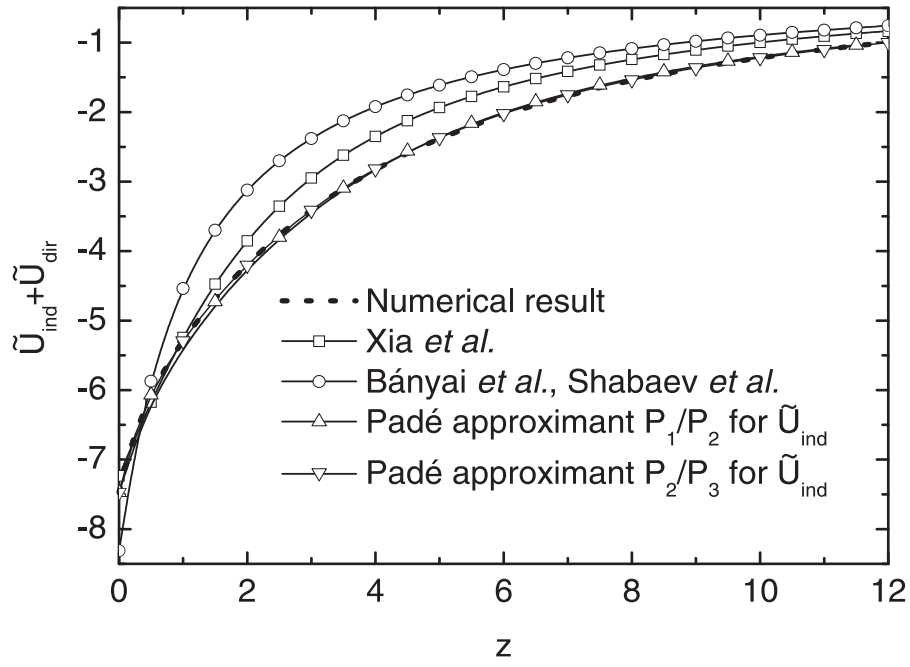


*Fig. 3.7* Plot of the effective exciton potential $\tilde{U}_{\rm dir}+\tilde{U}_{\rm ind}$ for $\epsilon_1/\epsilon_2=10$. The full thick line is the numerical result and the thin lines show the different fits: Eq. (3.23), Eq. (3.24), $P_1/P_2$ together with Eq. (3.20) and $P_2/P_3$ together with Eq. (3.20).

fit for small interparticle distances $z$. In previous papers, other fits were proposed for the effective exciton potential. E.g. Xia *et al.* [92] suggested

$$\tilde{U}_{\rm dir}+\tilde{U}_{\rm ind}=\frac{\epsilon_1}{\epsilon_2}\frac{-1}{|z|+\lambda e^{-\mu|z|}}, \tag{3.23}$$

with $\lambda=1.382$ and $\mu=0.421$ for $\epsilon_1/\epsilon_2=10$ whereas Bányai *et al.* [82] and Shabaev *et al.* [90] proposed the following fit formula:

$$\tilde{U}_{\rm dir}+\tilde{U}_{\rm ind}=\frac{\epsilon_1}{\epsilon_2}\frac{-1}{|z|+\upsilon}. \tag{3.24}$$

with $\upsilon=1.203$. In these papers the fit involved the total $z$-dependent exciton potential, i.e. the sum of the direct and induced potential, $\tilde{U}_{\rm dir}+\tilde{U}_{\rm ind}$. However, Fig. 3.7 shows that these fits produce significantly different results for the total of the direct and induced potential. A significantly better result is obtained with our $P_1/P_2$ approximant with parameters $p=-8.94$, $q=-56.43$, $r=2.11$ and $s=11.57$ and with the $P_2/P_3$ approximant with parameters $a=-7.33$, $b=146.65$, $c=226.88$, $d=8.21$, $e=30.07$ and $f=46.52$, as seen in Fig. 3.7. From now on, we will no longer consider the Padé approximant

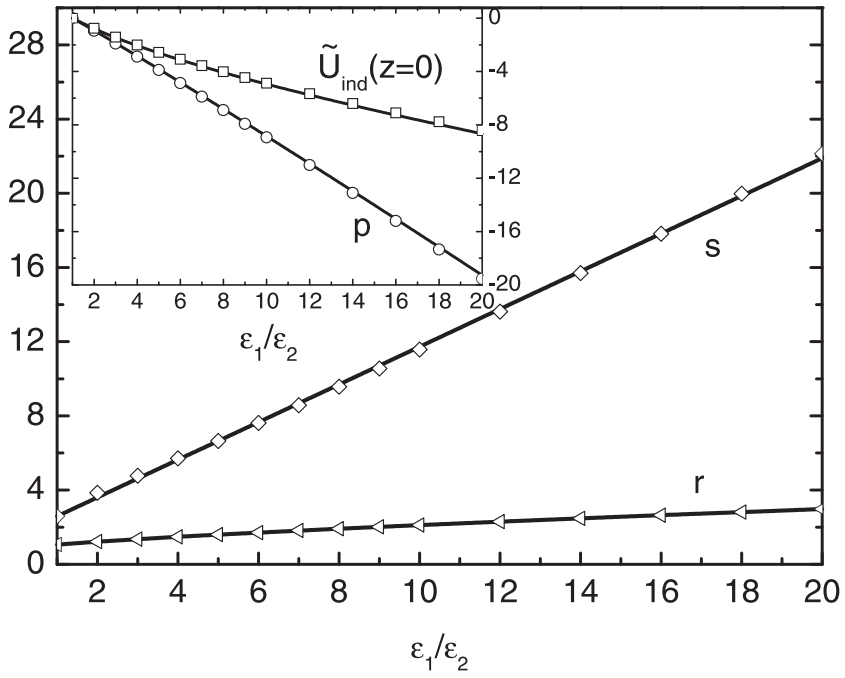


*Fig. 3.8* The fitting parameters as function of the dielectric mismatch. The full lines are the expressions of Eq. (3.28) and the numerically fitted parameters of Eq. (3.25) are given by the symbols.

$P_2/P_3$, since it does not lead to any significant improvement. Requiring that the first derivative of $\tilde{U}_{\rm ind}$ vanish at $z = 0$ and matching the fit function with the calculated value at $z = 0$, we obtain the following expressions which we fitted to the numerical results:

$$\tilde{U}_{\rm ind,1} = \frac{p\,|z| + \tilde{U}_{\rm ind}(z=0)s}{z^2 + r\,|z| + s} \tag{3.25}$$

In this case we have also taken the correct behavior for $z \to 0$ into account, because it should be noted that we can write $\tilde{U}_{\rm ind}$ of Eq. (3.18) as follows:

$$\tilde{U}_{\rm ind}(z) = \int_0^\infty f(k)\cos(kz). \tag{3.26}$$

The function $f(k)$ is a complicated function depending on $k$ but not on $z$. $f(k)$ exhibits a logarithmic divergence for $k \to 0$. Consequently, since for $z \approx 0$ we can write that $\cos(kz) = 1 + (1/2)z^2k^2 + \ldots$, we find that

$$\tilde{U}_{\rm ind}(z \to 0) = A + Bz^2 + \ldots \tag{3.27}$$

with $A$ and $B$ constants.

The parameters for Eq. (3.25) were determined for a wide range of permittivities. In Fig. 3.8 we show these fit parameters as a function of the dielectric mismatch ratio, $\epsilon_1/\epsilon_2$. In the range $1 < \epsilon_1/\epsilon_2 < 20$ we obtained the following simple fit expressions:

$$p = 0.86\left(1-(\epsilon_1/\epsilon_2)^{1.05}\right), \tag{3.28a}$$

$$r = 0.84 + 0.23(\epsilon_1/\epsilon_2)^{3/4}, \tag{3.28b}$$

$$s = 1.57 + 1.02(\epsilon_1/\epsilon_2), \tag{3.28c}$$

$$\tilde{U}_{\rm ind}(z=0) = 1.36\left(1-(\epsilon_1/\epsilon_2)^{2/3}\right). \tag{3.28d}$$

Avoiding time-consuming numerical calculations, we may use the above mentioned fit-formulas to quickly and accurately construct the exciton potential for a wide range of $\epsilon_1/\epsilon_2$-values appearing in any further calculations.

The only thing left to calculate is the self-energy, i.e. Eq. (3.19). Comparing various free-standing quantum wires, we particularly have to deal with the case where the dielectric constant of the wire ($\epsilon_1/\epsilon_0$) typically varies from one to twenty while $\epsilon_2/\epsilon_0$ remains fixed to some constant value, say 1. In that case it proves convenient to express the self-energy in terms of $E_0' = e^2/4\pi\epsilon_2 R$ which is independent of $\epsilon_1$. We found that the self-energy can be fitted adequately to the expression

$$\frac{E_{\rm self}}{E_0'} = \frac{a\left((\epsilon_1/\epsilon_2)^b - 1\right)}{\epsilon_1/\epsilon_2} \tag{3.29}$$

with $a = 0.89$ and $b = 0.59$. The numerically calculated self-energy is plotted and compared with its analytical fit formula in Fig. 3.9. Clearly, $E_{\rm self}/E_0'$ attains a maximum value of 0.285 around $\epsilon_1/\epsilon_2 = 4.7$. This is very different from the results for a quantum dot reported in Ref. [94] where it was shown that the dominant contribution to the self-energy in a quantum dot is $1/2(1-\epsilon_2/\epsilon_1)$ which reduces to 0.5 when $\epsilon_1/\epsilon_2 \to \infty$. Consequently, the maximal self-energy of the dot is roughly twice as large as the maximum attained in the wire. This can be explained as a dimensional effect in the sense that surface effects in a 0D structure are significantly more important than in wires where the self-energy vanishes as $\tilde{E}_{\rm self}/E_0' \to 0.89(\epsilon_1/\epsilon_2)^{-0.41}$ for $\epsilon_1/\epsilon_2 \to \infty$.

## 3.5 EXCITON BINDING ENERGY

Using the analytical representation of the induced exciton potential as given by the Padé approximant (Eq. (3.25)), we are able to construct the complete exciton potential and solve the effective 1D Schrödinger equation. As was indicated before, the natural unit $E_0$ that arises when calculating the effective exciton potential, is no longer the most appropriate unit to study the energy. Also we found that some choices of units may lead to confusing results and therefore we have chosen to rewrite the Schrödinger equation Eq. (3.4) as

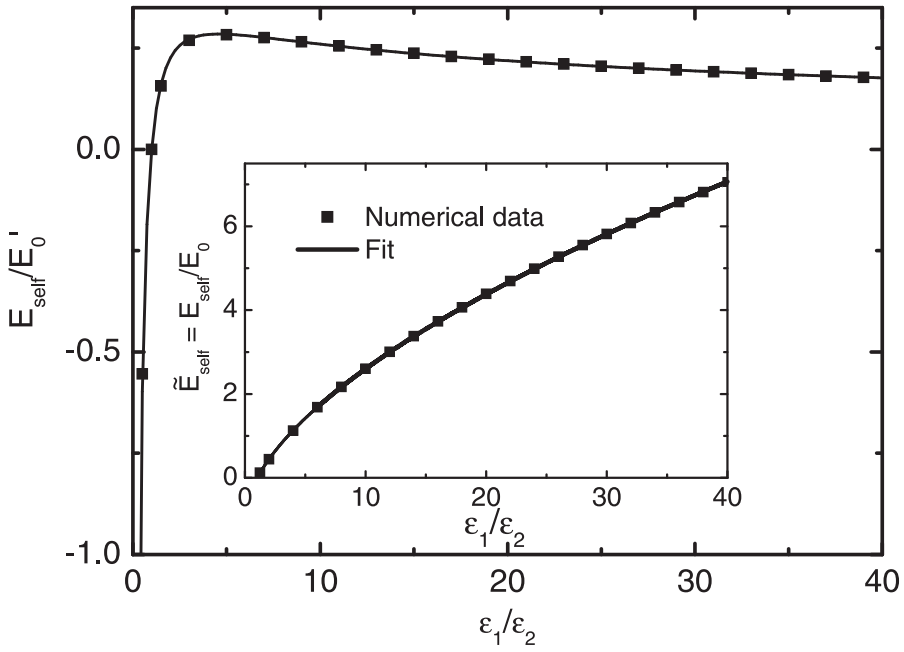


*Fig. 3.9* Self-energy as function of the ratio of dielectric constants in units of $E_0' = e^2/4\pi\epsilon_2 R$ and (inset) $\tilde{E}_{\rm self}$, i.e. $E_{\rm self}$ is in units of $E_0 = e^2/4\pi\epsilon_1 R$. The fit (full lines) of Eq. (3.29) agrees very well with the numerical results (symbols).

follows:

$$\left(-\frac{1}{2}\left(\frac{1}{R/a^*_{B,0}}\right)^2\frac{\partial^2}{\partial z^2}+\frac{U_{\rm tot}}{E_0''}\right)\phi(z)=\frac{E_C}{E_0''}\phi(z), \tag{3.30}$$

where $E_0'' = e^2/4\pi\epsilon_0 a^*_{B,0}$ with $a^*_{B,0} = 4\pi\epsilon_0\hbar^2/\mu e^2$. Typical values for these energy and length units are for GaAs: $E_0'' = 1.58$ eV, $a^*_{\rm B,0} = 0.91$ nm, Si: $E_0'' = 8.86$ eV, $a^*_{\rm B,0} = 0.16$ nm, Ge: $E_{0,}'' = 6.49$ eV, $a^*_{\rm B,0} = 0.22$ nm, InP: $E_0'' = 1.91$ eV, $a^*_{\rm B,0} = 0.75$ nm, where we used the bulk electron and heavy hole masses. Since we calculated and fitted the potential $U_{\rm tot}$ in units of $E_0$, we find that the conversion factor between both units for the potential is given by $(\epsilon_0/\epsilon_1)(a^*_{B,0}/R)$, resulting in

$$\left(-\frac{1}{2}\left(\frac{1}{R/a^*_{B,0}}\right)^2\frac{\partial^2}{\partial z^2}+\frac{\epsilon_0}{\epsilon_1}\frac{1}{R/a^*_{B,0}}\frac{U_{\rm tot}}{E_0}\right)\phi(z)=\frac{E_C}{E_0''}\phi(z), \tag{3.31}$$

for the Schrödinger equation. Having now rewritten the Schrödinger equation, we can easily plug in our previous results to find the energy $E_C/E_0''$. Note that we have to leave out the self-energy given in Eq. (3.19), i.e. a constant energy shift amounting to a mere renormalization of the bandgap, to

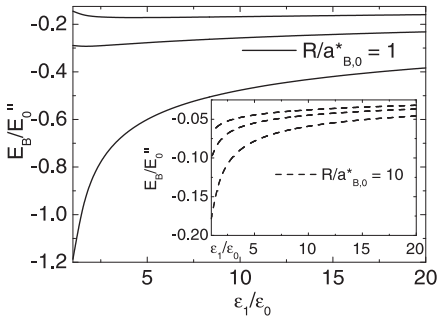


*Fig. 3.10* Lowest three energy levels of the exciton as function of the permittivity for $R/a^*_{B,0} = 1$ and (inset) $R/a^*_{B,0} = 10$, $\epsilon_2/\epsilon_0 = 1$.

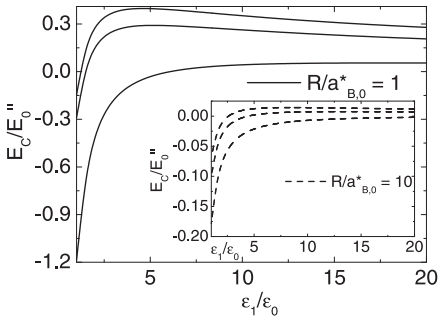


*Fig. 3.11* Plot of the PL energy (ignoring the bandgap energy) as function of the permittivity for $R/a^*_{B,0} = 1$ and (inset) $R/a^*_{B,0} = 10$, $\epsilon_2/\epsilon_0 = 1$.

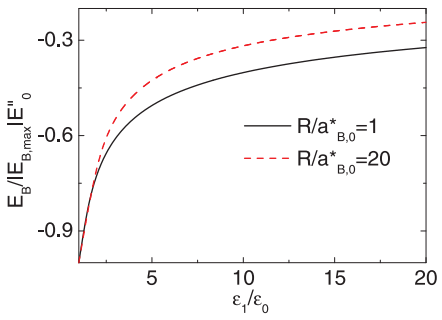


*Fig. 3.12* Normalized ground state X energy levels as function of the mismatch for $R/a^*_{B,0} = 1$ ($|E_{\mathrm{B,max}}| = 1.19$) and $R/a^*_{B,0} = 20$ ($|E_{\mathrm{B,max}}| = 0.097$) with $\epsilon_2/\epsilon_0 = 1$.

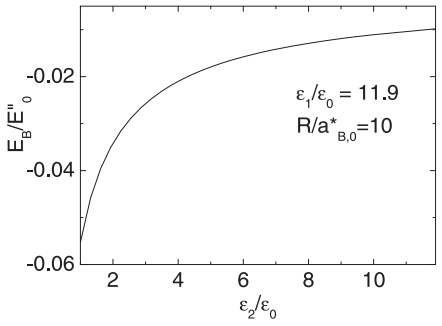


*Fig. 3.13* Binding energy for fixed wire parameters ($\epsilon_1/\epsilon_0 = 11.9$ and $R/a^*_{B,0} = 10$) as function of the condition outside the wire.

calculate the actual exciton binding energy $E_B$, so we have $E_B = E_C - 2E_{\mathrm{self}}$, where the factor of 2 arises since the self-energy of both electron *and* hole has to be taken into account. Fig. 3.10 shows the excitonic ground state and the first few excited states as a function of the dielectric permittivity $\epsilon_1/\epsilon_0$ for different values of the dimensionless parameter $R/a^*_{B,0}$. As a result, it follows that the effect of the dielectric mismatch on the exciton binding energy is significant and may not be neglected when the optical properties of a quantum wire are investigated. Note that the binding energy generally changes the most between $\epsilon_1/\epsilon_0 = 1$ and 5. Also note that the self-energy changes depending on the dielectric mismatch ratio and therefore the normalization of the bandgap also constantly changes. To illustrate this, we also plotted $E_C$, which corresponds to the PL energy minus the bandgap energy. This is

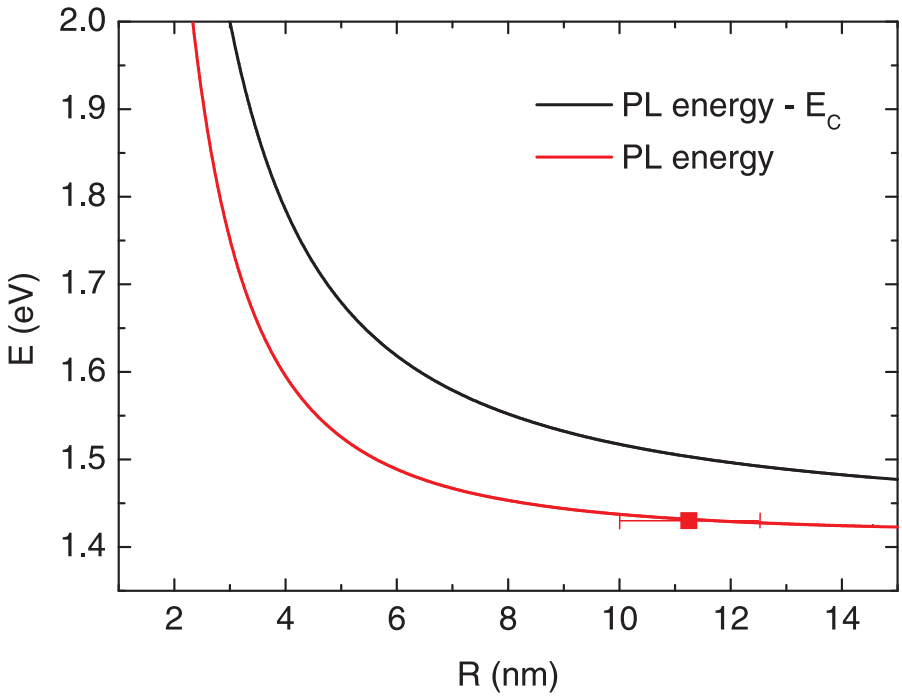


*Fig. 3.14* PL energy (red curve) for InP wires as a function of the wire radius. The experimental result (red square) from Ref. [95] is found to compare very well with our theoretical calculations. The energy without the negative Coulomb contribution (black curve) can be found above the PL energy.

shown in Fig. 3.11. Also notice in Fig. 3.12, where normalized curves of the ground state energy for both $R/a^*_{B,0} = 1$ and $R/a^*_{B,0} = 20$ are shown, how for an increasing radius the exciton binding energy starts to show a stronger $\epsilon_1$-dependence. This is as expected, since for bulk materials the binding energy goes as $1/\epsilon_1^2$. We compared our results with experimental results on InP and CdSe wires in chrysotile asbestos [91]. Muljarov *et al.* found an estimated exciton binding energy $E_B = 192$ meV for $R = 2$ nm InP wires. For CdSe wires, $E_B = 257$ meV for $R = 2$ nm and $E_B = 224$ meV for $R = 4.8$ nm. According to our calculations, we find for InP $E_B = 211$ meV while for CdSe $E_B = 271$ meV ($R = 2$ nm) and $E_B = 233$ meV ($R = 2.4$ nm). In view of the fact that we used a simple two band model, we find that our theoretical results compare rather well with the experimental values reported in Ref. [91] and overestimates the exciton binding energy with about 5-10%. The following parameters were used in our calculations. For InP: $m_e = 0.079m_0$, $\gamma_1 = 4.94$, $\gamma_2 = 1.65$, $E_g = 1.4236$ eV ($T = 2$K), and $\epsilon_1 = 9.61$; for CdSe: $m_e = 0.12m_0$, $m_h = 0.45m_0$, $E_g = 1.751$, $\epsilon_1 = 5.8$; for chrysotile asbestos $E_g = 4$ eV and $\epsilon_2 = 2.2$. Bearing in mind that spill-over effects necessarily take place for

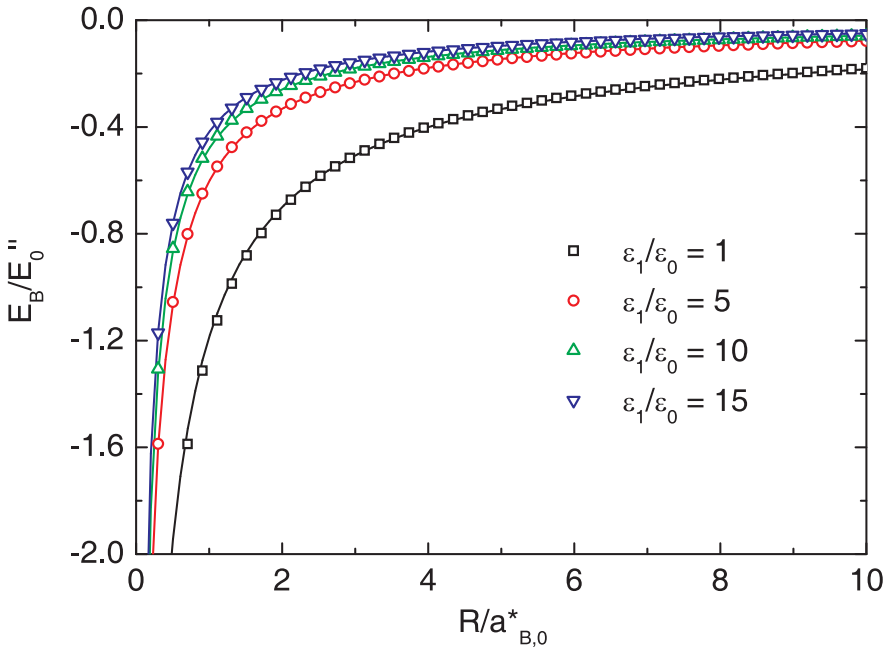


*Fig. 3.15* Ground state binding energy of the exciton as function of $R/a^*_{B,0}$ for different values of the dielectric mismatch ($\epsilon_2/\epsilon_1 = 1$). The numerical results (open symbols) are shown together with the fits (full lines) of Eq. (3.32).

InP and CdSe wires in a chrysotile asbestos matrix, the effective confinement will be lowered, resulting in a lower binding energy. Also note that the binding energies for wires with a dielectric mismatch are significantly larger than for wires with no dielectric mismatch. Excluding the dielectric mismatch we found $E_B = 64$ meV for an InP wire with $R = 2$ nm and for the CdSe wires of $R = 2$ nm and $R = 2.4$ nm we obtained $E_B = 134$ meV and $E_B = 117.2$ meV resp. To emphasize the difference between a wire with and without a dielectric mismatch, we plotted the exciton binding energy for $\epsilon_1/\epsilon_0 = 11.9$, while the dielectric constant of the surrounding medium, $\epsilon_2/\epsilon_0$, is changing (Fig. 3.13 ). This is different from Figs. 3.10 and 3.11, where $\epsilon_2/\epsilon_0$ was set to 1 and $\epsilon_1/\epsilon_0$ was varied. Fig. 3.13 clearly shows the difference between a wire with and without mismatch, the exciton binding energy is enhanced by a factor of $\propto 5.5$ by placing the wire in an environment that causes a high mismatch. We also compared our calculations with the results found in Ref. [95]. InP freestanding nanowires were produced with a diameter range of 20 - 25 nm. For these wires, a PL peak appeared at 1.432 eV, whereas our theoretical calculations predict a PL peak position at 1.432 eV for a freestanding wire with a diameter of 22.5 nm (see Fig. 3.14). In the figure, the PL energy

*Table 3.1* Fit parameters for the exciton binding energy as a function of the wire radius (Eq. (3.32)).

| | $\xi$ | $\sigma$ |
|---|---|---|
| $\epsilon_1/\epsilon_0 = 1$ | -2.45 | 1.07 |
| $\epsilon_1/\epsilon_0 = 5$ | -0.87 | 0.44 |
| $\epsilon_1/\epsilon_0 = 10$ | -0.64 | 0.33 |
| $\epsilon_1/\epsilon_0 = 15$ | -0.54 | 0.29 |

was plotted as a function of the wire radius together with the curve without Coulomb binding energy to illustrate the effect of this binding energy in a freestanding wire.

Next, we investigate the energy as function of the wire radius. This is shown in Fig. 3.15. This figure emphasizes again that a change in dielectric mismatch will have the strongest effect for small values of the mismatch and that mismatch effects will become less important for larger radii. The numerical results of Fig. 3.15 can be fitted to an analytical expression. In the previous chapter, we already introduced an analytical expression for the binding energy as function of the wire radius for $\epsilon_1/\epsilon_0 = 1$ and $\epsilon_2/\epsilon_0 = 1$ (Eq. 2.21). Based on these results, we suggest the following fitting curve:

$$\frac{E_B}{E_0''} = \frac{1}{R/a^*_{\mathrm{B},0}} \frac{\xi}{1 + \sigma/\sqrt{R/a^*_{\mathrm{B},0}}} \tag{3.32}$$

with the fit parameters given in Table 3.1.

The fits are also shown in Fig. 3.15. This figure illustrates the importance of the Coulomb interaction and how it grows as the radius of the wire is reduced.

## 3.6 CONCLUSION

We proposed an appropriate analytical formula for the effective exciton potential in a semiconductor quantum wire, which accounts for the effect of dielectric mismatch for a wide variety of semiconductor permittivities. The different parameters in the formula have been fitted to several expressions, which enables a quick reconstruction of the complete effective exciton potential for different dielectric permittivities. The formula greatly facilitates the determination of the energy levels of the exciton (i.e. ground and excited states) while drastically reducing the computation time (by as much as a factor of 100) and can be used for further calculation the optical oscillator strengths. Furthermore, the self energy and the binding energy was studied as a function of the dielectric mismatch. It was shown that a change in dielectric constant of the wire material between one to five has a significantly larger influence on

the total energy then a change from e.g. five to ten. Although we only used a simple two band model, we find that our theoretical results compare rather well with the experimental values reported in several papers. Also the binding energy as function of the wire radius was calculated for different values of the dielectric mismatch and fitted to an analytical expression.

### Publications

The results in this chapter were published as:

- A.F. Slachmuylders, B. Partoens, W. Magnus, and F.M. Peeters, *Dielectric mismatch effects on the exciton states in cylindrical nanowires*, Phys. Rev. B **74**, 235321 (2006).
- The paper Phys. Rev. B **74**, 235321 (2006) was also selected to appear in the Virtual Journal of Nanoscale Science and Technology, July 3 edition (2007).
- A.F. Slachmuylders, B. Partoens, W. Magnus, and F.M. Peeters, *Excitons and trions in cylindrical nanowires with dielectric mismatch*, Phys. Stat. Sol. (c) **5**, 2416 (2008).
- A.F. Slachmuylders, B. Partoens, W. Magnus, and F.M. Peeters, *The effect of dielectric mismatch on excitons and trions in cylindrical semiconductor nanowires*, to appear in Journal of Computational Electronics.
- A.F. Slachmuylders, B. Partoens, W. Magnus, and F.M. Peeters, *The effect of the dielectric mismatch on excitons and trions in freestanding nanowires*, Phys. E **40**, 2166 (2008).

# 4

# *Trions with dielectric mismatch*

## 4.1 INTRODUCTION

When an additional electron or hole is bound to an exciton ($X$), a charged exciton or *trion* ($X^+$ or $X^-$) is formed. Its existence in bulk semiconductors was first predicted theoretically in the 1950's by Lampert [72], but due to the low binding energies, trions could only be observed in bulk materials at very low temperatures [96, 97], restricting the practical relevance of these many particle systems. Nevertheless, trions become of importance when the dimensionality is reduced: confinement results in enhanced binding energies [98, 99] and consequently these complexes become observable at higher temperatures.

Stability of negative and positive trions has been investigated previously in quantum wires [101], rods [102], wells [103] and dots [104] but, to our knowledge, nobody has investigated trions in wires in the presence of a dielectric mismatch, which is the goal of this work. When the Coulomb interaction is small as compared to the radial confinement, the adiabatic approximation can be used which reduces the problem from a 9D to a 2D problem. Within the framework of the effective mass approximation, the reduced Schrödinger equation will be solved numerically using the finite element technique that enables us to calculate the trion binding energies for a whole range of wire materials and wire surroundings. Extending our work of the previous chapters on quantum wire excitons, we will calculate positive and negative trion binding energies as function of hole and electron mass ratio, dielectric constants and wire radius. Also the trion wave function will be investigated.

This chapter is organized as follows: In Sect. 4.2 we focus on the theoretical calculation and present the effective trion Hamiltonian. In Sect. 4.3, we construct the trion potential, with the aid of our previously obtained results on excitons. The calculation of the trion binding energy and wave function is presented in Sect. 4.4. Finally, we summarize our main results in Sect. 4.5.

## 4.2 HAMILTONIAN

The trion Hamiltonian in the effective mass approximation is given by

$$H_{\pm} = \sum_i \left( -\frac{\hbar^2}{2m_i}\vec{\nabla}_i^2 + V_i\left(\vec{r}_i\right)\right) + \sum_{i<j} W\left(\vec{r}_i - \vec{r}_j\right), \tag{4.1}$$

where the index $i = e_1, e_2, h$ for $X^-$ while $i = h_1, h_2, e$ for $X^+$; $e_i(h_i)$ refers to electron (hole) and $V_i\left(\vec{r}_i\right)$ is the particle confinement potential. $W\left(\vec{r}_i - \vec{r}_j\right)$ is the electrostatic potential energy due to interparticle interaction, which will be discussed later.

From now on, we focus on the calculations for $X^-$ as the results for $X^+$ can be obtained in a similar way. Again, we assume that the lateral confinement is sufficiently large to decouple the lateral and transverse motion, so we can write the trion wave function as

$$\begin{aligned}\Psi(\vec{r}_{e_1}, \vec{r}_{e_2}, \vec{r}_h) &= \psi_e(x_{e_1}, y_{e_1})\psi_e(x_{e_2}, y_{e_2})\psi_h(x_h, y_h) \\ &\quad \times\chi_-(z_{e_1}, z_{e_2}, z_h).\end{aligned} \tag{4.2}$$

The simplified Hamiltonian now reads

$$H_- = H_{e_1} + H_{e_2} + H_h + H_-^{\text{eff}} \tag{4.3}$$

where $H_{e_1,e_2,h}$ are the Hamiltonians of the non-interacting particles and

$$\begin{aligned}H_-^{\text{eff}} &= -\frac{\hbar^2}{2m_e}\left[\frac{\partial^2}{\partial z_{e_1}^2} + \frac{\partial^2}{\partial z_{e_2}^2}\right] - \frac{\hbar^2}{2m_h}\frac{\partial^2}{\partial z_h^2} \\ &\quad + U_{\text{tot}}(z_{e_1}, z_{e_2}, z_h),\end{aligned} \tag{4.4}$$

with

$$\begin{aligned}U_{\text{tot}}(z_{e_1}, z_{e_2}, z_h) = \int_{\text{wire}} &\mathrm{d}x_{e_1}\mathrm{d}y_{e_1}\mathrm{d}x_{e_2}\mathrm{d}y_{e_2}\mathrm{d}x_h\mathrm{d}y_h \\ &\times \left(W\left(\vec{r}_{e_1} - \vec{r}_h\right) + W\left(\vec{r}_{e_2} - \vec{r}_h\right) + W\left(\vec{r}_{e_1} - \vec{r}_{e_2}\right)\right) \\ &\times \left|\psi_e(x_{e_1}, y_{e_1})\right|^2 \left|\psi_e(x_{e_2}, y_{e_2})\right|^2 \left|\psi_h(x_h, y_h)\right|^2.\end{aligned} \tag{4.5}$$

Finally, we reduce the effective Hamiltonian, by introducing the center-of-mass coordinate $Z$ and the relative electron-hole positions $z_{h1}$ and $z_{h2}$:

$$Z = \frac{z_{e_1} + z_{e_2} + \sigma z_h}{2+\sigma}, \tag{4.6}$$

$$z_{h1} = z_h - z_{e_1}, \tag{4.7}$$

$$z_{h2} = z_h - z_{e_2}, \tag{4.8}$$

yielding

$$H_-^{\text{eff}} = -\frac{\hbar^2}{m_e}\frac{1}{2M}\frac{\partial^2}{\partial Z^2} + H_-^{\text{rel}}, \tag{4.9}$$

where $M = 2+\sigma$ is the $X^-$ trion mass and $\sigma = m_h/m_e$ the hole to electron mass ratio. With $\mu = \sigma/(1+\sigma)$ the reduced mass of an electron-hole pair, we can write

$$\begin{aligned} H_-^{\text{rel}} &= \frac{\hbar^2}{m_e}\left[-\frac{1}{2\mu}\left(\frac{\partial^2}{\partial z_{h1}^2} + \frac{\partial^2}{\partial z_{h2}^2}\right) - \frac{1}{\sigma}\frac{\partial^2}{\partial z_{h1}\partial z_{h2}}\right] \\ &\quad + U_{\text{tot}}(z_{h1}, z_{h2}), \end{aligned} \tag{4.10}$$

which allows us to separate the wave function $\chi_-$ into a product of the center of mass and relative wave functions, i.e. $\chi_- = \chi_{\text{CM}}(Z)\chi(z_{h1}, z_{h2})$ and to reduce the original problem to the solution of a 2D Schrödinger equation.

Analogously, a positive trion $X^+$ may be represented by

$$\begin{aligned} H_+^{\text{rel}} &= \frac{\hbar^2}{m_e}\left[-\frac{1}{2\mu}\left(\frac{\partial^2}{\partial z_{h1}^2} + \frac{\partial^2}{\partial z_{h2}^2}\right) - \frac{\partial^2}{\partial z_{h1}\partial z_{h2}}\right] \\ &\quad + U_{\text{tot}}(z_{h1}, z_{h2}), \end{aligned} \tag{4.11}$$

where $z_{h1}$ and $z_{h2}$ denote the relative position coordinates of the first and second hole with respect to the electron position.

## 4.3 EFFECTIVE 2D TRION POTENTIAL

In order to calculate the effective 2D potential $U_{\text{tot}}$ mentioned in Eq. (4.10), we need an explicit expression for $W_{\text{tot}} = W(\vec{r}_{e_1} - \vec{r}_h) + W(\vec{r}_{e_2} - \vec{r}_h) + W(\vec{r}_{e_1} - \vec{r}_{e_2})$. For that purpose we express $W_{\text{tot}}$ in terms of the electrostatic potential $V_{\text{in}}$, the potential inside a wire at a point $\vec{r} = (\rho, \theta, z)$ due to a charge $e$ at $\vec{r} = (\rho', \theta', z')$

$$\begin{aligned} W_{\text{tot}} &= \frac{1}{2}\int \mathrm{d}\vec{r}\,[e\delta(\vec{r} - \vec{r}_{e_1}) + e\delta(\vec{r} - \vec{r}_{e_2}) - e\delta(\vec{r} - \vec{r}_h)] \\ &\quad \times [V_{\text{in}}(\vec{r}, \vec{r}_{e_1}) + V_{\text{in}}(\vec{r}, \vec{r}_{e_2}) - V_{\text{in}}(\vec{r}, \vec{r}_h)]\,. \end{aligned} \tag{4.12}$$

An expression for $V_{\text{in}}(\vec{r}, \vec{r}')$ can be found in Eq. 3.6. We follow the same approach as in Chapter 3 and we subtract the electrostatic self-energy coming

from the terms proportional to

$$\frac{\delta(\vec{r}-\vec{r}_{e_1})}{|\vec{r}-\vec{r}_{e_1}|}+\frac{\delta(\vec{r}-\vec{r}_{e_2})}{|\vec{r}-\vec{r}_{e_2}|}+\frac{\delta(\vec{r}-\vec{r}_h)}{|\vec{r}-\vec{r}_h|} \tag{4.13}$$

in the integral of Eq. (4.12) yielding the total interaction energy

$$\delta W = W_{\rm dir}+W_{\rm ind}+W_{\rm ind,S}, \tag{4.14}$$

where

$$W_{\rm dir}\left(\vec{r}_{e_1},\vec{r}_{e_2},\vec{r}_h\right) = \frac{e^2}{4\pi\epsilon_1}\left(\frac{1}{|\vec{r}_{e_1}-\vec{r}_{e_2}|}-\frac{1}{|\vec{r}_{e_1}-\vec{r}_h|}-\frac{1}{|\vec{r}_{e_2}-\vec{r}_h|}\right) \tag{4.15}$$

is the direct Coulomb interaction in the absence of a dielectric mismatch and

$$\begin{aligned} W_{\rm ind,S}\left(\vec{r}_{e_1},\vec{r}_{e_2},\vec{r}_h\right) &= \frac{e^2}{4\pi^2\epsilon_1}\left(\frac{\epsilon_1}{\epsilon_2}-1\right)\sum_{m=-\infty}^{+\infty}\int_0^\infty {\rm d}k\mathbb{C}_m\left(kR,\frac{\epsilon_1}{\epsilon_2}\right) \\ &\quad\times\left[I_m^2(k\rho_{e_1})+I_m^2(k\rho_{e_2})+I_m^2(k\rho_h)\right], \end{aligned} \tag{4.16}$$

$$\begin{aligned} W_{\rm ind}\left(\vec{r}_{e_1},\vec{r}_{e_2},\vec{r}_h\right) &= -2\frac{e^2}{4\pi^2\epsilon_1}\left(\frac{\epsilon_1}{\epsilon_2}-1\right)\sum_{m=-\infty}^{+\infty}\int_0^\infty {\rm d}k\mathbb{C}_m\left(kR,\frac{\epsilon_1}{\epsilon_2}\right) \\ &\quad[\cos(kz_{h1})\cos(m(\theta_{e_1}-\theta_h))I_m(k\rho_{e_1})I_m(k\rho_h) \\ &\quad+\cos(kz_{h2})\cos(m(\theta_{e_2}-\theta_h))I_m(k\rho_{e_2})I_m(k\rho_h) \\ &\quad-\cos(k(z_{e_1}-z_{e_2}))\cos(m(\theta_{e_1}-\theta_{e_2})) \\ &\quad\times I_m(k\rho_{e_1})I_m(k\rho_{e_2})], \end{aligned} \tag{4.17}$$

are the modifications of this interaction due to the image charges induced by the difference in permittivity between the wire and its surrounding environment.

Similarly to the results in Chapter 3, these expressions clearly show the different contributions to the electrostatic energy $\delta W$ as illustrated by the labeled arrows in Fig. 4.1:

- three direct contributions (DC) of the regular Coulomb potential in $W_{\rm dir}$ (Eq. (4.15)) representing the Coulomb interaction between each of the particles;
- three self-energy contributions (SEC) $W_{\rm ind,S}$ emerging from the interaction between an induced image charge and the original charge (that produces the image);
- induced contributions (IC) $W_{\rm ind}$ emerging from the interaction between a charge in the wire and an induced image charge produced by another charge.

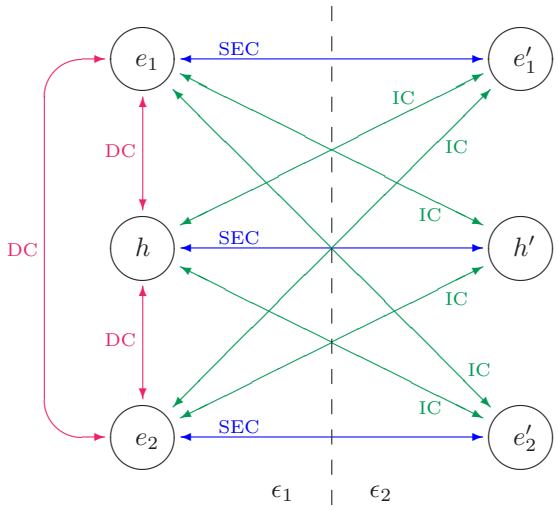


*Fig. 4.1* Schematical drawing of electrons ($e_1$ and $e_2$) and hole ($h$) near an interface with the indication of the different interactions between the electrons and hole and their images $e_1'$, $e_2'$ and $h'$.

The next step is to average the contributions $W_{\mathrm{dir}}$, $W_{\mathrm{ind,S}}$ and $W_{\mathrm{ind}}$ with the single particle radial wave functions in order to obtain the effective potential energies, resp. $U_{\mathrm{dir}}$, $E_{\mathrm{self}}$ and $U_{\mathrm{ind}}$. In previous chapters we obtained fits for all three contributions: The direct potential energy is given by Eq. (2.18), the induced potential can be found in Eq. (3.25) with its parameters in Eq. (3.28) and the self-energy is given by the fit in Eq. (3.29). Reusing these analytic expressions, we are able to construct the 2D effective trion potential:

$$\begin{aligned} U_{\mathrm{tot}} \quad = \quad & \tilde{U}_{\mathrm{dir}}\left(z_{h1}\right) + \tilde{U}_{\mathrm{dir}}\left(z_{h2}\right) - \tilde{U}_{\mathrm{dir}}\left(z_{h1} - z_{h2}\right) \\ & - \tilde{U}_{\mathrm{ind}}\left(z_{h1} - z_{h2}\right) + \tilde{U}_{\mathrm{ind}}\left(z_{h1}\right) + \tilde{U}_{\mathrm{ind}}\left(z_{h2}\right) + 3\frac{E_{\mathrm{self}}}{E_0'}. \end{aligned} \tag{4.18}$$

Three-dimensional and contour plots of the sum of direct and induced potentials for four different values of the dielectric mismatch are shown in Fig. 4.2. In this figure, we did not include the constant self-energy which is independent of $z_{h1}$ and $z_{h2}$, since this merely results in an increase of the bandgap without affecting the trion binding energy. In Fig. 4.2 we see that the potential exhibits a maximum for $z_{h1} = z_{h2}$, which corresponds to the configuration $z_{e_1} = z_{e_2}$ (for $X^-$) for which a strong repulsion between the two electrons is apparent. Lines of minima (attraction) are present in the potential energy for $z_{e_1} = z_h$ (i.e. $z_{h1} = 0$) and $z_{e_2} = z_h$ (i.e. $z_{h2} = 0$). As the dielectric mismatch is increased, the potential becomes slightly deformed: the larger the dielectric mismatch, the more pronounced are the minima and maxima.

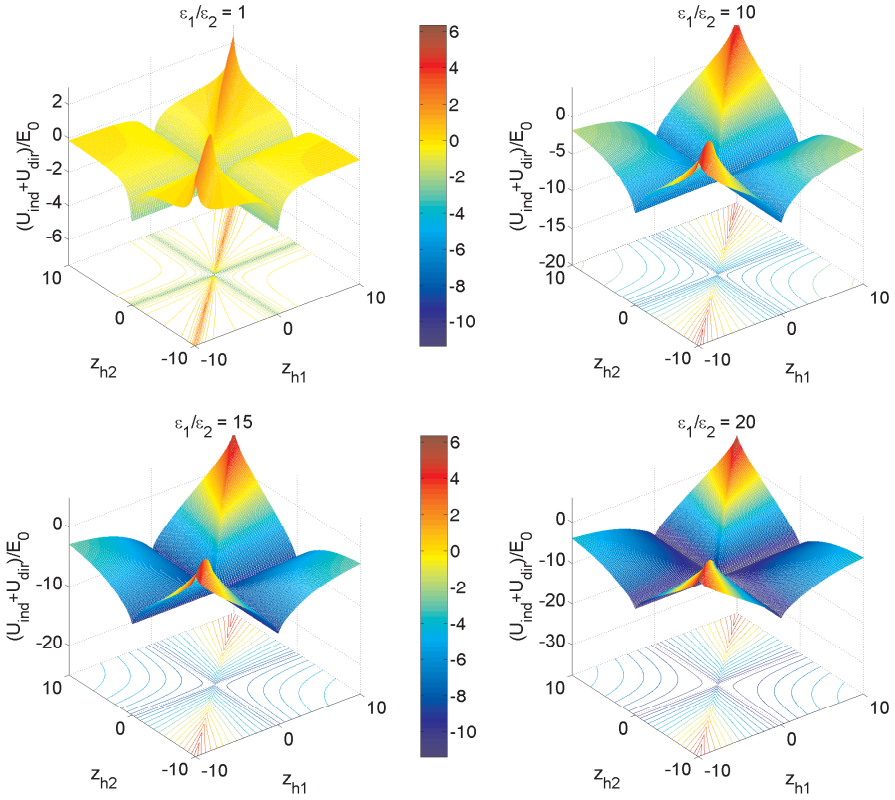


*Fig. 4.2* Three-dimensional and contour plots of the sum of induced and direct interaction potentials for $\epsilon_1/\epsilon_2 = 1, 10, 15, 20$. Note that the potential is plotted in units of $E_0 = e^2/4\pi\epsilon_1 R$.

## 4.4 TRION BINDING ENERGY AND WAVE FUNCTION

Next, we insert the effective 2D trion potential into the Schrödinger equation (Eq. (4.10)) and solve the latter on a 2D grid and obtain wave functions and energies. Introducing the wire radius $R$ as the unit of length and putting $a_{\mathrm{b},0} = 4\pi\epsilon_0\hbar^2/(m_e e^2)$, $E_0'' = e^2/(4\pi\epsilon_0 a_{\mathrm{b},0})$ and $E_0 = e^2/(4\pi\epsilon_1 R)$ we can rewrite Eq. (4.10) in a dimensionless form

$$H_-^{\mathrm{rel}} = \left(\frac{a_{\mathrm{b},0}}{R}\right)^2 \left[-\frac{1}{2\mu}\left(\frac{\partial^2}{\partial z_{h1}^2} + \frac{\partial^2}{\partial z_{h2}^2}\right) - \frac{1}{\sigma}\frac{\partial^2}{\partial z_{h1}\partial z_{h2}}\right] + \left(\frac{a_{\mathrm{b},0}}{R}\right)\frac{\epsilon_0}{\epsilon_1}\frac{U_{\mathrm{tot}}}{E_0}. \tag{4.19}$$

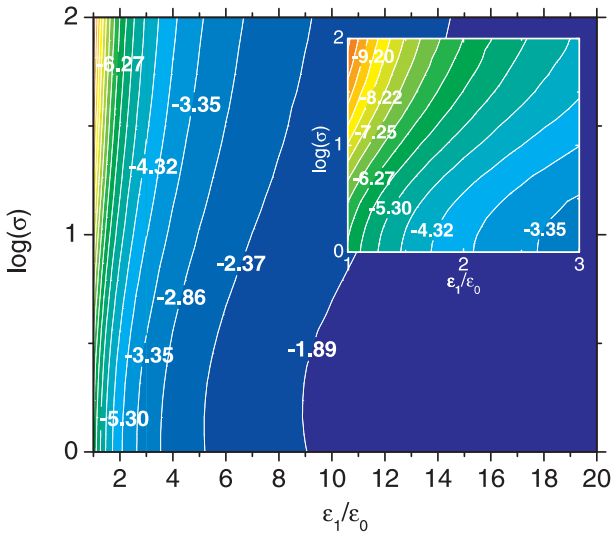


*Fig. 4.3* Contour plot of the $X^+$ ground state binding energy in units of $E_0''/1000 = \left[e^2/(4\pi\epsilon_0 a_{\mathrm{b},0})\right] \cdot [1/1000]$, as a function of the dielectric constant of the wire (with $\epsilon_2/\epsilon_0 = 1$) and the electron-hole mass ratio $\sigma$. The inset figure shows the same as the main figure, but now zoomed in to the region $1 \leq \epsilon_1/\epsilon_0 \leq 3$. The result is shown for $R/a_{\mathrm{b},0} = 20$.

*Table 4.1* Table with relevant material parameters for free-standing nanowires. For silicon we mentioned the transverse (t) and lateral (l) mass at the $X$-point, as well as the mass in the $\Gamma$ point. The value of $R/a_{b,0}$ in the last column was calculated for $R = 10$ nm.

| | $m_e$ $(m_0)$ | $m_{hh}$ $(m_0)$ | $\epsilon_1$ $(\epsilon_0)$ | $a_{b,0}$ (nm) | $E_0''$ (eV) | $\sigma$ | $R$ $(a_{b,0})$ |
|---|---|---|---|---|---|---|---|
| Si @ $X$ (t) | 0.1905 | 0.49 | 11.9 | 0.28 | 5.17 | 2.58 | 35.8 |
| Si @ $X$ (l) | 0.9163 | 0.49 | 11.9 | 0.06 | 24.86 | 0.53 | 172.7 |
| Si @ $\Gamma$ | 0.20 | 0.49 | 11.9 | 0.27 | 5.43 | 2.45 | 37.7 |
| InP | 0.0798 | 0.53 | 12.4 | 0.66 | 2.16 | 6.64 | 15.0 |
| ZnO | 0.24 | 0.78 | 8.1 | 0.22 | 6.51 | 3.25 | 45.2 |
| Ge | 0.082 | 0.28 | 16 | 0.65 | 2.22 | 3.41 | 15.5 |
| GaAs | 0.067 | 0.35 | 12.5 | 0.79 | 1.82 | 5.22 | 12.6 |
| InAs | 0.026 | 0.33 | 14.6 | 2.04 | 0.71 | 12.69 | 4.9 |

Similarly, we obtain for the positive trion the following Hamiltonian for the relative motion

$$H_+^{\mathrm{rel}} = \left(\frac{a_{\mathrm{b},0}}{R}\right)^2 \left[-\frac{1}{2\mu}\left(\frac{\partial^2}{\partial z_{h1}^2} + \frac{\partial^2}{\partial z_{h2}^2}\right) - \frac{\partial^2}{\partial z_{h1}\partial z_{h2}}\right] + \left(\frac{a_{\mathrm{b},0}}{R}\right)\frac{\epsilon_0}{\epsilon_1}\frac{U_{\mathrm{tot}}}{E_0}. \tag{4.20}$$

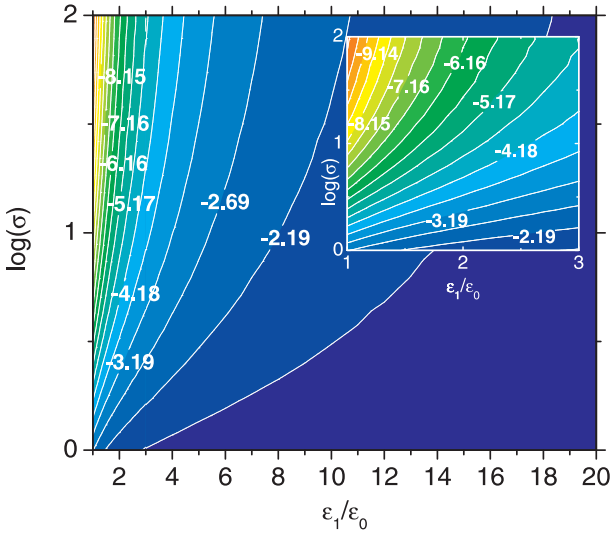


*Fig. 4.4* The same as Fig. 4.3 but now for the $X^+$ first excited state binding energy.

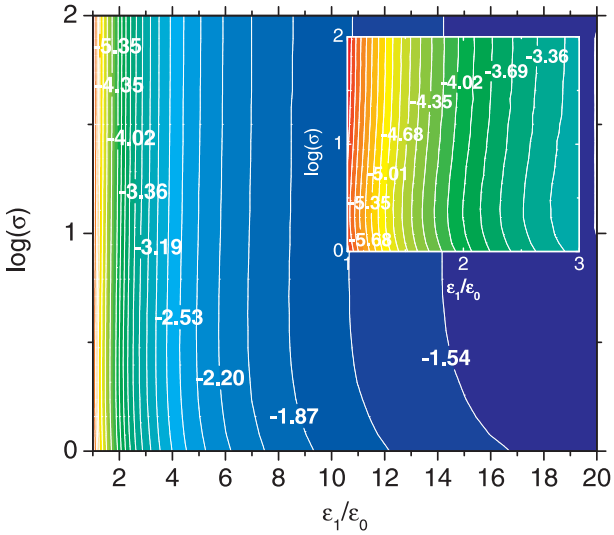


*Fig. 4.5* The same as Fig. 4.3 but now for the $X^-$ ground state binding energy.

The reference energies in both cases are the single particle energies, i.e. $E_{e_1} + E_{e_2} + E_h$ for $X^-$ and $E_{h_1} + E_{h_2} + E_e$ for $X^+$. Therefore, the lowest energy eigenvalues of Eqs. (4.19)-(4.20) correspond to the energy to break up the trion in three separate particles moving freely along the wire. However, our main interest is to determine the binding energy of the trion, i.e. the energy

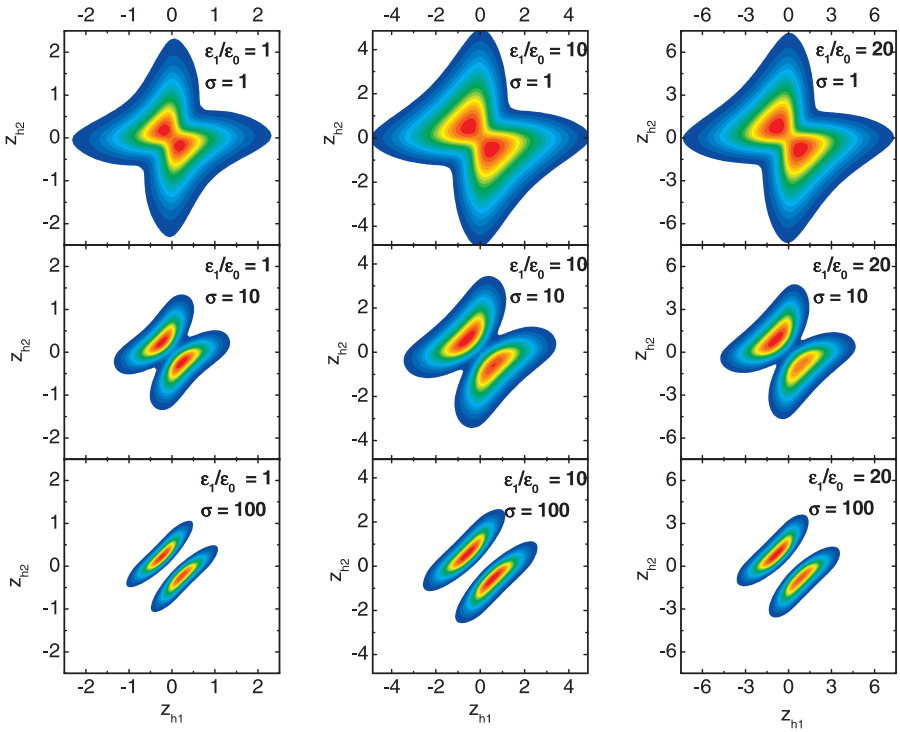


*Fig. 4.6* Plots of the $X^+$ ground state wave function for several values of $\sigma$ and $\epsilon_1/\epsilon_0$. The result is shown for $R/a_{\mathrm{b},0} = 20$.

needed to break up the trion into an exciton and one free particle:

$$E_B(X^{\pm}) = E(X^{\pm}) - E(X). \tag{4.21}$$

Please note that both $E(X^{\pm})$ and $E(X)$ are the many-particle energies as referred to the single-particle energy of their constituents. The exciton binding energy was obtained previously in Chapter 3. In Table 4.1 material parameters are given for a few materials [105, 106, 107].

Contour plots of the binding energy for free-standing wires ($\epsilon_2/\epsilon_0 = 1$) as a function of the dielectric constant of the wire $\epsilon_1/\epsilon_0$ for different values of $\sigma$ are shown in Figs. 4.3-4.4 for the positive trion $X^+$, where the binding energy values indicated at the contour lines are given in units of $E_0''/1000 = \left[e^2/(4\pi\epsilon_0 a_{\mathrm{b},0})\right]\cdot[1/1000]$. The energy of the ground state (Fig. 4.3) and the first excited state (Fig. 4.4) has been calculated. We can see that for a small fixed value of $\epsilon_1/\epsilon_0$ the ground state binding energy varies more rapidly with $\sigma$ than for a large fixed value of $\epsilon_1/\epsilon_0$. The picture for the first excited state is slightly different, but again most changes in the binding energy occur in the region of small dielectric constants. For the negative and less stable trion $X^-$ we only calculated the ground state binding energy in Fig. 4.5. The

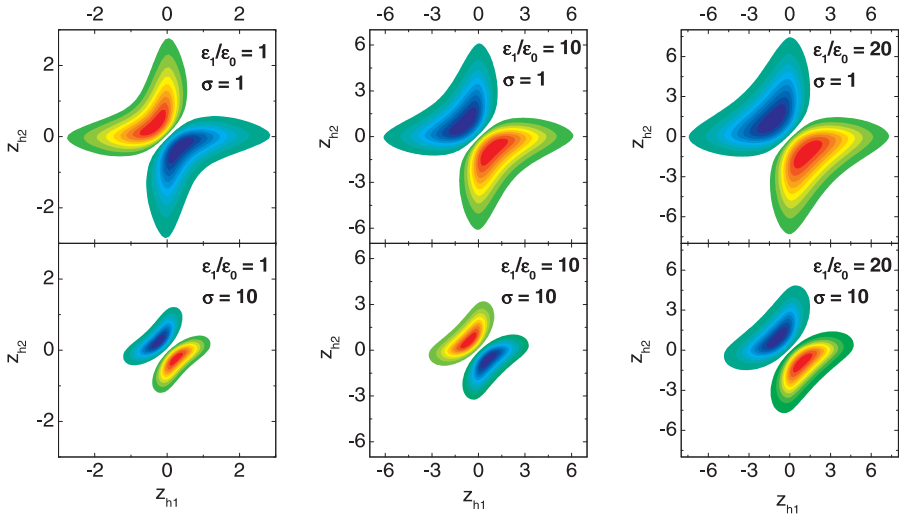


*Fig. 4.7* Plots of the $X^+$ first excited state wave function for several values of $\sigma$ and $\epsilon_1/\epsilon_0$. For larger values of $\sigma$, the wave function of the excited state will result in the same probability density as for the ground state: degeneracy sets in. The only difference is that for the excited state the wave functions are antisymmetric with respect to the interchange of holes, whereas for the ground state they are symmetric. The result is shown for $R/a_{\mathrm{b},0} = 20$.

fundamental difference with the positively charged trion is that now the contour lines are essentially parallel, which means that the $X^-$ binding energy is only weakly dependent on $\sigma$. As the dielectric constant $\epsilon_1/\epsilon_0$ is increased, the contour lines become slightly more bent, but the overall conclusion is clear: the parameter $\sigma$ does almost not affect the $X^-$ binding energy. In Figs. 4.6, 4.7 and 4.8 we show the wave functions for $X^+$ and $X^-$ for various values of $\sigma$ and $\epsilon_1/\epsilon_0$. In Fig. 4.6 we see the ground state wave function for the $X^+$ trion. It is clear that increasing $\sigma$ mainly changes the shape of the wave function: the maxima are pulled further away from each other and a node along the $z_{h1} = z_{h2}$ is created, the particles also become more localized. With increasing $\epsilon_1/\epsilon_0$, the extent of the wave function is changing (i.e. it increases with increasing $\epsilon_1/\epsilon_0$), while its shape is practically unaltered. With increasing $\sigma$ (i.e. increasing hole mass) the exciton wave function becomes more localized and the wave function condenses into two well-separated pockets. In Fig. 4.7 the excited state wave function of $X^+$ is plotted. It is clear that for $\sigma = 10$ the wave functions for the ground state and the excited state will result in a similar probability function and thus they result in (almost) degenerate values of the energy. For larger values of $\sigma$ ($\sigma \gtrsim 10$), the ground state and excited state become degenerate for $X^+$. Fig. 4.9 shows the energy difference in terms of percentage between both the ground and the excited state, the darkest blue zone representing the area where the difference is (almost) zero.

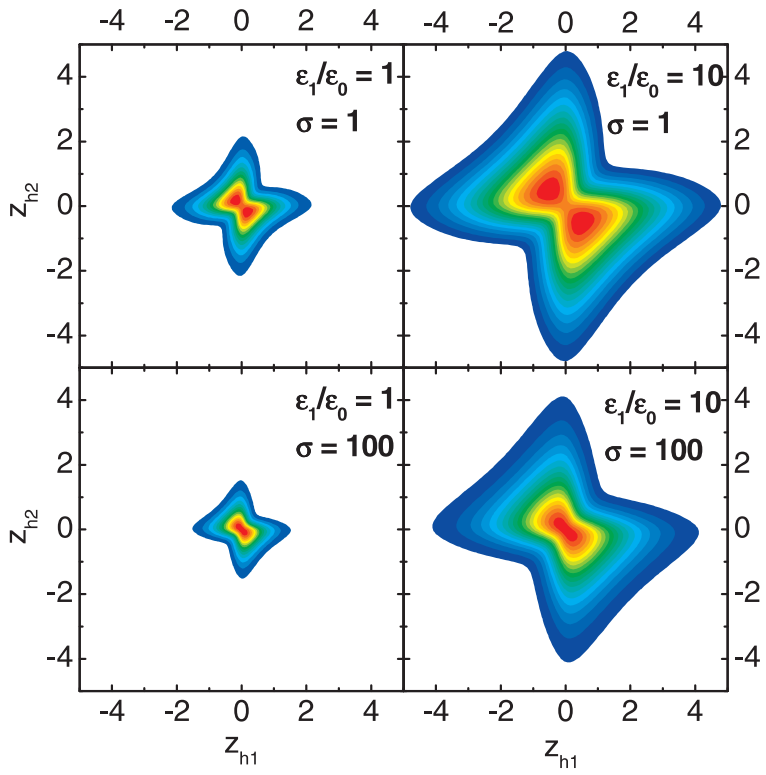


*Fig. 4.8* Plots of the ground state wave function for several values of $\sigma$ and $\epsilon_1/\epsilon_0$ for $X^-$. The result is again shown for $R/a_{\mathrm{b},0} = 20$ and $\epsilon_2/\epsilon_0 = 1$.

Fig. 4.8 shows several contour plots of the $X^-$ wave function. Notice again how a change in $\epsilon_1/\epsilon_0$ modifies the size of the wave function. As was to be expected from the energy contour plots, the wave function does not change significantly when $\sigma$ is increased. When increasing $\sigma$, the maxima are getting closer for the $X^-$ trion, whereas for the $X^+$ trion the maxima tend to separate: for the electrons in the $X^-$ trion it becomes more easy to tunnel through the barrier along the $z_{h1} = z_{h2}$ diagonal of the potential with increasing $\sigma$, while the opposite is true for the heavier holes.

The correlation between particles within the $X^\pm$ trions is reflected even more clearly in the pair correlation functions. The correlation functions can be expressed through:

$$f_{eh}(z) = \iint \mathrm{d}z_{h1}\mathrm{d}z_{h2}\,|\chi(z_{h1}, z_{h2})|^2\,\delta(z - z_{h1}), \tag{4.22}$$

for the electron-hole correlation and

$$f_{ee/hh}(z) = \iint \mathrm{d}z_{h1}\mathrm{d}z_{h2}\,|\chi(z_{h1}, z_{h2})|^2\,\delta\left(z - (z_{h1} - z_{h2})\right), \tag{4.23}$$

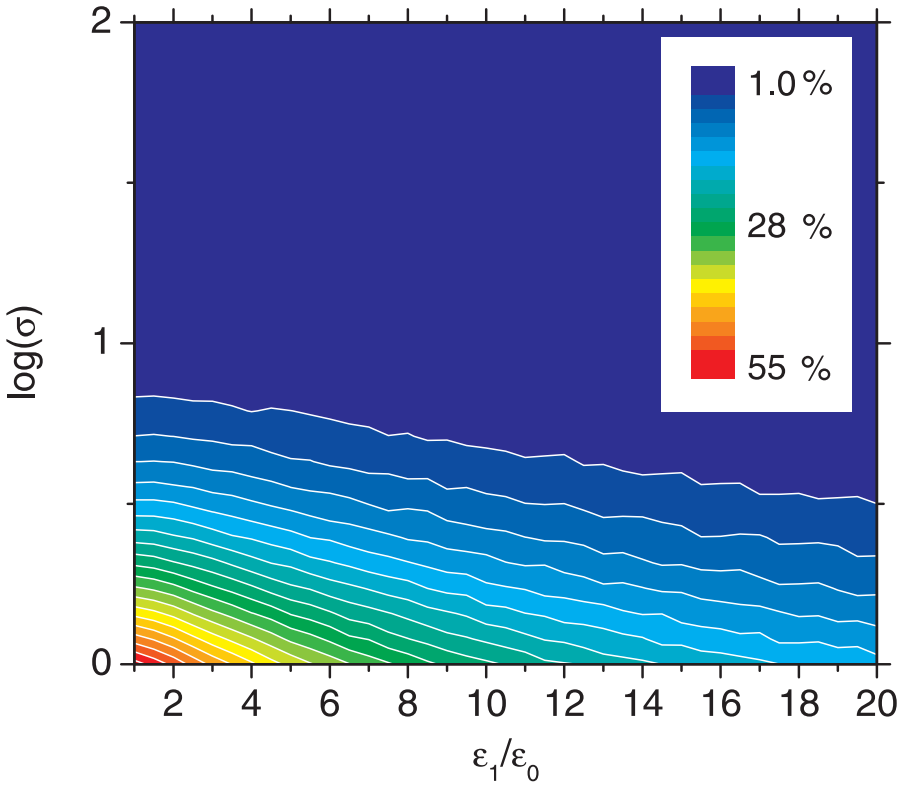


*Fig. 4.9* Plot of the energy difference in terms of percentage between the ground and excited state for the $X^+$ trion. The darkest blue zone represents the area where the energy is practically degenerate ($\epsilon_2/\epsilon_0 = 1$).

for the electron-electron or hole-hole correlation. The results are shown in Fig. 4.10. Notice that for the ground state: (i) the light electrons can still tunnel through the potential barrier for zero interparticle distance, whereas this is more difficult for the heavier holes, (ii) increasing $\sigma$ has the opposite effect on the positive and negative trion at zero interparticle distance, and (iii) the electron-hole correlation is the largest at zero interparticle distance, i.e. oppositely charged particles prefer to sit on top of each other. For the excited state correlation function, we find that (i) the $e-e$ and $h-h$ correlation functions exactly vanish for zero interparticle distance for both trions because of the asymmetry of the wave function at $z/R = 0$ and (ii) the $e-h$ correlation for the $X^+$ is larger than for the $X^-$ (it was vice-versa in the ground state): both particles are more bound to each other for the $X^+$ excited state than for the $X^-$ excited state. From Figs. 4.3, 4.4 and 4.5 we can also conclude that the ground state wave functions for both trions are symmetric with respect to the interchange of holes or electrons. Since the system consists of fermions, this

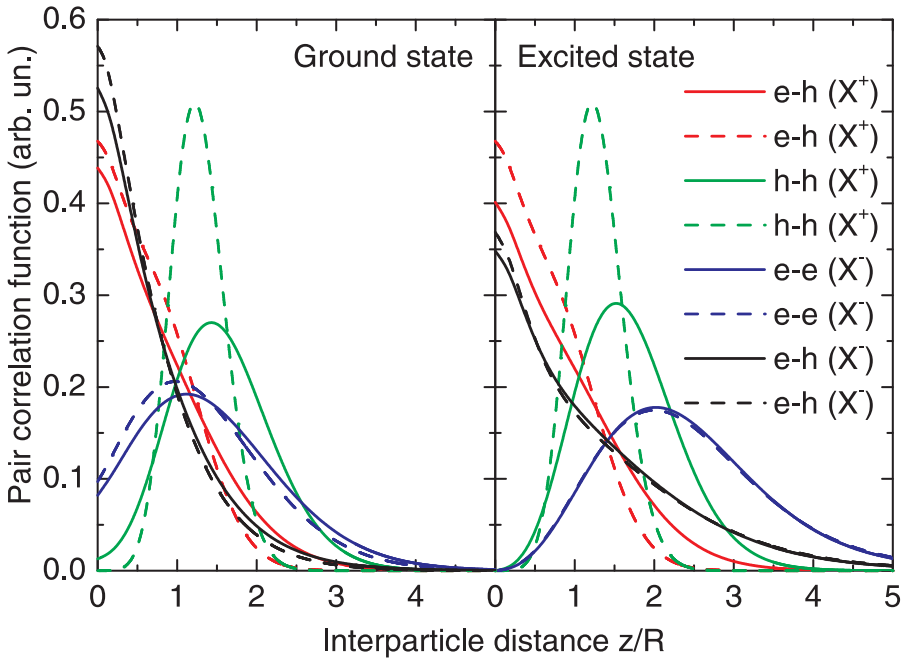


*Fig. 4.10* Ground state (left) and excited state (right) $X^+$ and $X^-$ pair correlation functions for electron-electron, hole-hole and electron-hole interaction for $\sigma = 5$ (full lines) and $\sigma = 50$ (dashed lines). The calculation was done for $R/a_{\mathrm{b},0} = 20$, $\epsilon_2/\epsilon_0 = 1$ and $\epsilon_1/\epsilon_0 = 10$.

means that the spin part of the total wave function must be antisymmetric and therefore the ground state wave functions are singlet states. The excited state wave functions however, are antisymmetric and correspond thus to triplet states in this case. From Ref. [108] we find that the trion singlet state consists of two different spin states, whereas the trion triplet consists of six different spin states. In the presence of a magnetic field the degeneracy of these states is lifted. Here, the trion spin-states are constructed by taking the orbital angular momentum for transverse motion $l = 0$ for all particles and are consequently 'bright' triplets. Triplet states with lower energy but with angular momentum different from zero may exist for thick wires. But as these triplet states are 'dark' states, thus optically inactive, we did not consider them here.

Furthermore, we also plotted the conditional probability as a function of several electron and hole positions for $X^{\pm}$. This probability is given by $|\Psi|^2$ where two particles out of the three are fixed in space. In Fig. 4.11(a) we placed for the $X^+$ trion an electron in the origin and a hole at a distance which corresponds to the average electron-hole distance in the $X^+$. Note that the hole is most likely to be found near the electron, i.e. it is drawn to the electron but on the other hand it is also repelled by the other hole. When the

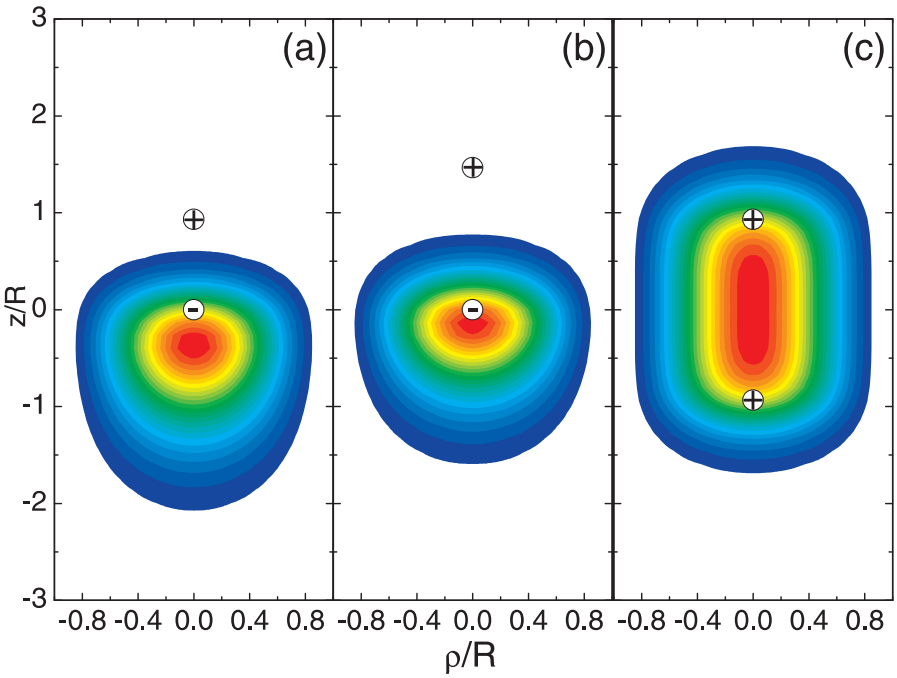


*Fig. 4.11* (a) and (b) $X^+$ conditional probability plots for an electron fixed at $z/R = 0$ and one of the holes fixed at two different positions. (c) Both holes are fixed. The highest probability to find the remaining particle corresponds to the red areas. These plots were made for $R/a_{\mathrm{b},0} = 20$, $\epsilon_2/\epsilon_0 = 1$ $\epsilon_1/\epsilon_0 = 10$ and $\sigma = 5$.

electron-hole distance increases (Fig. 4.11(b)), the hole is able to get closer to the electron. From Fig. 4.11(c) it is clear that the electron can be found, with equal probability, in the vicinity of one of the holes, the probability function is symmetric with respect to the origin. Figs. 4.12(a-c) show similar pictures for the $X^-$ as for the $X^+$ trion. Notice that the electron cloud is much more spread out as a consequence of the lighter electron mass. Similarly, the hole cloud is more concentrated between the two electrons.

From Table 4.1 it is clear that our main focus is on the $1 \leq \sigma \leq 10$ interval and therefore we plotted in Fig. 4.13 the singlet and triplet binding energy for this interval for $\epsilon_1/\epsilon_0 = 5, 10$ and 15 and $R/a_{b,0} = 20$. As it should be, the binding energies are identical for both positive and negative trions when $\sigma = 1$. When $\sigma$ increases, we see that: (i) the ground state binding energy for the $X^-$ trion is quasi constant and the ground state for the $X^+$ trion becomes clearly more stable for all values of $\epsilon_1/\epsilon_0$; (ii) the binding energy of the first excited state of $X^-$ decreases with increasing $\sigma$, whereas its ground state energy stays quasi constant; and (iii) the first excited state of the $X^+$

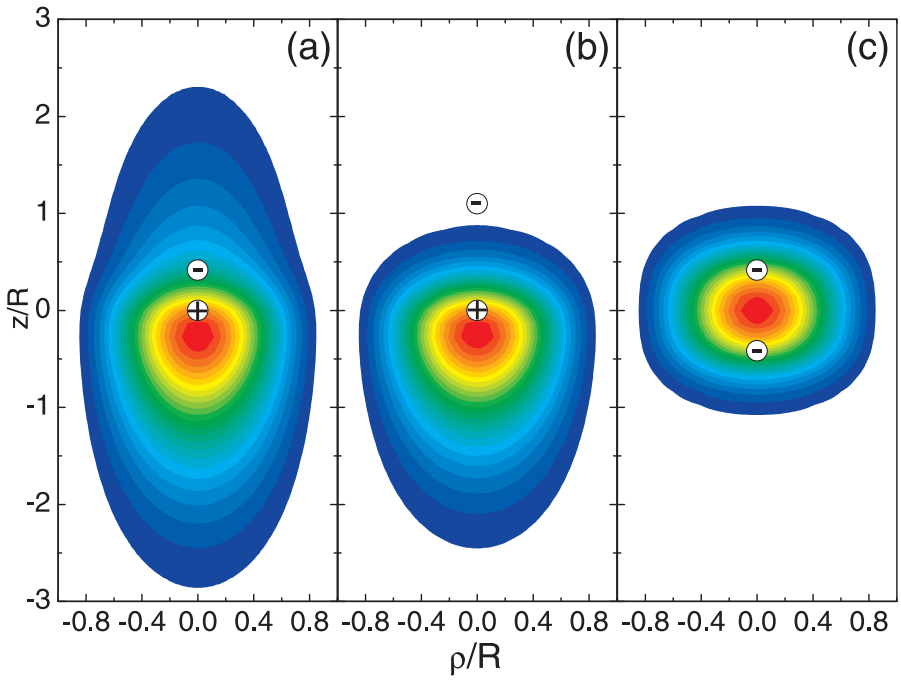


*Fig. 4.12* (a) and (b) $X^-$ conditional probability plots for a hole fixed at $z/R = 0$ and one of the electrons fixed at two different positions. (c) Both electrons are fixed. The highest probability to find the remaining particle corresponds to the red areas. These plots were made for $R/a_{\mathrm{b},0} = 20$, $\epsilon_1/\epsilon_0 = 10$ and $\sigma = 5$.

comes close to degeneracy with its ground state and becomes more stable than the $X^-$ ground state for $\sigma$ between 3 and 4.

Finally, we calculated the singlet and triplet $X^+$ and $X^-$ trion binding energy as function of the radius $R/a_{b,0}$. This is shown in Fig. 4.14 for $\sigma = 0.53$ which is valid for thicker Si wires (wires where the bandgap is indirect we take the mass of the electron at the $X$-point, in this case we choose the lateral mass), and $\sigma = 2.45$, valid for thin wires where the bandgap becomes direct and we can use the mass of the electron at the $\Gamma$-point (for this mass, the transverse mass at the $X$-point would result in almost exactly the same curve due to the very small difference in $\sigma$). It is clear from Fig. 4.14 that a small difference in the value of $\sigma$ results in small differences in the behavior as function of the wire radius. For the chosen parameters the triplet state or excited state is always less bound than the singlet state or ground state. We found that, to a good approximation (within 1 %), the $X^-$ and $X^+$ singlet binding energies could be fitted to $-c/(R/a_{b,0})^d$. The values of the fitting parameters $c$ and $d$ for the singlet binding energies for several materials are

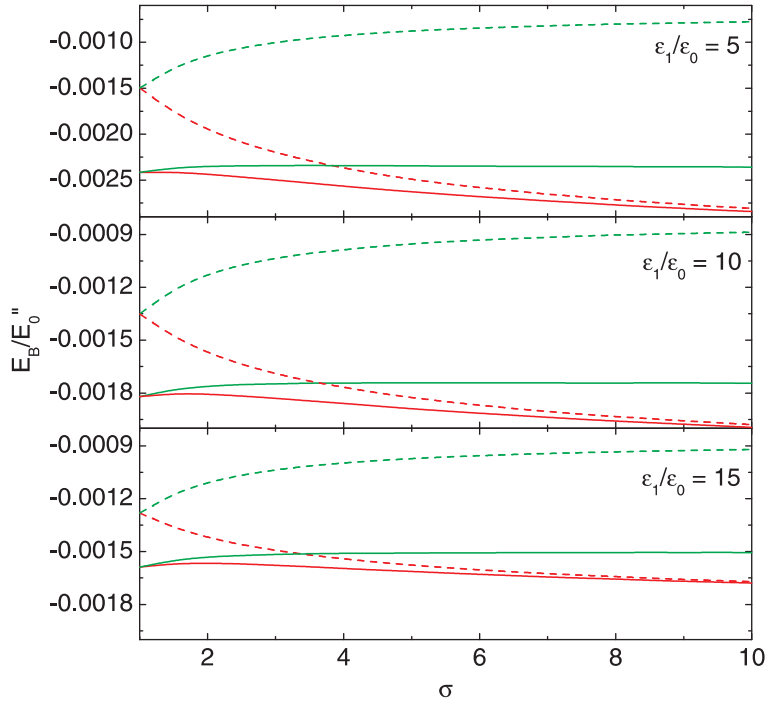


*Fig. 4.13* Singlet (full lines) and triplet (dashed lines) $X^+$ (red) and $X^-$ (green) trion binding energies as function of $\sigma = m_h/m_e$ for $\epsilon_1/\epsilon_0 = 5, 10$ and 15 and fixed $R/a_{b,0} = 20$, $\epsilon_2/\epsilon_0 = 1$.

given in Table 4.2. The triplet binding energies can be fitted to the same formula but, of course, with different parameters.

## 4.5 CONCLUSION

In this chapter we studied the stability of positively and negatively charged excitons in wires with different dielectric constants. Thanks to our previous work on excitons, we were able to quickly and accurately reconstruct the effective 2D potential for trions, which enables the calculation of trion binding energies on a 2D grid. We found that the negatively charged exciton has always a smaller binding energy than the positively charged exciton in a wire with $\sigma > 1$, even when the dielectric mismatch is larger. In the case of $\sigma < 1$ the opposite is true. This is in contrast to the embedded V-grooved wires [109] where it was found experimentally that for narrow widths $|E_B(X^-)| > |E_B(X^+)|$. Furthermore, we found that the dielectric mismatch does not change the qualitative behavior of the $\sigma$-dependence of the binding

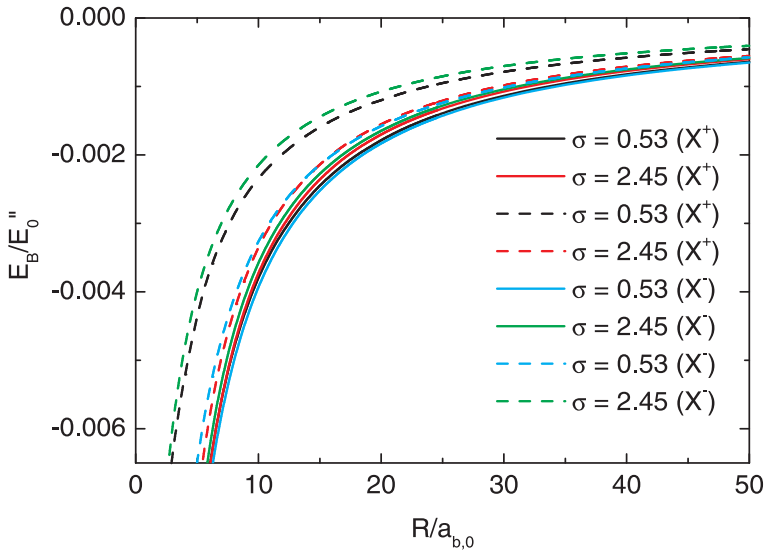


*Fig. 4.14* Trion singlet (full lines) and triplet (dashed lines) binding energy as function of the wire radius $R/a_{b,0}$ for $\epsilon_1/\epsilon_0 = 11.9$. We took $\sigma = 0.53$ (Si @ $X$) and $\sigma = 2.45$ (Si @ $\Gamma$).

*Table 4.2* Table with fitting parameters for the $X^{\pm}$ singlet binding energy using the formula $-c/(R/a_{b,0})^d$.

| | $X^+$ | | $X^-$ | |
|---|---|---|---|---|
| | $c$ | $d$ | $c$ | $d$ |
| Si @ $X$ (t) | 0.0465 | 1.100 | 0.0431 | 1.086 |
| Si @ $X$ (l) | 0.0422 | 1.052 | 0.0448 | 1.064 |
| Si @ $\Gamma$ | 0.0462 | 1.098 | 0.0430 | 1.085 |
| InP | 0.0520 | 1.126 | 0.0433 | 1.095 |
| ZnO | 0.0540 | 1.096 | 0.0485 | 1.079 |
| Ge | 0.0440 | 1.112 | 0.0397 | 1.093 |
| GaAs | 0.0501 | 1.120 | 0.0430 | 1.093 |
| InAs | 0.0536 | 1.144 | 0.0416 | 1.101 |

energy for the $X^-$ trion, whereas the curves for the $X^+$ singlet state show a smaller $\sigma$-dependence with increasing $\epsilon_1/\epsilon_0$. We also studied the trion wave functions and discussed both correlation functions and conditional probabilities of the trions. These results show us the correlated arrangement of the particles in the wire. The binding energies as function of the wire radius exhibit, to a good approximation, a $1/R$ dependence.

### Publications

The results in this chapter were published as:

- A.F. Slachmuylders, B. Partoens, W. Magnus, and F.M. Peeters, *Trions in cylindrical nanowires with dielectric mismatch effects*, Phys. Rev. B **76**, 075405 (2007).
- The paper Phys. Rev. B **76**, 075405 (2007) was also selected to appear in the Virtual Journal of Nanoscale Science and Technology, August 20 edition (2007).
- A.F. Slachmuylders, B. Partoens, W. Magnus, and F.M. Peeters, *Excitons and trions in cylindrical nanowires with dielectric mismatch*, Phys. Stat. Sol. (c) **5**, 2416 (2008).
- A.F. Slachmuylders, B. Partoens, W. Magnus, and F.M. Peeters, *The effect of dielectric mismatch on excitons and trions in cylindrical semiconductor nanowires*, to appear in Journal of Computational Electronics.
- A.F. Slachmuylders, B. Partoens, W. Magnus, and F.M. Peeters, *The effect of the dielectric mismatch on excitons and trions in freestanding nanowires*, Phys. E **40**, 2166 (2008).

# 5

# *Effect of a metallic gate on the energy levels of a shallow donor*

## 5.1 INTRODUCTION

The study of shallow donor impurities near an interface has gained renewed interest in view of the perspective towards atomic scale electronics. On one hand, a very promising application aims at the realization of a qubit exploiting shallow donor states as was initially proposed by Kane [20, 21] for a P dopant in Si. To manipulate (read out) the qubit one proposes the use of a metallic gate to control the position of the electron [110]. On the other hand, controlling donor states is equally important to pursue the miniaturization of nanodevices e.g. transistors having only a few dopants in their conduction channel. Recently, H. Sellier *et al.* [19] have studied the effect of an impurity on the electrical transport in a semiconductor nanowire. As three-dimensional (3D) atomical control of the dopant position has already been realized [16], a better understanding of the physics of single dopants is highly desirable to anticipate future applications in nanoelectronics. In the first part of this chapter we study the energy levels of a single dopant, which provide useful information for transport experiments. The obtained energy levels indicate where tunneling through the donor site can occur, since tunneling is invoked when the applied gate voltage causes the dopant energy level to match with the Fermi level in source and drain. In the second part of the paper, we investigate how the electric field can be used to tune the electron position between the donor site and the interface.

In previous theoretical work [110, 111, 112, 113], the properties of a donor placed near a thick insulating interface were studied. In this constellation the

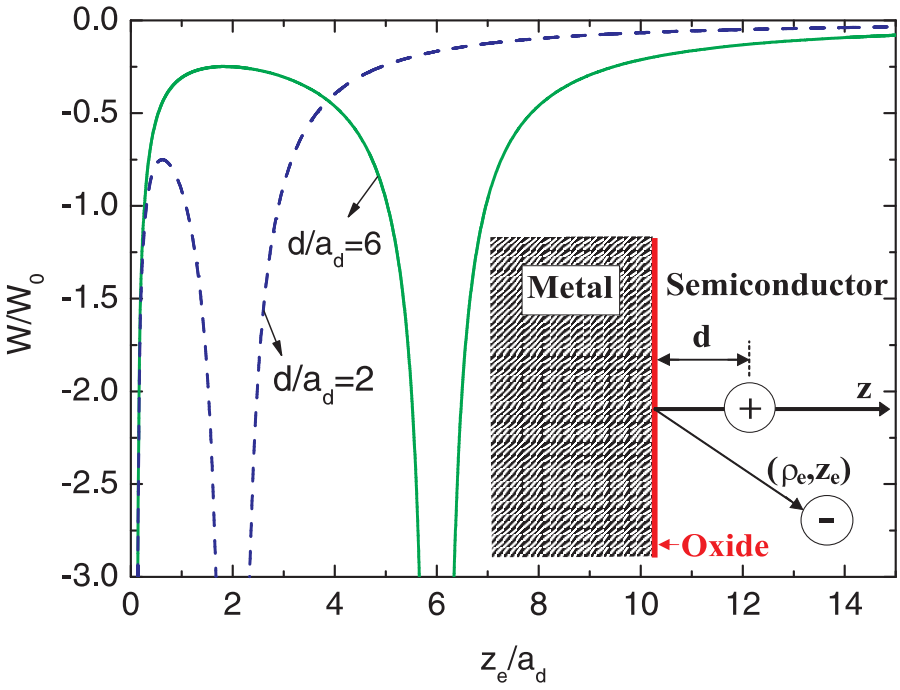


*Fig. 5.1* Plot of the potential energy along the $z$-axis ($\rho_e = 0$) for two different impurity positions. Note that $W_0 = e^2/(4\pi\epsilon_1 a_d)$ and $a_d = 4\pi\epsilon_1\hbar^2/(m_\perp e^2)$. Inset: schematical representation of the studied system.

dielectric mismatch (e.g. $\epsilon_{\rm Si} = 11.9$ and $\epsilon_{\rm SiO_2} = 3.4$) leads to an enhancement of the Coulomb interaction. The gate was assumed to be sufficiently far away from the interface to prevent screening while merely providing an electric field to drive the electron away from the impurity. Here, we consider the opposite case of a very thin oxide layer separating the metallic gate from the semiconductor (see inset Fig. 5.1). We have chosen to model the system by assuming that the oxide layer negligibly contributes to the dielectric mismatch and only prevents the electron from leaving the semiconductor.

We consider a donor located at a distance $d$ from a semiconductor/insulator /metal interface. As was mentioned previously, we assume that the thickness of the insulator is negligibly small. Moreover its potential barrier is considered infinitely high so as to confine the electron to the semiconductor region. Due to dielectric mismatch effects – the permittivity $\epsilon_1$ at the semiconductor side of the interface is typically of the order of 10, while the permittivity $\epsilon_2$ of the metallic gate is infinite – image charges will arise that screen the interaction potential between the impurity and the electron.

## 5.2 THEORY: POTENTIAL ENERGY AND HAMILTONIAN

The potential energy $W$ between an electron and an impurity near the semiconductor/metal interface at position $\vec{r}_h = (0, d)$ is given by [114]

$$W(\vec{r}_e, \vec{r}_h) = \frac{e^2}{4\pi\epsilon_1}\left[-\frac{1}{4z_e} - \frac{1}{\sqrt{\rho_e^2 + (z_e - d)^2}} + \frac{1}{\sqrt{\rho_e^2 + (z_e + d)^2}}\right], \tag{5.1}$$

with $\rho = \sqrt{x^2 + y^2}$. The first term arises from the interaction between the electron and its image, the second term is due to the normal electron-impurity interaction, whereas the last term represents the interaction between a particle (electron or impurity) and the image of the other particle (impurity image or electron image). The impurity-impurity image interaction is removed, since it only adds a constant to the bandgap. The potential energy profile exhibits a double well structure (see Fig. 5.1, where $W$ is plotted for two impurity positions $d/a_d$, with $a_d = (4\pi\epsilon_1\hbar^2)/(m_\perp e^2)$ the donor Bohr radius, $m_\perp$ the transverse effective mass and $W_0 = e/(4\pi\epsilon_1 a_d)$. When the impurity moves towards the interface, the potential wells start to interact strongly and eventually combines into a single well. Exploiting the cylinder symmetry of the problem, we may write the dimensionless Hamiltonian of the system as [111]

$$H = -\frac{1}{2}\left[\frac{\partial^2}{\partial\rho_e^2} + \frac{1}{\rho_e}\frac{\partial}{\partial\rho_e} - \frac{m^2}{\rho_e^2} + \gamma\frac{\partial^2}{\partial z_e^2}\right] + \left[-\frac{1}{4z_e} - \frac{1}{\sqrt{\rho_e^2+(z_e-d)^2}} + \frac{1}{\sqrt{\rho_e^2+(z_e+d)^2}}\right] + \tilde{F}z_e, \tag{5.2}$$

where $\gamma = m_\perp/m_\parallel$ is the ratio between the transverse and longitudinal effective masses (for simplicity, we took $\gamma = 1$ in our calculations). Because of the cylindrical symmetry we have $\Psi_e = e^{im\theta_e}\psi(\rho_e, z_e)$. We introduced the donor Bohr radius $a_d$ as the unit of length and twice the Rydberg energy, $E_{2Ry} = \hbar^2/(m_\perp a_d^2)$ as the unit of energy. $\tilde{F} = F/F_0$ where $F$ is a uniform electric field and $F_0 = E_{2Ry}/(ea_d)$. For Si, the atomic units are $a_d = 3.31$ nm, $E_{2Ry} = 36.5$ meV and $F_0 = 110$ kV/cm whereas for GaAs we find $a_d = 9.89$ nm, $E_{2Ry} = 11.6$ meV and $F_0 = 12$ kV/cm. Notice that the Hamiltonian given in Eq. (5.2) corresponds to a (scaled) hydrogen model for large values of $d/a_d$.

## 5.3 DONOR ENERGY LEVELS

Using finite element techniques, we obtained a numerically exact solution to the effective 2D Schrödinger equation. The resulting energy levels for

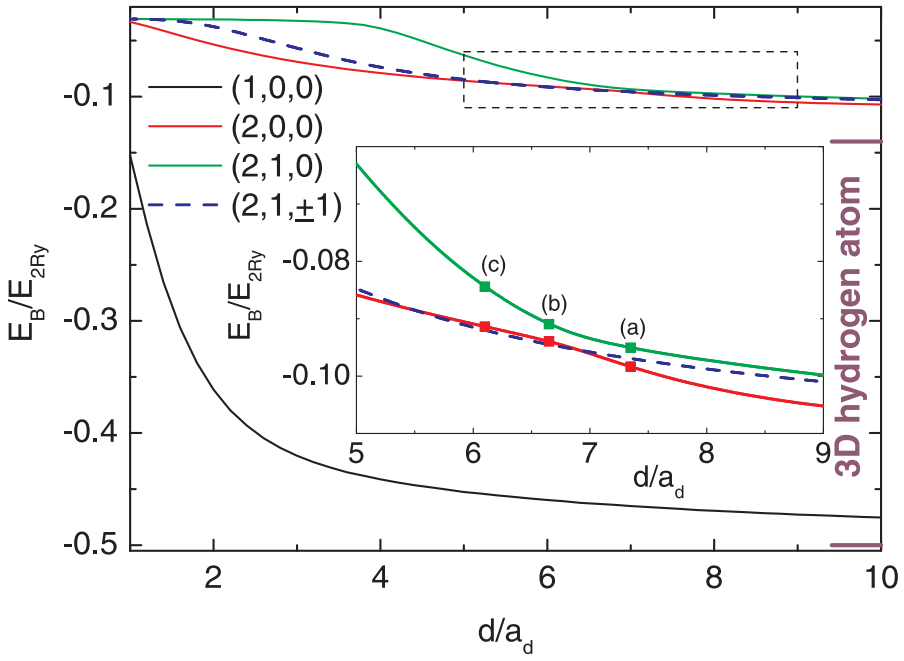


*Fig. 5.2* Energy spectrum versus the donor position $d/a_d$ w.r.t. the metallic interface. The values for the 3D hydrogen atom are indicated at the right of the figure. Inset: box region indicated by the dotted curves in the main figure.

$F/F_0 = 0$ are shown in Fig. 5.2 where we labeled the energy levels with $n$, $l$ and $m$. Due to cylindrical symmetry, only $m$, the quantum number of the angular momentum operator $L_z$, is conserved in contrast to $n$ and $l$, the quantum numbers of the hydrogen spectrum, emerging for $d/a_d \to \infty$. The energy levels of the latter are $E_n = \hbar^2/(2m_\perp a_d^2 n^2)$. A remarkable anti-crossing between the $(n,l,m)$= (2,0,0) and (2,1,0) energy levels (levels of equal $m$ and originating from different $l$ quantum number) is observed for $d/a_d \approx 6.6$. The surrounding region is enlarged in the inset of Fig. 5.2 where it is seen clearly that both levels fail to interact with the (2,1,1) level, due to a different quantum number $m$. Similar observations can be made for other parts of the spectrum. Near the anti-crossing point, the probability densities (see Fig. 5.3) undergo drastic changes: the probability density of the (2,0,0) level exhibits a secondary extremum first underneath, then around and finally above the primary extremum with decreasing $d/a_d$. As $d/a_d$ decreases, the (2,1,0) probability density shows an increase in size of the bottom lobe, which explains the energy increase since the corresponding $p_z$-like orbital piles up against the interface. We did not plot the probability density of the (2,1,1) state, since it does not interact with any other state and no significant changes in the shape of the wave function are found. It should be noted that we

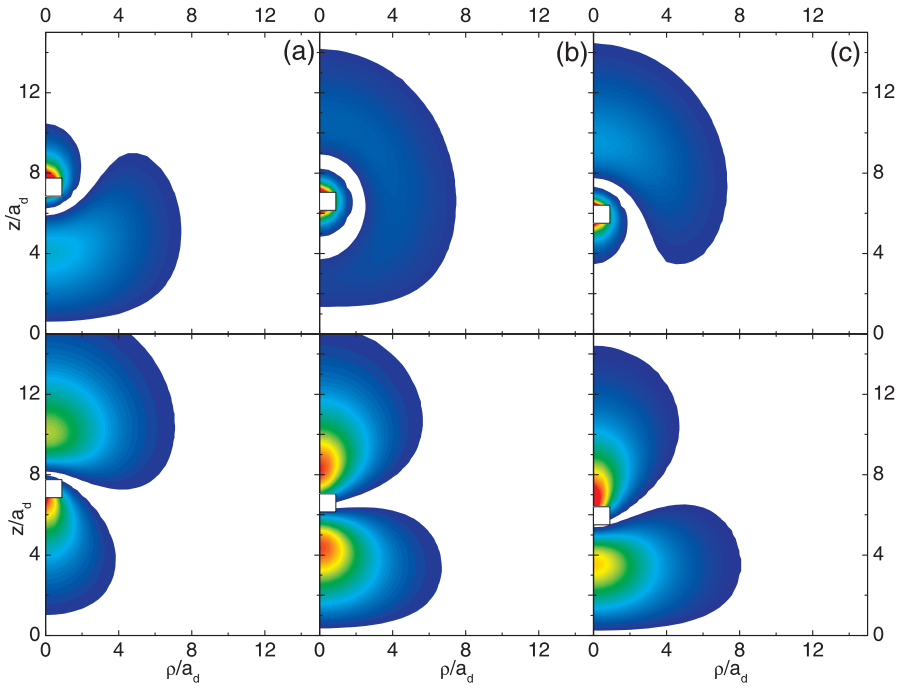


*Fig. 5.3* Probability density in (a), (b) and (c) as indicated in the inset of Fig. 5.2 as function of the distance $d/a_d$ from the metallic interface. The top three figures correspond to the densities of the (2,0,0) energy level, whereas the three figures at the bottom correspond to the (2,1,0) energy level. The donor position is indicated by the white square. Blue (red) areas represent low (high) probabilities. The white area represents zero probability.

did not find any anticrossing behavior of the ground state energy level as a function of the donor position without an electric field. In Ref. [115], it was shown that the character of the ground state changes at a certain value of the electric field: the *s*-like ground state becomes *p*-like.

## 5.4 INFLUENCE OF AN ELECTRIC FIELD

Next, we investigated the possibility of using an electric field to influence the position of the electron. For quantum computing purposes such an electric field can be used to move the electron back and forth between the donor site and the interface. From Fig. 5.4 it is clear that an increasing field pushes the electron closer to the interface for all donor positions. For larger values of $d/a_d$ (e.g. $d/a_d = 10$) a weak electric field is already sufficient to considerably enlarge the distance from the donor position; indeed for $d/a_d = 10$ an electric

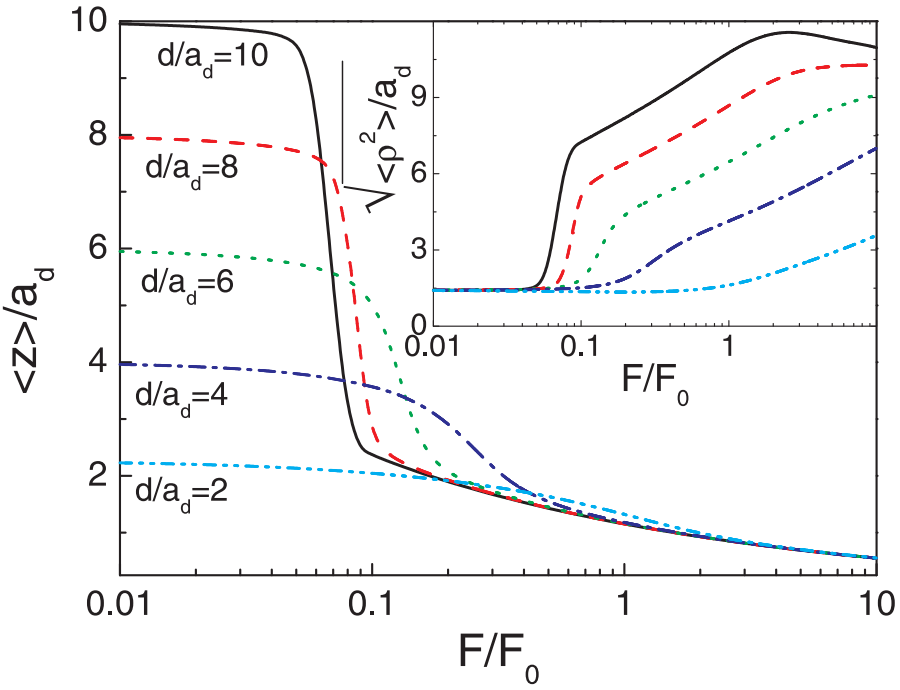


*Fig. 5.4* Expectation value of the electron position along the $z$-axis, $\langle z\rangle/a_d$, as a function of the electric field for different impurity positions. Inset: expectation value of the electron wave function extending along the $(x, y)$-plane, $\sqrt{\langle\rho^2\rangle}/a_d$, as a function of the electric field for different impurity positions.

field of $F/F_0 \cong 0.07$ is sufficient to ionize the donor in an abrupt way. The transition is less abrupt when the donor is located closer to the interface, which is illustrated for $d/a_d = 4$ and $d/a_d = 2$: the donor is ionized slowly and a much larger electric field is required to pull the electron away from the donor site. These two different regimes of response of the system to an applied electric field was also obtained in Ref. [116] and Ref. [117], where the system was modeled without image charges. Both the adiabatic (slow ionization of the donor) and tunneling (sudden ionization) regime can be observed in our model.

Also, it should be noted that for an efficient manipulation of the electron states in a real quantum device it is compulsory that switching the electron between the interface and the donor site be completely reversible. Therefore, the electron state near the interface should remain laterally bound to its donor site. From the inset in Fig. 5.4 we notice that while an increasing electric field drags the electron towards the interface, the lateral localization of the electron wave function is found to deteriorate. However, since the electric field $F/F_0 = 10$ is rather large as compared to what is used in a typical experiment,

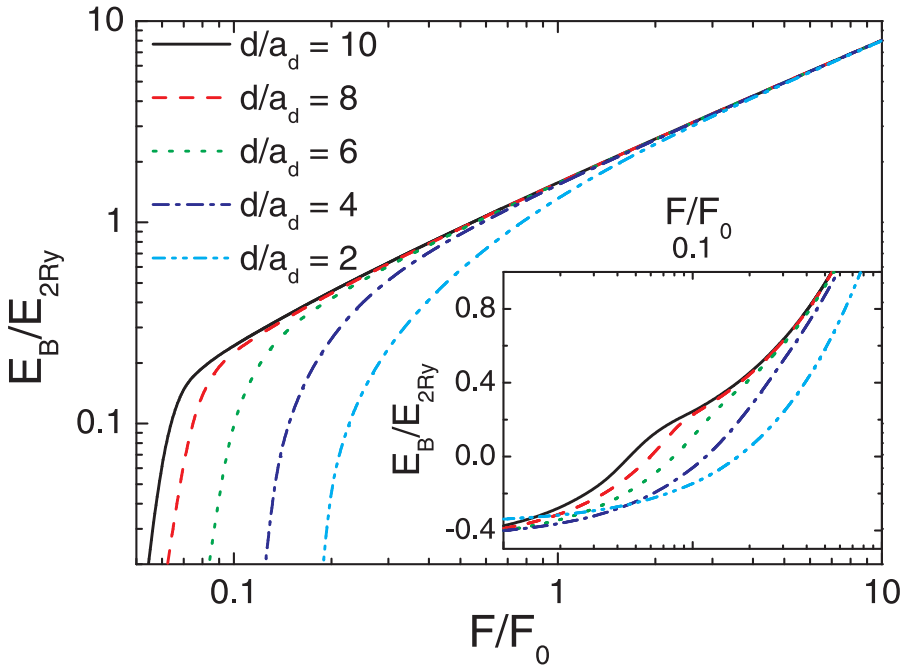


*Fig. 5.5* Log-log plot of the ground state energy levels for $m = 0$ as a function of the electric field for different impurity positions. Inset: same but now with a linear scale for the energy.

we may conclude that the electron stays sufficiently localized at the interface in the range of experimentally relevant electric fields.

Finally, the ground state energy was calculated as a function of the electric field for different donor positions. Fig. 5.5 shows that for very large electric fields the energies are independent of the donor position, i.e. the electric field is strong enough to pull away the electron from the impurity site for any value of $d/a_d$. Also note that a sudden ionization is clearly reflected in the electron energy spectrum (see Fig. 5.5).

## 5.5 CONCLUSION

To conclude, in this chapter we investigated the energy levels of an impurity near a metallic interface. We calculated the energy levels of the impurity as a function of the donor position and compared them with the bulk values to demonstrate the effect of the metallic interface on the energy levels that may also carry source-to-drain tunneling currents in nanoscale transistors. In view of potential quantum computing applications, we have studied the effect of

an electric field moving the electron away from the donor site to the interface. An acceptable degree of lateral localization of the electron at the interface can be kept at experimentally relevant fields to switch between the donor site and the metallic interface. This conclusion is also supported by the electric field dependence of the energy spectrum: only at very large electric fields, the energy spectrum is dominated by the electric field strength and not by the characteristic of the sample, e.g. the donor position. Ionization is found to occur adiabatically when the donor resides close to the interface, whereas it occurs suddenly for large distances from the interface. In the range of experimentally relevant electric fields, the donor position clearly affects the donor energy levels and the effect of a sudden ionization can be seen.

**Publications**

The results in this chapter were published as:

- A.F. Slachmuylders, B. Partoens, W. Magnus, and F.M. Peeters, *Effect of a metallic gate on the energy levels of a shallow donor*, Appl. Phys. Lett. **92**, 083104 (2008).

# 6

# Summary

In this thesis, exciton and impurity properties of semiconductor nanowires and related systems have been investigated theoretically. Valuable information about specific characteristics is obtained by determining the excitonic properties in these low-dimensional systems. Since NWs exist in a wide variety of materials and sizes, I tried to keep most calculations in this thesis as general as possible, allowing a very large "window" of applicability of the presented results. The main focus of this work was obtaining the characteristics for the exciton and exciton complexes in NWs. Additionally, impurity effects near a metallic interface were investigated, which is relevant for NWs and other applications such as the development of quantum computers.

In the **first chapter**, the introduction to this work was presented. I discussed several methods to grow wires, and some of the applications that have been realized over the last few years, in order to give an idea of the huge potential of NWs and related systems. NW applications often reveal superior qualities over other existing devices and therefore a bright future for NWs has been predicted by many researchers. After discussing its applications, I turn to a more theoretical part, where an introduction to solid state physics was given, together with the explanation of some basic concepts, such as excitons and related complexes.

The excitonic properties were first treated in **chapter two** in the most simple case, i.e. without any dielectric mismatch effects. In this chapter I calculated the effective interaction potential and the exciton binding energy. The effective interaction potential was calculated for different states of the electron and hole and we were able to present 'exact' numerical results. In order to reduce the computational burden for future calculations, these results

were used to be fitted to three analytical approximate expressions. A first Padé approximation gives the correct qualitative behaviour, but the fit was not optimal. Nevertheless this expression was useful to perform further analytical calculations to estimate the binding energy of the exciton, especially for small values of the wire radius $R$. A second Padé approximation as well as the result from the parabolic confinement gave rise to very good fits. Furthermore the exciton binding energy was calculated both semi-analytically and numerically and analytical approximations were given. I also investigated the influence of a magnetic field and determined an analytical expression for the effective potential for arbitrary magnetic field strengths. Finally I calculated the binding energy as a function of the magnetic field, where I found that the ground state binding energy is mostly affected by a variation of the magnetic field.

I took the dielectric mismatch into account in the **third chapter**. The interaction potential becomes significantly more complicated and has been studied in detail in this chapter. Again, I proposed an appropriate analytical formula for the effective exciton potential in a semiconductor quantum wire, which now accounts for the effect of dielectric mismatch for a wide variety of semiconductor permittivities. The different parameters in the formula have been fitted to several expressions, which enables a quick reconstruction of the complete effective exciton potential for different dielectric permittivities. The new formula greatly facilitates the determination of the energy levels of the exciton (i.e. ground and excited states) and the optical oscillator strengths while drastically reducing the computation time (by as much as a factor of 100). Furthermore, the self energy and the binding energy were studied as a function of the dielectric mismatch. It was shown that a change in dielectric constant of the wire material from one to five has a significantly larger influence on the total energy then a change from e.g. five to ten. Although we only used a simple two band model, we find that our theoretical results compare rather well with the experimental values reported in several papers. Also the binding energy as function of the wire radius was calculated for different values of the dielectric mismatch and fitted to an analytical expression.

In the **fourth chapter** the complexity increases further, when I study the stability of positively and negatively charged excitons in wires with different dielectric constants. Due to our previous work on excitons, reconstructing the 2D effective potential for trions is an easy and very simple task, which enables us to immediately start with calculations of trion binding energies. I found that the negatively charged exciton has always a smaller binding energy than the positively charged exciton in a wire with a hole to electron mass ratio $\sigma > 1$, even when the dielectric mismatch is larger. In the case of $\sigma < 1$ the opposite is true. This is in contrast to the embedded V-grooved wires where it was found experimentally that for narrow widths $|E_B(X^-)| > |E_B(X^+)|$. Furthermore, I found that the dielectric mismatch does not change the qualitative behavior of the $\sigma$-dependence of the binding energy for the $X^-$ trion, whereas the curves for the $X^+$ singlet state show a less pronounced $\sigma$-

dependence with increasing $\epsilon_1/\epsilon_0$. I also studied the trion wave functions and discussed both correlation functions and conditional probabilities of the trions. These results show the correlated arrangement of the particles in the wire. The binding energies as function of the wire radius exhibit, to a good approximation, a $1/R$ dependence.

Finally, in **chapter five**, I investigated the energy levels of an impurity near a metallic interface. I calculated the energy levels of a donor as a function of its position and compared them with the bulk values to demonstrate the effect of the metallic interface on the energy levels that may also carry source-to-drain tunneling currents in nanoscale transistors. In view of potential quantum computing applications, I have studied the effect of an electric field moving the electron away from the donor site to the interface. An acceptable degree of lateral localization of the electron at the interface can be kept at experimentally relevant fields to switch between the donor site and the metallic interface. This conclusion is also supported by the electric field dependence of the energy spectrum: only at very large electric fields, the energy spectrum is dominated by the electric field strength and not by the characteristic of the sample, e.g. the donor position. Ionization is found to occur adiabatically when the donor resides close to the interface, whereas it occurs suddenly for large distances from the interface. In the range of experimentally relevant electric fields, the donor position clearly affects the donor energy levels and the effect of a sudden ionization can be seen.

# 7

# Samenvatting

In deze thesis werd een theoretische studie uitgevoerd over de eigenschappen van excitonen en onzuiverheden in halfgeleider nanodraden en gerelateerde systemen. Waardevolle informatie over specifieke karakteristieken kan men bekomen door de excitoneigenschappen van deze laag-dimensionele systemen te bestuderen. Aangezien er een zeer grote variëteit aan materialen en afmetingen bestaat bij nanodraden, heb ik steeds geprobeerd de meeste berekeningen in deze thesis zo algemeen mogelijk te houden, wat een breed spectrum van toepasbaarheid biedt van het geleverde werk. De focus van dit werk is gericht op het bepalen van de karakteristieken van excitonen en excitoncomplexen. Verder werd eveneens een onzuiverheid aan een metallisch scheidingsoppervlak onderzocht. Dit is relevant zowel voor nanodraden als voor andere toepassingen, zoals bijvoorbeeld de ontwikkeling van kwantumcomputers.

In het **eerste hoofdstuk** werd een inleiding gegeven tot het thesiswerk. Ik heb verschillende groeimethodes voor draden besproken, alsook enkele recentelijk gerealiseerde toepassingen, om een beeld te vormen van het enorme potentieel dat schuilt in nanodraden en gelijkaardige systemen. Devices gebaseerd op nanodraden bezitten immers dikwijls superieure kwaliteiten in vergelijking met andere, reeds bestaande devices, wat ervoor gezorgd heeft dat vele wetenschappers een mooie toekomst weggelegd zien voor nanodraden. Na een bespreking van de toepassingen, richt ik mijn aandacht naar een meer theoretisch gedeelte, waar een inleiding gegeven wordt tot de vaste-stoffysica, tesamen met enkele basisbegrippen zoals excitonen en excitoncomplexen.

De excitoneigenschappen komen in hun meest eenvoudige vorm – t.t.z. zonder diëlektrische mismatch – aan bod in **hoofdstuk twee**. In dit hoofdstuk heb ik de effectieve interactiepotentiaal bepaald, alsook de exciton bindingsen-

ergie. Deze interactiepotentiaal werd berekend voor verschillende toestanden van het elektron en van de holte, waar we telkens in staat waren "numeriek exacte" resultaten te bepalen. Om het computationele werk enigszins te verlichten in de toekomst, werden de numerieke resultaten gebruikt om drie analytische functies aan te fitten. Een eerste Padé benadering gaf reeds een correct kwalitatief gedrag, maar deze fit was echter niet optimaal. Een tweede Padé benadering alsook de functie dewelke oorspronkelijk afkomstig is van het geval waar een parabolische opsluitingspotentiaal genomen wordt, resulteert in een goede fit. Verder werd de exciton bindingsnergie zowel semi-analytisch als numeriek berekend. Analytische fits werden eveneens bepaald. Ik heb ook de invloed van een magneetveld bestudeerd en een analytische uitdrukking bepaald voor de effectieve potentiaal voor willekeurige magneetvelden. Tot slot heb ik de bindingsenergie als functie van het magneetveld berekend.

De diëlektrische mismatch werd mee in rekening genomen vanaf **hoofdstuk drie**. De interactiepotentiaal wordt hierdoor significant ingewikkelder en werd in detail bestudeerd. Opnieuw heb ik gezocht naar een geschikte analytische uitdrukking voor de effective excitonpotentiaal in een halfgeleider nanodraad. In deze uitdrukking kan nu rekening gehouden worden met een grote spreiding aan waarden van de diëlektrische mismatch. De verschillende parameters in de formule voor de potentiaal werden immers gefit voor een hele range van mismatchen, wat ervoor zorgt dat een snelle reconstructie van de effectieve interactiepotentiaal mogelijk is voor verschillende diëlektrische constanten. De nieuwe formule vergemakkelijkt aanzienlijk de bepaling van de energieniveau's (grondtoestand en geëxciteerde toestanden) en de optische oscillatorsterkte, terwijl de computationele rekentijd significant (met een factor 100) gereduceerd wordt. Verder werd eveneens de zelfenergie en de bindingsenergie bepaald als functie van de diëlektrische mismatch. Deze studie bracht aan het licht dat een verandering in de diëlektrische constante van het materiaal van de draad het sterkste effect op de energie zal hebben voor waarden tussen 1 en 5, terwijl dit effect minder uitgesproken zal zijn tussen bijvoorbeeld 5 en 10. Ondanks het feit dat we gebruik gemaakt hebben van een eenvoudig twee-bandenmodel, vinden we dat de resultaten vrij goed overeenstemmen met de experimentele resultaten uit verscheidene artikels. De bindingsenergie werd tenslotte bepaald als functie van de straal van de draad voor verschillende waarden van diëlektrische mismatch en eveneens gefit aan analytische uitdrukkingen.

In **hoofdstuk vier** neemt de complexiteit toe, als ik positief en negatief geladen excitonen in draden met verschillende diëlektrische constanten bestudeer. Dankzij het eerder geleverde werk over de excitonen, is het construeren van de effectieve 2D-trionpotentiaal een gemakkelijk en erg eenvoudige opgave, zodat onmiddellijk gestart kan worden met de bepaling van de trion bindingsenergie. Ik heb gevonden dat het negatief geladen exciton steeds minder sterk gebonden is dan het positief geladen exciton in een draad met een holte-elektron massaverhouding $\sigma > 1$, ook al verandert de mismatch. Voor $\sigma < 1$ is het omgekeerde waar. Dit is in tegenstelling met de bevindingen die

gedaan werden bij ingebedde V-grooved draden, waar men experimenteel heeft aangetoond dat voor kleine breedtes $|E_B(X^-)| > |E_B(X^+)|$. Verder heb ik eveneens gevonden dat de diëlektrische mismatch het kwalitatieve gedrag van de $\sigma$-afhankelijkheid van de bindingsenergie niet veranderde voor het $X^-$-trion, terwijl de $X^+$-singlet toestand een minder uitgesproken gedrag van $\sigma$-afhankelijkheid vertoont bij toenemende $\epsilon_1/\epsilon_0$. Ook de trion golffuncties werden bestudeerd, alsook de correlatiefuncties en de conditionele waarschijnlijkheden van trionen. Deze resultaten tonen de correlatie in de schikking van de deeltjes in de draad. De bindingsenergie als functie van de straal van de draad vertoont, in goede benadering, een $1/R$ gedrag.

Tot slot heb ik in **hoofdstuk vijf** de energieniveau's van een onzuiverheid aan een metallisch scheidingsoppervlak bestudeerd. Ik heb de energieniveau's van een donor berekend als functie van zijn positie ten opzichte van het scheidingsoppervlak en vergeleken met de bulk waarden. Dit toont het effect van het metallische scheidingsoppervlak op de energieniveau's van de donor, dewelke kunnen instaan voor source-naar-drain tunneling in transistoren op nanoschaal. Met het oog op mogelijke toepassingen in het gebied van de kwantumcomputers, heb ik het effect bestudeerd van een elektrisch veld dat in staat is het elektron te verplaatsen van de donor naar de interface. Een acceptabele graad van laterale localisatie van het elektron kan behouden blijven voor het normale bereik van elektrische velden dat in experimenten gebruikt wordt. Deze conclusie volgt eveneens uit de veldafhankelijkheid van het energiespectrum: enkel bij zeer hoge elektrische velden, zal het energiespectrum gedomineerd worden door de sterkte van het elektrisch veld en niet door de karakteristieke eigenschappen van het monster, zoals b.v. de donor positie. De ionisatie van de donor gebeurt op een adiabatische manier als de donor zich dicht bij het scheidingsoppervlak bevindt, terwijl het plots gebeurt op grote afstanden van het scheidingsoppervlak. In het gebied van elektrische velden dat relevant is voor het experiment is het effect van de positie van de donor op het energieniveau duidelijk merkbaar, evenals het effect van een plotse ionisatie.

# *Appendix A Numerical calculation of the effective potential*

To obtain the effective exciton potential of Eq. (2.11), we have to evaluate four-fold integrals. They can be rewritten in polar coordinates as follows, using the same dimensionless units as before (i.e. distances scaled with the wire radius):

$$V_{\text{eff}}(z) = -\int \rho_e \rho_h \mathrm{d}\rho_e \mathrm{d}\rho_h \mathrm{d}\theta_e \mathrm{d}\theta_h \frac{|\psi_{nl}(\rho_e,\theta_e)|^2 \, |\psi_{n'l'}(\rho_h,\theta_h)|^2}{\sqrt{\rho_e^2+\rho_h^2-2\rho_e\rho_h cos(\theta_e-\theta_h)+z^2}} \tag{A.1}$$

Due to cylindrical symmetry, we can perform the integral over the angle $\theta_h$ analytically, yielding

$$\begin{aligned} &\int_0^{2\pi} \mathrm{d}\theta_e \int_0^{2\pi} \frac{\mathrm{d}\theta_h}{\sqrt{\rho_e^2+\rho_h^2-2\rho_e\rho_h cos(\theta_e-\theta_h)+z^2}} \\ &\quad = 2\pi \frac{4}{\sqrt{(\rho_e+\rho_h)^2+z^2}} \mathbb{K}\left(\frac{4\rho_e\rho_h}{(\rho_e+\rho_h)^2+z^2}\right) \end{aligned} \tag{A.2}$$

where $\mathbb{K}(m)$ is the elliptic integral of the first kind. Since

$$\mathbb{K}(-m) = (1+m)^{-1/2}\mathbb{K}(m(1+m)^{-1}); \tag{A.3}$$

we can rewrite Eq. (A.2) to

$$I_1 = \frac{4}{\sqrt{(\rho_e+\rho_h)^2+z^2}}\mathbb{K}\left(\frac{4\rho_e\rho_h}{(\rho_e+\rho_h)^2+z^2}\right) \tag{A.4}$$

Using a polynomial approximation [86] for the elliptic integral,

$$\begin{aligned}\mathbb{K}(m) &= \sum_{i=0}^{4} a_i m_1^i + \sum_{i=0}^{4} b_i m_1^i \ln\frac{1}{m_1} \\ &\equiv \mathbb{A}(m_1) + \mathbb{B}(m_1)\ln(1/m_1),\end{aligned} \tag{A.5}$$

where $a_0 = 1.3863, a_1 = 0.0967, a_2 = 0.0359, a_3 = 0.0374, a_4 = 0.0145, b_0 = 0.5, b_1 = 0.1250, b_2 = 0.0688, b_3 = 0.0333, b_4 = 0.0044$ and $m_1 = 1 - m$, we find that

$$\begin{aligned}V_{\text{eff}}(z) &= -2\pi\int_0^1 \mathrm{d}\rho_e\rho_e\left|\psi_{nl}(\rho_e,\theta_e)\right|^2 \\ &\times \underbrace{\int_0^1 4\frac{\mathrm{d}\rho_h\rho_h\left|\psi_{n'l'}(\rho_h,\theta_h)\right|^2}{\sqrt{(\rho_e+\rho_h)^2+z^2}}\left[\mathbb{A}(m_1)+\mathbb{B}(m_1)\ln\frac{1}{m_1}\right]}_{\equiv I_1}.\end{aligned}$$

In a next step, we calculate the integral $I_1$ over $\rho_h$ using numerical techniques. To obtain good convergence, we use the logarithmically weighted method and consider the following integral:

$$I(\rho_e,z) = \int_0^1 \mathrm{d}\rho_h F(\rho_h,\rho_e,z)\ln\left(\frac{(\rho_e-\rho_h)^2+z^2}{(\rho_e+\rho_h)^2+z^2}\right). \tag{A.6}$$

We use the following transformation

$$\begin{aligned}I(\rho_e,z) &= \sum_{i=0}^{s-1}\int_0^h \mathrm{d}x F(x+hi,\rho_e,z) \\ &\quad\times\ln\left(\frac{(x-(\rho_e-hi))^2+z^2}{(x+(\rho_e+hi))^2+z^2}\right),\end{aligned} \tag{A.7}$$

where $h$ denotes the step size and $s$ the total number of steps. If we replace $F(x+hi)$ by $F_i + (F_{i+1}+F_i)x/h$, we can write (A.7) as

$$I(\rho_e,z) = \sum_{i=0}^{s-1} F_i A_i(\rho_e,z) + (F_{i+1}-F_i)\,C_i(\rho_e,z), \tag{A.8}$$

and the remaining problem is the calculation of the coefficients $A_i$ and $C_i$. These coefficients are given by

$$\begin{aligned} A_i(\rho_e, z) &= \int_0^h \mathrm{d}x \ln\left(\frac{(x-(\rho_e - hi))^2 + z^2}{(x+(\rho_e + hi))^2 + z^2}\right), \\ C_i(\rho_e, z) &= \frac{1}{h}\int_0^h \mathrm{d}x x \ln\left(\frac{(x-(\rho_e - hi))^2 + z^2}{(x+(\rho_e + hi))^2 + z^2}\right). \end{aligned} \tag{A.9}$$

These integrals can be performed analytically which leads to the following results:

$$A_i(\rho_e, z) = a(h-(\rho_e - hi)) - a(h+(\rho_e + h_i)), \tag{A.10}$$

$$C_i(\rho_e, z) = h^{-1}\left[c(h-(\rho_e - hi)) - c(h+(\rho_e + h_i))\right] - 2\rho_e, \tag{A.11}$$

with

$$\begin{aligned} a(y) &= H_i(y) + H_i(h-y) + 2z\left[\arctan\left(\frac{y}{z}\right) + \arctan\left(\frac{h-y}{z}\right)\right], \\ H_i(y) &= y\ln(y^2+z^2), \\ c(y) &= \frac{1}{2}\left(y(2h-y)+z^2\right)G_i(y) + \frac{1}{2}\left((h-y)^2 - z^2\right)G_i(h-y) + 2z(h-y) \\ &\quad \times\left[\arctan\left(\frac{y}{z}\right) + \arctan\left(\frac{h-y}{z}\right)\right], \\ G_i(y) &= \ln(y^2+z^2). \end{aligned} \tag{A.12}$$

Now we can write, using the logarithmically weighted method,

$$\begin{aligned} I_1 &= \int \frac{4\mathrm{d}\rho_h \rho_h \left|\psi_{n'l'}(\rho_h, \theta_h)\right|^2}{\sqrt{(\rho_e+\rho_h)^2 + z^2}} \left(\mathbb{A}(m_1) + \mathbb{B}(m_1)\ln(m_1)\right) \\ &= \sum_{i=0}^{s-1}\int_0^h \mathrm{d}x F(x+hi)\left(\mathbb{A}(m_1) + \mathbb{B}(m_1)\ln(m_1)\right) \\ &= \sum_{i=1}^{s-1}\left(F_i h\mathbb{A}(m_1) + F_i\left(A_i + C_{i-1} - C_i\right)\mathbb{B}(m_1)\right) \\ &\quad + F_s\frac{h}{2}\mathbb{A}(m_1) + F_s C_{s-1}\mathbb{B}(m_1), \end{aligned} \tag{A.13}$$

where

$$F_i \equiv F(hi) = \frac{4hi\left|\psi_{n',l'}(hi)\right|^2}{\sqrt{(\rho_e+hi)^2+z^2}}. \tag{A.14}$$

The final step is to calculate then the integral over $\rho_e$. Similarly, we can also perform this last integration over $\rho_e$. Using the above mentioned result of

Eq. (A.13), we obtain the final expression for the effective potential in the $z$-direction:

$$\begin{aligned} V_{\text{eff}}(z) &= -2\pi\Bigg[h\sum_{j=1}^{s-1} hj\,|\psi_{nl}(hj)|^2\Big[\big[S_1(hj)h + T(hj)\frac{h}{2}\mathbb{A}(m_1)\big] \\ &\quad -\big[S_2(hj) + T(hj)C_{s-1}\mathbb{B}(m_1)\big]\Big] + \frac{h}{2}hs\,|\psi_{nl}(sh,\theta_e)|^2 \\ &\quad \times\Big[\big[S_1(hs)h + T(hs)\frac{h}{2}\mathbb{A}(m_1)\big] - \big[S_2(hs) + T(hs)C_{s-1}\mathbb{B}(m_1)\big]\Big]\Bigg] \end{aligned}$$

with

$$S_1(x) = \sum_{i=1}^{s-1} \frac{4hi\,|\psi_{n'l'}(hi,\theta_h)|^2}{\sqrt{(x+hi)^2+z^2}}\mathbb{A}(m_1), \tag{A.15}$$

$$T(x) = \frac{4sh\,|\psi_{n'l'}(sh,\theta_h)|^2}{\sqrt{(x+sh)^2+z^2}}, \tag{A.16}$$

$$S_2(x) = \sum_{i=1}^{s-1} \frac{4hi\,|\psi_{n'l'}(hi,\theta_h)|^2}{\sqrt{(x+hi)^2+z^2}}(A_i + C_{i-1} - C_i)\mathbb{B}(m_1). \tag{A.17}$$

# *Appendix B Discretisation of the 1D Schrödinger equation on an inhomogeneous grid*

In order to solve the 1D Schrödinger equation,

$$-\alpha\frac{d^2\phi(z)}{dz^2} + \tilde{V}_{\text{eff}}(z)\phi(z) = \tilde{E}_C\phi(z), \tag{B.1}$$

on a grid, it is favorable to use the finite volume method (FVM). In Fig. B.1, a schematical picture is given, that shows the typical potential profile together with the wave function at its lowest binding energy. It is clear that an inhomogeneous grid is highly desirable: a high amount of grid points around the origin (region of potential minimum and strongest variation in the wave function) is necessary to obtain good numerical results without increasing the number of grid points too much in regions that are of less importance, such as the tails of the wave function (region of slowly varying potential). The FVM can be implemented by introducing the finite volumes,

$$B_k = [z_{k-1/2}, z_{k+1/2}], \tag{B.2}$$

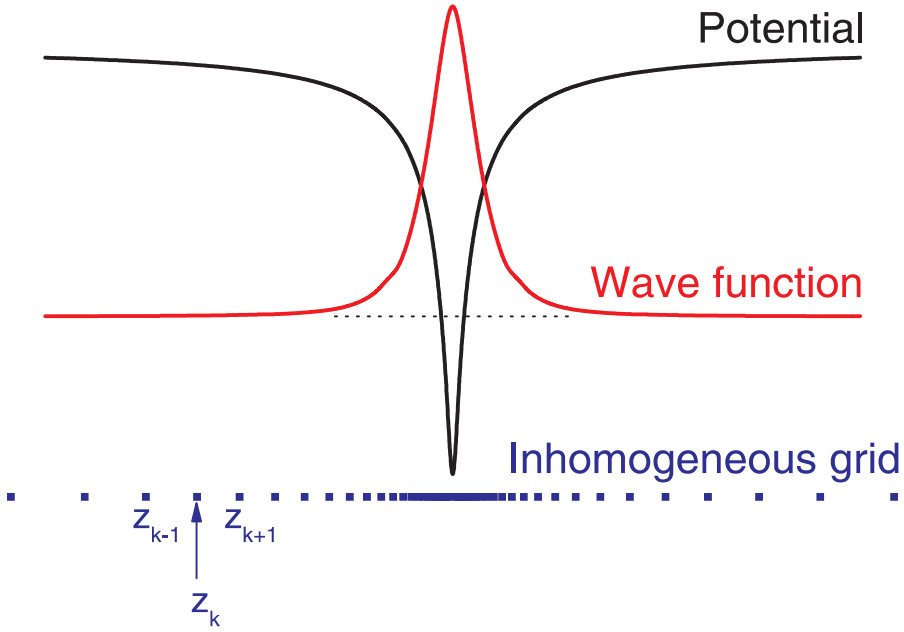


*Fig. B.1* Schematical picture of a typical potential profile (black) and the corresponding wave function (red) at the ground state energy. At the bottom, the inhomogeneous grid (blue) is shown.

where $z_{k\pm1/2} = (z_{k\pm1} + z_k)/2$. Integrating Eq. (B.1) over these finite volumes, we obtain

$$\int_{B_k} -\alpha \frac{d^2\phi(z)}{dz^2} = \int_{B_k} \left(\tilde{E}_C - \tilde{V}_{\text{eff}}(z)\right) \phi(z). \tag{B.3}$$

Integrating the left hand side by parts yields

$$-\alpha \int_{\partial B_k} \frac{d\phi(z)}{dz} = \int_{B_k} \left(\tilde{E}_C - \tilde{V}_{\text{eff}}(z)\right) \phi(z), \tag{B.4}$$

or

$$\left[-\alpha \frac{d\phi(z)}{dz}\right]_{z_{k-1/2}}^{z_{k+1/2}} = \int_{B_k} \left(\tilde{E}_C - \tilde{V}_{\text{eff}}(z)\right) \phi(z). \tag{B.5}$$

This means

$$-\alpha \left(\frac{d\phi(z)}{dz}(z_{k+1/2}) - \frac{d\phi(z)}{dz}(z_{k-1/2})\right) = \int_{B_k} \left(\tilde{E}_C - \tilde{V}_{\text{eff}}(z)\right) \phi(z). \tag{B.6}$$

Note that this is still an exact expression, which respects the physical conservation law. Now we are going to approximate this expression by writing the first derivatives as divided differences. The right hand side is approximated

by a quadrature formula (the midpoint rule). We obtain thus

$$-\alpha\left(\frac{\phi_{k+1}-\phi_k}{z_{k+1}-z_k}-\frac{\phi_k-\phi_{k-1}}{z_k-z_{k-1}}\right)=\left(z_{k+1/2}-z_{k-1/2}\right)\left(\tilde{E}_C-\tilde{V}_{\text{eff}}(z_k)\right)\phi_k. \tag{B.7}$$

This finite difference scheme results in a Hermitian matrix and allows the use of a non-homogeneous grid. This is of great advantage to obtain accurate results without increasing the computing time too much.

# *References*


1. http://www.itrs.net/Links/2007ITRS/ExecSum2007.pdf

2. Y. Huang, X. Duan, Y. Cui, and C.M. Lieber, Nano Lett. **2**, 101 (2002).

3. L.J. Lauhon, M.S. Gudiksen, D. Wang, and C.M. Lieber, Nature (London) **420**, 57 (2002).

4. Y. Li, J. Xiang, F. Qian, S. Gradečak, Y. Wu, H. Yan, D.A. Blom, and C.M. Lieber, Nano Lett. **6**, 1468 (2006).

5. J. Goldberger, A.I. Hochbaum, R. Fan, and P. Yang, Nano Lett. **6**, 973 (2006).

6. Y. Cui and C.M. Lieber, Science **291**, 851 (2001).

7. X. Duan, Y. Huang, Y. Cui, J. Wang, and C.M. Lieber, Nature (London) **409**, 66 (2001).

8. X. Duan, Y. Huang, and C.M. Lieber, Nano Lett. **2**, 487 (2002).

9. M.H. Huang, S. Mao, H. Feick, H. Yan, Y. Wu, H. Kind, E. Weber, R. Russo, and P. Yang, Science **292**, 1897 (2001).

10. X. Duan, Y. Huang, R. Agarwal, and C.M. Lieber, Nature (London) **421**, 241 (2003).

11. H. Cao, X. Qiu, Y. Liang, Q. Zhu, and M. Zhao, Appl. Phys. Lett. **83**, 761 (2003).

12. Y. Cui, Q. Wei, H. Park, and C.M. Lieber, Science **293**, 1289 (2001).

13. Q.H. Li, Q. Wan, Y.X. Liang, and T.H. Wang, Appl. Phys. Lett. **84**, 4556 (2004).

14. Z. Zhong, D. Wang, Y. Cui, M.W. Bockrath, and C.M. Lieber, Science **302**, 1377 (2003).

15. Y. Huang, X. Duan, Q. Wei, and C.M. Lieber, Science **291**, 630 (2001).

16. F.J. Rueß, W. Pok, T.C.G. Reusch, M.J. Butcher, K.E.J. Goh, L. Oberbeck, G. Scappucci, A.R. Hamilton, and M.Y. Simmons, Small **3**, 563 (2007).

17. L.E. Calvet, R.G. Wheeler, and M.A. Reed, Appl. Phys. Lett. **80**, 1761 (2002).

18. L.E. Calvet, R.G. Wheeler, and M.A. Reed, Phys. Rev. Lett. **98**, 096805 (2007).

19. H. Sellier, G. P. Lansbergen, J. Caro, S. Rogge, N. Collaert, I. Ferain, M. Jurczak, and S. Biesemans, Phys. Rev. Lett. **97**, 206805 (2006).

20. B.E. Kane, Nature (London) **393**, 133 (1998).

21. B.E. Kane, Fortschr. Phys. **48**, 1023 (2000).

22. C.Y. Chang and S.M. Sze, *ULSI technology* (McGraw-Hill, New York, 1996).

23. M. Zgirski, K.-P. Riikonen, V. Tuboltsev, P. Jalkanen, T.T. Hongisto, and K.Y. Arutyunov, Nanotechnology **19**, 055301 (2008).

24. N. Wang, Y. Cai, and R.Q. Zhang, Mat. Science and Engineering R **60**, 1 (2008).

25. M. Kuno, Phys. Chem. Chem. Phys. **10**, 620 (2008).

26. Y. Xia, P. Yang, Y. Sun, Y. Wu, B. Mayers, B. Gates, Y. Yin, F. Kim, and H. Yan, Adv. Mater. **15**, 353 (2003).

27. R.S. Wagner and W.C. Ellis, Appl. Phys. Lett. **4**, 89 (1964).

28. A.M. Morales and C.M. Lieber, Science **279**, 208 (1998).

29. Y. Wu and P. Yang, Chem. Mater. **12**, 605 (2000).

30. Y.J. Zhang, Q. Zhang, N.L. Wang, Y.J. Yan, H.H. Zhou, and J. Zhu, J. Cryst. Growth **226**, 185 (2001).

31. J. Westwater, D.P. Gosain, S. Tomiya, and S. Usui, J. Vac. Sci. Technol. B **15**, 554 (1997).

32. C.C. Chen, C.C. Yeh, C.H. Chen, M.Y. Yu, H.L. Liu, J.J. Wu, K.H. Chen, L.C. Chen, J.Y. Peng, and Y.F. Chen, J. Am. Chem. Soc. **123**, 2791 (2001).

33. J. Zhang, X.S. Peng, X.F. Wang, Y.W. Wang, and L.D. Zhang, Chem. Phys. Lett. **345**, 372 (2001).

34. M.Q. He, P.Z. Zhou, S.N. Mohammad, G.L. Harris, J.B. Halpern, R. Jacobs, W.L. Sarney, and L. Salamanca-Riba, J. Cryst. Growth **231**, 357 (2001).

35. W.S. Shi, Y.F. Zheng, N. Wang, C.S. Lee, and S.T. Lee, J. Vac. Sci. Tech. B **19**, 1115 (2001).

36. C.C. Chen and C.C. Yeh, Adv. Mater. **12**, 738 (2000).

37. T. Shimada, K. Hiruma, M. Shirai, M. Yazawa, K. Haraguchi, T. Sato, M. Matsui, and T. Katsuyama, Superlattices Microstruct. **24**, 453 (1998).

38. K. Hiruma, M. Yazawa, T. Katsuyama, K. Ogawa, K. Haraguchi, M. Koguchi, and H. Kakibayashi, J. Appl. Phys. **77**, 447 (1995).

39. M. Yazawa, M. Kohuchi, A. Muto, and K. Hiruma, Adv. Mater. **5**, 577 (1993).

40. Y.W. Wang, L.D. Zhang, C.H. Liang, G.Z. Wang, and X.S. Peng, Chem. Phys. Lett. **357**, 314 (2002).

41. Y.W. Wang, G.W. Meng, L.D. Zhang, C.H. Liang, and J. Zhang, Chem. Mater. **14**, 1773 (2002).

42. X. Duan and C.M. Lieber, Adv. Mater. **12**, 298 (2000).

43. M. Lopez-Lopez, A. Guillen-Cervantes, Z. Rivera-Alvarez, and I. Hernandez-Calderon, J. Cryst. Growth **193**, 528 (1998).

44. Y.J. Chen, J.B. Li, Y.S. Han, X.Z. Yang, and J.H. Dai, J. Cryst. Growth **245**, 163 (2002).

45. X.C. Wu, W.H. Song, K.Y. Wang, T. Hu, B. Zhao, Y.P. Sun, and J.J. Du, Chem. Phys. Lett. **336**, 53 (2001).

46. M.H. Huang, Y. Wu, H. Feick, N. Tran, E. Weber, and P. Yang, Adv. Mater. **13**, 113 (2001).

47. X.M. Cai, A.B. Djurišić, and M.H. Xie, Thin Solid Films **515**, 984 (2006).

48. Y.F. Chan, X.F. Duan, S.K. Chan, I.K. Sou, X.X. Zhang, and N. Wang, Appl. Phys. Lett. **83**, 2665 (2003).

49. http://physik2.uni-goettingen.de/faculty/4_ronning/Nanowires

50. Y. Wu and P. Yang, J. Am. Chem. Soc. **123**, 3165 (2001).

51. L. Samuelson, M.T. Björk, K. Deppert, M. Larsson, B.J. Ohlsson, N. Panev, A.I. Persson, N. Sköld, C. Thelander, and L.R. Wallenberg, Phys. E **21**, 560 (2004).

52. L.J. Lauhon, M.S. Gudiksen, and C.M. Lieber, Phil. Trans. R. Soc. Lond A **362**, 1247 (2004).

53. E.A. Stach, P.J. Pauzauskie, T. Kuykendall, J. Goldberger, R. He, and P. Yang, Nano Lett. **3**, 867 (2003).

54. Y. Cai, S.K. Chan, I.K. Sou, Y.F. Chan, D.S. Su, and N. Wang, Small **3**, 111 (2007).

55. C.R. Martin, Science **266**, 1961 (1994).

56. J.D. Holmes, K.P. Johnston, R.C. Doty, and B.A. Korgel, Science **287**, 1471 (2000).

57. F. Wang, A. Dong, J. Sun, R. Tang, H. Yu, and W.E. Buhro, Inorg. Chemistry **45**, 7511 (2006).

58. D. Fuster, B. Alén, L. González, Y. González, J. Martínez-Pastor, M.U. González, and J.M. García, Nanotechnology **18**, 035604 (2007).

59. J.-W. Lee, M.-H. Ham, and J.-M. Myoung, Sol. Stat. Comm. **145**, 327 (2008).

60. F. Patolsky, B.P. Timko, G. Zheng, and C.M. Lieber, MRS Bull. **32**, 142 (2007).

61. C. Kittel, *Introduction to solid state physics*, 6th ed. (John Wiley & Sons, Inc., New York, 1986).

62. N.V. Ashcroft and N.D. Mermin, *Solid State Physics* (Holt, Rinehart and Winston, New York, 1976).

63. J. Singh, *Electronic and optoelectronic properties of semiconductor structures* (Cambridge University Press, Cambridge, 2003)

64. J.R. Chelikowsky and M.L. Cohen, Phys. Rev. B **14**, 556 (1976).

65. http://www.ioffe.rssi.ru/SVA/NSM/Semicond/InP/bandstr.html

66. J.M. Luttinger and W. Kohn, Phys. Rev. **97**, 869 (1955); J.M. Luttinger, Phys. Rev. **102**, 1030 (1956).

67. E.O. Kane, J. Chem Phys. Solids **1**, 249 (1957).

68. M. Cardona and F.H. Pollak, Phys. Rev. **142**, 530 (1966).

69. G.E. Pikus and G.L. Bir, Sov. Phys.-Solid State **1**, 1502 (1959).

70. http://www-opto.e-technik.uni-ulm.de/lehre/cs/index.html

71. M.D. Sturge, Phys. Rev. **127**, 768 (1962).

72. M.A. Lampert, Phys. Rev. Lett. **1**, 450 (1958).

73. G. Munschy and B. Stébé, Phys. Stat. Sol. (b) **64**, 213 (1974).

74. K. Kheng, R. T. Cox, Merle Y. d'Aubigné, Franck Bassani, K. Saminadayar, and S. Tatarenko, Phys. Rev. Lett. **71**, 1752 (1993).

75. J. Bellessa, V. Voliotis, R. Grousson, X. L. Wang, M. Ogura, and H. Matsuhata, Appl. Phys. Lett. **71**, 2481 (1997).

76. A. Hartmann, Y. Ducommun, E. Kapon, U. Hohenester, and E. Molinari, Phys. Rev. Lett. **84**, 5648 (2000).

77. http://www.comsol.com

78. L. Ramdas Ram-Mohan, *Finite Element and boundary element applications in quantum mechanics* (Oxford University Press, Oxford, 2003).

79. T. Ogawa and T. Takagahara, Phys. Rev. B **44**, 8138 (1991).

80. D.S. Chuu, C.M. Hsiao, and W.N. Mei, Phys. Rev. B **46**, 3898 (1992).

81. S.V. Branis, G. Li, and K.K. Bajaj, Phys. Rev. B **47**, 1316 (1993).

82. L. Banyai, I. Galbraith, C. Ell, and H. Haug, Phys. Rev. B **36**, 6099 (1987). Note that this paper contains several mistakes in the formulas; the figures, however, are correct which indicates that the mistakes are typing errors. Nevertheless, one should be careful and not just copy the formulas.

83. Y. Sidor, B. Partoens, and F.M. Peeters, Phys. Rev. B **71**, 165323 (2005).

84. S. Bednarek, B. Szafran, T. Chwiej, and J. Adamowski, Phys. Rev. B **68**, 045328 (2003).

85. For the sake of simplicity, we took circular symmetry. One can perform similar calculations for square wires and find that the final results, i.e. the effective exciton potential and exciton energy, match the result of a circular wire with radius comparable to half of the side of a square. This was investigated by Y. Zhang and A. Mascarenhas, Phys. Rev. B **59**, 2040 (1999).

86. M. Abramowitz and I. Stegun, *Handbook of mathematical functions* (Dover, New York, 1970).

87. P.J. Price, Sol. State Electron. **39**, 653 (1996).

88. R. Loudon, Am. J. Phys. **27**, 649 (1959).

89. F. Geerinckx, F.M. Peeters, and J.T. Devreese, J. Appl. Phys. **68**, 3435 (1990).

90. A. Shabaev and A.L. Efros, Nano Lett. **4**, 1821 (2004).

91. E.A. Muljarov, E.A. Zhukov, V.S. Dneprovskii, and Y. Masumoto, Phys. Rev. B **62**, 7420 (2000).

92. J.B. Xia, and K.W. Cheah, Phys. Rev. B **55**, 1596 (1997).

93. A. Shik, J. Appl. Phys. **74**, 2951 (1993).

94. V.A. Fonoberov, E.P. Pokatilov, and A.A. Balandin, Phys. Rev. B **66**, 085310 (2002).

95. S. Bhunia, T. Kawamura, Y. Watanabe, S. Fujikawa, and K. Tokushima, Appl. Phys. Lett. **83** 3371 (2003).

96. G.A. Thomas and T.M. Rice, Sol. Stat. Comm. **23**, 359 (1977).

97. T. Kawabata, K. Muro, and S. Narita, Sol. Stat. Comm. **23**, 267 (1977).

98. B. Stébé and A. Ainane, Superl. Microstr. **5**, 545 (1989).

99. B. Szafran, B. Stébé, J. Adamowski, and S. Bednarek, Phys. Rev. B **66**, 165331 (2002).

100. M. Law, J. Goldberger, and P. Yang, Annu. Rev. Mater. Res. **34**, 83 (2004).

101. B. Szafran, T. Chwiej, F.M. Peeters, S. Bednarek, and J. Adamowski, Phys. Rev. B **71**, 235305 (2005).

102. S. Baskoutas, Chem. Phys. Lett. **404**, 107 (2005).

103. C. Riva, F.M. Peeters, and K. Varga, Phys. Rev. B **61**, 13873 (2000).

104. A.S. Bracker, E.A. Stinaff, D. Gammon, M.E. Ware, J.G. Tischler, D. Park, D. Gershoni, A.V. Filinov, M. Bonitz, F.M. Peeters, and C. Riva, Phys. Rev. B **72**, 035332 (2005).

105. I. Vurgaftman, J.R. Meyer, and L.R. Ram-Mohan, Journal of Appl. Phys. **89**, 5815 (2001).

106. G. Coli and K.K. Bajaj, Appl. Phys. Lett. **78**, 2861 (2001).

107. http://www.semiconductors.co.uk/

108. A.J. Shields, M. Pepper, M.Y. Simmons, and D.A. Ritchie, Phys. Rev. B **52**, 7841 (1995).

109. T. Otterburg, D.Y. Oberli, M.-A. Dupertuis, N. Moret, E. Pelucchi, B. Dwir, K. Leifer, and E. Kapon, Phys. Rev. B **71**, 033301 (2005).

110. M.J. Calderón, B. Koiller, X. Hu, and S. Das Sarma, Phys. Rev. Lett. **96**, 096802 (2006).

111. D.B. Macmillan and U. Landman, Phys. Rev. B **29**, 4524 (1984).

112. H. Sun and S.-W. Gu, Phys. Rev. B **46**, 224 (1992).

113. M.J. Calderón, B. Koiller, and S. Das Sarma, Phys. Rev. B **75**, 125311 (2007).

114. D.J. Griffiths, *Introduction to electrodynamics* (Prentice Hall of India,1989).

115. A. Debernardi, A. Baldereschi, and M. Fanciulli, Phys. Rev. B **74**, 035202 (2006).

116. G.D.J. Smit, S. Rogge, J. Caro, and T.M. Klapwijk, Phys. Rev. B **68**, 193302 (2003).

117. A.S. Martins, R.B. Capaz, and B. Koiller, Phys. Rev. B **69**, 085320 (2004).

# *List of publications*

- A.F. Slachmuylders, B. Partoens, and F.M. Peeters, *Geometry and magnetic field induced vortices and antivortices in mesoscopic two-dimensional systems*, Phys. Rev. B **71**, 245405 (2005). **Also** selected to appear in the Virtual Journal of Nanoscale Science and Technology, June 20 edition (2005). **Also** selected to appear in the Virtual Journal of Applications of Superconductivity, June 15 edition (2005).

- A.F. Slachmuylders, B. Partoens, W. Magnus, and F.M. Peeters, *Exciton states in cylindrical nanowires*, J. Phys.: Condens. Matter **18**, 3951 (2006).

- A.F. Slachmuylders, B. Partoens, W. Magnus, and F.M. Peeters, *Dielectric mismatch effects on the exciton states in cylindrical nanowires*, Phys. Rev. B **74**, 235321 (2006). **Also** selected to appear in the Virtual Journal of Nanoscale Science and Technology, July 3 edition (2007).

- A.F. Slachmuylders, B. Partoens, W. Magnus, and F.M. Peeters, *Trions in cylindrical nanowires with dielectric mismatch effects*, Phys. Rev. B **76**, 075405 (2007). **Also** selected to appear in the Virtual Journal of Nanoscale Science and Technology, August 20 edition (2007).

- A.F. Slachmuylders, B. Partoens, W. Magnus, and F.M. Peeters, *The effect of the dielectric mismatch on excitons and trions in freestanding nanowires*, Physica E **40**, 2166 (2008).

- A.F. Slachmuylders, B. Partoens, W. Magnus, and F.M. Peeters, *Excitons and trions in cylindrical nanowires with dielectric mismatch*, Phys. Stat. Sol. (c) **5**, 2416 (2008).

- A.F. Slachmuylders, B. Partoens, W. Magnus, and F.M. Peeters, *The effect of dielectric mismatch on excitons and trions in cylindrical semiconductor nanowires*, to appear in Journal of Computational Electronics.

- A.F. Slachmuylders, B. Partoens, W. Magnus, and F.M. Peeters, *Effect of a metallic gate on the energy levels of a shallow donor*, Appl. Phys. Lett. **92**, 083104 (2008).

- B. Li, A.F. Slachmuylders, B. Partoens, W. Magnus, and F.M. Peeters, *Dielectric mismatch effect on shallow impurity states in a semiconductor nanowire*, Phys. Rev. B **77**, 115335 (2008).

# *Curriculum Vitae*


***An Slachmuylders***
***Groenenborgerlaan 171***
***2020 Antwerpen***

an.slachmuylders@ua.ac.be


Duffel, 22/09/1981
Belgian Citizen
Married

## EDUCATION

| **Year** | **Graduate Institution** | **Title of qualification awarded** |
|---|---|---|
| 2004 - 2008 | University of Antwerp, Condensed Matter Theory Group, Department of Physics, Antwerpen | PhD in Physics |
| 1999 - 2004 | University of Antwerp, Condensed Matter Theory Group, Department of Physics, Antwerpen | Master in Physics |
| 2002 - 2004 | University of Antwerp, Antwerpen | Academische Initiële Lerarenopleiding |

## TEACHING EXPERIENCE

Exercises *Numerical methods* (3rd Bachelor Physics).
(Courses in 2005-2006, 2006-2007 and 2007-2008)

## COMPUTER SKILLS

- OS: Windows, Linux (basic);
- Microsoft Office: Powerpoint, Word, Excel;
- Programming software: Matlab, Comsol, C++ and OOP, Fortran (basic);
- Other: Maple, Origin, LaTeX

## LANGUAGES

Dutch (native), English (fluent), French (fluent), Italian (good), German (basic).

## INTERESTS

Languages, cooking, cinema, reading, games.